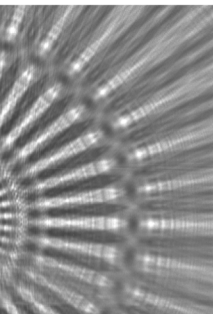


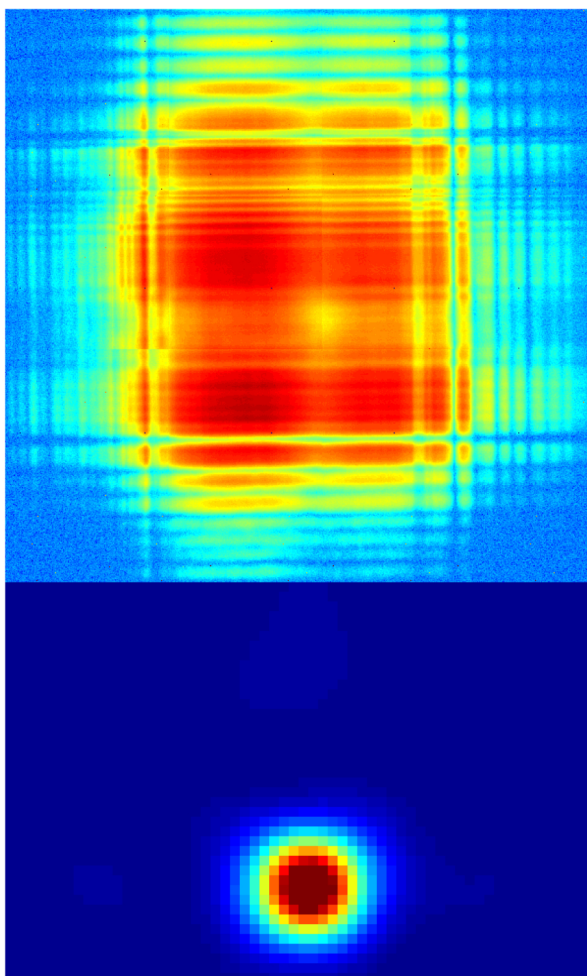


Göttingen Series in
X-ray Physics



Sven Philip Krüger

Optimization of waveguide optics for lensless x-ray imaging



Universitätsverlag Göttingen

Sven Philip Krüger

Optimization of waveguide optics for lensless x-ray imaging

This work is licensed under the [Creative Commons](#) License 3.0 “by-nd”, allowing you to download, distribute and print the document in a few copies for private or educational use, given that the document stays unchanged and the creator is mentioned. You are not allowed to sell copies of the free version.



Published in 2011 by Universitätsverlag Göttingen
as Volume 2 in the series „Göttingen series in x-ray physics“

Sven Philip Krüger

Optimization of
waveguide optics for lensless
x-ray imaging

Göttingen series in x-ray physics
Volume 2



Universitätsverlag Göttingen
2011

Bibliographische Information der Deutschen Nationalbibliothek

Die Deutsche Nationalbibliothek verzeichnet diese Publikation in der Deutschen Nationalbibliographie; detaillierte bibliographische Daten sind im Internet über <http://dnb.ddb.de> abrufbar.

Supported by the Deutsche Forschungsgemeinschaft, SFB755
and the Bundesministerium für Bildung und Forschung (BMBF), 05KS7MGA

Address of the Author

Dr. Sven Philip Krüger

Email: Sven-Philip.Krueger@phys.uni-goettingen.de

Dissertation zur Erlangung des
mathematisch-naturwissenschaftlichen Doktorgrades
„Doctor rerum naturalium“
der Georg-August-Universität Göttingen
vorgelegt von Sven Philip Krüger aus Saarbrücken
Göttingen 2010

Referent: Prof. Dr. Tim Salditt

Koreferent: Prof. Dr. Hans-Ulrich Krebs

Tag der mündlichen Prüfung: 17.12.2010

This work is protected by German Intellectual Property Right Law.
It is also available as an Open Access version through the publisher's homepage and the Online Catalogue of the State and University Library of Goettingen (<http://www.sub.uni-goettingen.de>). Users of the free online version are invited to read, download and distribute it. Users may also print a small number for educational or private use. However they may not sell print versions of the online book.

Layout: Sven Philip Krüger

Cover: Jutta Pabst

Cover image: Sven Philip Krüger

© 2011 Universitätsverlag Göttingen

<http://univerlag.uni-goettingen.de>

ISBN: 978-3-86395-015-6

ISSN: 2191-9860

Preface of the series editor

The Göttingen series in x-ray physics is intended as a collection of research monographs in x-ray science, carried out at the Institute for X-ray Physics at the Georg-August-Universität in Göttingen, and in the framework of its related research networks and collaborations.

It covers topics ranging from x-ray microscopy, nano-focusing, wave propagation, image reconstruction, tomography, short x-ray pulses to applications of nanoscale x-ray imaging and biomolecular structure analysis.

In most but not all cases, the contributions are based on Ph.D. dissertations. The individual monographs should be enhanced by putting them in the context of related work, often based on a common long term research strategy, and funded by the same research networks. We hope that the series will also help to enhance the visibility of the research carried out here and help others in the field to advance similar projects.

Prof. Dr. Tim Salditt, Editor
Göttingen February 2011

Contents

Introduction	1
1 X-ray propagation imaging	5
1.1 Propagation of x-rays in free-space	5
1.1.1 Wave equations in free-space	5
1.1.2 Free-space propagator	6
1.1.3 Fresnel diffraction	8
1.1.4 Fraunhofer diffraction	9
1.2 Interaction of x-rays with matter	10
1.2.1 Refraction and absorption of x-rays	10
1.2.2 The projection approximation	11
1.3 Imaging regimes	13
1.4 Fresnel scaling theorem	16
1.5 Object reconstruction	18
1.5.1 In-line holographic reconstruction	20
1.5.2 Iterative phase retrieval methods	22
1.5.3 Phase retrieval simulations	24
1.6 Conclusion	31
2 Waveguide optics	33
2.1 State of the art in x-ray optics	33
2.2 Planar waveguides	35
2.2.1 Analytical solution	36
2.2.2 Numerical method	38
2.3 Transmission and coherence	41
2.3.1 Mono-modal waveguides	43
2.3.2 Optimized cladding design	44
2.4 Exit wave-field propagation	48
2.4.1 Waveguide near-field	49
2.4.2 Waveguide far-field	53
2.4.3 Mode beating effect	54
2.5 Conclusion	55
3 Fabrication of x-ray waveguides	57
3.1 Fabrication steps	57
3.2 Deposition of optical layers	58
3.3 Wafer cleaning	59
3.4 Bonding process of the Ge cap wafer	60
3.5 Electroless Nickel plating	61

3.6	Cutting process	65
3.7	Waveguide polishing	66
3.8	Crossing of multilayer slices	68
3.9	Conclusion	69
4	Experiments I: X-ray waveguide characterization	71
4.1	Direct coupling into planar waveguides	71
4.1.1	Experimental setup BM20 beamline, ESRF	71
4.1.2	Waveguide alignment	72
4.1.3	Angular acceptance	73
4.1.4	Transmission	75
4.1.5	Far-field properties	77
4.1.6	Beam blocking materials	80
4.1.7	Conclusions	81
4.2	Direct coupling of a pre-focused beam into planar waveguides	82
4.2.1	ID22 experiment: setup and results	82
4.2.2	ID22-NI experiment: setup and results	86
4.2.3	ID1 experiment: setup and results	88
4.2.4	Conclusions	90
4.3	Two crossed waveguides	91
4.3.1	Experimental setup ID22-NI beamline, ESRF	91
4.3.2	Waveguide alignment	91
4.3.3	Transmission	92
4.3.4	Far-field pattern	93
4.3.5	Near-field reconstruction	94
4.3.6	Conclusions	97
4.4	Waveguide setup for new holography endstation	97
4.4.1	P10 beamline: experiments and results	97
4.5	Conclusions	99
5	Experiments II: Phase contrast imaging	101
5.1	Imaging of test pattern	101
5.1.1	Layout of the test pattern	101
5.1.2	Holographic imaging: Siemens star	103
5.1.3	Holographic reconstruction: Siemens star	105
5.1.4	Iterative reconstruction: Siemens star	109
5.1.5	Holographic imaging and reconstruction: Grid pattern	112
5.1.6	Resolution limit	114
5.1.7	Holographic imaging and reconstruction: 50 nm lines-and-spaces	117
5.2	Biological imaging	118

5.2.1 Dictyostelium discoideum cell imaging	118
5.3 Conclusions	120
6 Summary	121
A Fourier analysis	125
A.1 Fourier transform	125
A.2 Convolution theorem	125
A.3 Fourier derivative theorem	125
A.4 Friedel's law	125
B Image processing	127
B.1 Discrete Fourier transform	127
B.2 Grid spacing conversion	127
B.3 Sampling theorem	128
B.4 Oversampling	129
B.5 Oversampling of Fresnel pattern	132
B.6 Uniqueness of reconstruction	133
B.7 Source code in MATLAB	135
References	143

Introduction

The investigation of structure-property and structure-function relations is a leit-motif of condensed matter as of life sciences. Macroscopic phenomenological properties and material stoichiometries can in most cases be determined with the desirable accuracy. Likewise, biological function and the molecular players in living systems can be well identified and described. On the other hand the link of properties and functions to the three-dimensional structure of matter on the nanoscale is often missing. Therefore, there is still a significant need for more structure-resolving experimental capabilities, despite the tremendous progress in visible light and electron as well as scanning probe microscopies. These techniques can fully or partially resolve structures at the nanometer range, and in the case of transmission electron microscopy (TEM) or scanning tunneling microscopy (STM) even reach atomic resolution. However, a common and severe shortcoming is that these techniques can hardly image the properties of the undisturbed bulk. In the case of visible light, opacity, multiple scattering, and/or disturbances by using labels such as in fluorescence microscopy, can partially compromise the ability to probe structure in bulk specimens. In the case of scanning probe microscopy, bulk properties have to be derived from those of the investigated surface.

X-ray imaging is in principle a suitable and promising method to probe undisturbed bulk structure non-invasively under relevant environmental conditions. A necessary prerequisite to develop this technique was the advent of highly brilliant x-ray sources (synchrotrons, x-ray free-electron laser) and high performance x-ray detector arrays. Progress in x-ray optics is the third pillar needed to achieve the full potential of high resolution x-ray microscopy.

To date, many different experimental approaches exist to image nanoscale structures by x-ray beams, all of them characterized by individual assets and drawbacks. On the general leave, the methods can be classified into those that need coherent or partially coherent wavefronts, and those which work also with incoherent illumination. Furthermore, they can also be divided in scanning and full-field, as well as in lens based or lensless techniques, or in far-field and near-field (propagation based) imaging methods.

The most developed form of x-ray microscopy is zone plate-based x-ray microscopy, primarily applied in the soft x-ray spectral range. Fresnel zone plates replace the condenser and/or objective lenses known from conventional visible light microscopy. This method allows for very high resolution in the soft x-ray spectral range down to 12-15 nm in two-dimensional imaging [1] and of ≈ 50 nm in three-dimensional imaging (tomography) [2]. The resolution is not limited by the short x-ray wavelength (nm-to-Å range) but by the focusing properties of the respective optics.

The refractive index of x-rays is slightly lower than one which generally compromises the achievable focusing or imaging properties not only of lenses, but virtually for all x-ray optical devices, based on refraction, reflection or diffraction. Note that aside from Fresnel zone plates (diffractive optics) [3], small x-ray beam diameters can also be achieved by mirrors with low curvature (reflective optics) [4], and compound refractive lenses [5].

A conceptionally simple yet versatile imaging method can be implemented by scanning the focused beam across the sample, and measuring x-ray absorption, fluorescence, diffraction or differential phase contrast. In this case no (objective) lens is placed between sample and detector, making it particularly dose efficient. At the same time, a high degree of coherence is needed to achieve efficient focusing, and the resolution - at least at first sight - seems to be limited by the focal width.

On closer inspection, the situation changes for coherent focusing (coherent illumination), as in this case the resolution limit of the focal spot size can be overcome by inversion of the coherent far-field diffraction pattern. This approach which is based on a coherent wavefront is also denoted as lensless x-ray imaging or coherent x-ray diffractive imaging (CXDI). The idea of lensless imaging is that even if lenses or other optics are used as condensers, these should not limit the resolution. The first CXDI experiment was carried out using simply a pinhole [6] to select a coherent wavefront out of the partially coherent synchrotron beam. The resolution of the image is not limited by the focal spot but by the largest diffraction angle at which a statistically significant signal is recorded in the far-field. This method has been enhanced by using x-ray optics such as Fresnel zone plates [7] and compound refractive lenses [8]. The coherence condition was fulfilled either by reducing the beam size in front of the lens or by choosing objects with lateral extension below the coherence length. As in the pinhole CXDI experiments, the image resolution is much better than the focal spot size [9]. Importantly, with no optics between sample and detector, optical improvements and experimental design must focus on the optics of the illumination wavefront.

In this work we present advanced x-ray waveguide optics for the coherent illumination in lensless imaging. The particular advantages of using x-ray waveguides as quasi point-like sources for x-ray imaging are related to four aspects: Firstly, they act as coherence filter and decouple the coherence properties of the illumination from those of the primary source (undulator and/or beamline optics). Secondly, they provide a divergent exit beam, enabling an illumination wavefield which can be tailored in cross-section and curvature, e.g. simply by moving the sample along the optical axis. Thirdly, the divergence results in an extended far-field pattern which spreads the signal over many detector pixels in contrast to plane wave illumination, which usually necessitates the use of beamstops

leading to loss of information. Finally, reconstruction algorithms have been shown to converge faster for divergent illumination compared to plane wave illumination [7].

Indeed, the image formation and object reconstruction depend significantly on the properties of the illumination wave-field. Divergent illumination using x-ray waveguides enables a route to high resolution projection images. In the regime of hard x-rays, these images are predominantly formed by phase contrast, at least for nanoscale specimens. The divergent beams emitted from quasi-point sources also enable a simple and deterministic (holographic) reconstruction method by backpropagation [10]. However, as is well known, the reconstruction of in-line holograms leads to artifacts, such as the twin image problem. The situation can be significantly improved [11] by combining the divergent projection setting with iterative reconstruction algorithms [12, 13, 14].

Given the advantages of this form of propagation imaging and the progress in reconstruction algorithms, a pivotal challenge resides in the design and fabrication of suitable waveguides [15]. Up to now, the waveguides were severely limited in transmission and flux, restricting their use to high-contrast test structures with moderate resolution and long accumulation times [16, 17, 18].

To overcome these limits, the evanescent modes propagating inside the waveguide must be tailored such that the absorption is minimized. Enhanced transmission can be achieved by a two-component cladding with a suitable index profile [19, 20]. To this end, thin film deposition is a versatile fabrication technique enabling multiple design parameters to shape an optimized refractive index profile. However, two major problems occur if one aims at using this technology for the fabrication of x-ray waveguides. Firstly, optimized transmission is obtained only for rather thin slices, which are difficult to handle and to 'seal' with beam blocking materials. Depending on photon energy, thin slices (lamellae) of 200-600 μm thickness optimize the radiation transport and filtering properties, but are difficult to integrate into absorption apertures. Secondly, thin film optical films make up one-dimensional waveguides, but are not compatible, at first sight, with two-dimensional beam confinement and filtering. Extending the ideas of crossing orthogonal waveguides [21], we show that two-dimensionally (beam) confining waveguides can be achieved by means of a serial arrangement of two crossed planar waveguides. By optimal design and fabrication we achieve three advantages: 1.) the transmission is maximized by minimizing the length while blocking the radiative modes, 2.) the two focal planes can be brought into close proximity, and 3.) the compact design allows for an optical alignment in one step. Resulting from 1.), very small beam cross sections become amenable. In summary, the main goal of this thesis was to develop, to characterize and to optimize such two-component waveguides in a crossed geometry to cre-

ate suitable and powerful illumination sources for lensless x-ray imaging, as demonstrated by proof-of-concept experiments.

1 X-ray propagation imaging

Waveguide-based x-ray imaging involves diffraction of the waveguide field by the sample, propagation by free-space of the disturbed wave-field to the detector and reconstruction of the object from intensity measurements in the detection plane.

In section 1.1 we describe the theoretical background to propagate an arbitrary wave-field in free-space based on the scalar wave theory. Using suitable approximations we derive Fresnel and Fraunhofer diffraction pattern. In section 1.2 interaction of the x-ray wave-field with matter is considered leading to the projection approximation indicating that the object outgoing wave-field is directly related to the incoming waveguide field through the optical transmission function. Assuming plane wave illumination the different imaging regimes are illustrated by simulations as a function of the propagation distance of the object wave-field (section 1.3). We show that point-source illuminated Fresnel diffraction pattern can be considered as plane wave illuminated Fresnel diffraction pattern indicating that waveguide-based imaging can be related to parallel beam imaging by a variable transformation (section 1.4). In section 1.5 we discuss algorithms to retrieve the complete object function from intensity measurements in the detection plane. We focus on in-line holographic reconstruction and iterative reconstruction methods and present phase retrieval simulations illustrating the advantages and limitations by use of the different methods.

1.1 Propagation of x-rays in free-space

1.1.1 Wave equations in free-space

Propagation of electromagnetic waves is described by Maxwell's equations [22]. In the simplest case of free-space propagation, the Maxwell's equations in SI units are given by

$$\nabla \cdot \mathbf{E}(x, y, z, t) = 0, \quad (1.1)$$

$$\nabla \cdot \mathbf{B}(x, y, z, t) = 0, \quad (1.2)$$

$$\nabla \times \mathbf{E}(x, y, z, t) = -\frac{\partial \mathbf{B}}{\partial t}, \quad (1.3)$$

$$\nabla \times \mathbf{B}(x, y, z, t) = \varepsilon_0 \mu_0 \frac{\partial \mathbf{E}}{\partial t}, \quad (1.4)$$

in Cartesian coordinates (x, y, z) , i.e. in three-dimensional space and t as time. \mathbf{E} denotes the electric field, \mathbf{B} is the magnetic induction, ε_0 and μ_0 are respectively equal to the electrical permittivity and magnetic permeability of free space. As demonstrated in physics textbooks [23], the Maxwell's equations can be

transformed into the vacuum field equations which is in case of the electric field given by

$$\nabla^2 \mathbf{E}(x, y, z, t) = \varepsilon_0 \mu_0 \frac{\partial^2 \mathbf{E}(x, y, z, t)}{\partial t^2}. \quad (1.5)$$

In this vector theory the electromagnetic disturbance is specified by the electric field vector and the magnetic induction vector at each point in space and time. If polarization effects are negligible we can apply scalar theory and consider the single scalar field $\Psi(x, y, z, t)$ as a function of both position and time according to the vacuum field equation by [24]

$$\left(\frac{1}{c^2} \frac{\partial^2}{\partial t^2} - \nabla^2 \right) \Psi(x, y, z, t) = 0. \quad (1.6)$$

Here, we used the relation $c = v\lambda = \frac{1}{\sqrt{\mu_0 \varepsilon_0}}$ where c is the speed of light in vacuum, ν the frequency and λ the wavelength of the electromagnetic field. The spectral decomposition of a complex scalar function $\Psi(x, y, z, t)$ as a superposition of monochromatic fields describing a wave-field in a given volume of free space

$$\Psi(x, y, z, t) = \frac{1}{\sqrt{2\pi}} \int_0^\infty \psi_\omega(x, y, z) \exp(-i\omega t) d\omega, \quad (1.7)$$

is known as the analytic signal corresponding to the scalar electromagnetic disturbance [25]. Substituting Eq. (1.7) in Eq. (1.6), interchanging the order of differentiation and integration and finally applying the differentiation with respect to time results in

$$(\nabla^2 + k^2) \psi_\omega(x, y, z) = 0 \quad (1.8)$$

with the wave-number $k = \frac{\omega}{c}$ which depends on the angular frequency of the radiation $\omega = 2\pi\nu$. The time-independent equation (1.8) is known as the Helmholtz equation. It describes the development of the spatial wave-function $\psi_\omega(x, y, z)$ linked to a given monochromatic component of the spectral decomposition, i.e. the spatial component of a monochromatic wave-field.

1.1.2 Free-space propagator

In the following, we address the problem how to determine the propagated wave-field from the knowledge of the unpropagated wave-field. We follow the treatment of angular spectrum decomposition as presented in the textbooks of Goodman [26] and Paganin [23]. As sketched in Fig. 1.1, we consider two parallel planes $z = 0$ and $z = \Delta > 0$ with vacuum in between the planes, so that the

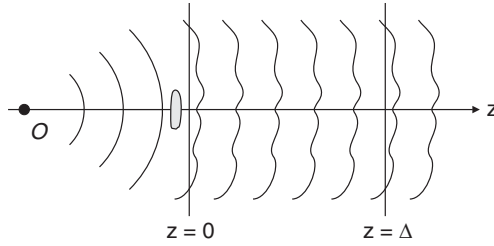


Figure 1.1: Schematic illustrating the diffraction problem for scalar electromagnetic fields. The point source, denoted by O is at $z < 0$ on the optical axis z and generates a spherical wave-field. The disturbed wave-field exiting an object is indicated by the wavy lines. Solving the diffraction problem amounts in obtaining the value of the spatial wave-function $\psi(x, y, z)$ over a plane $z = \Delta > 0$, knowing the value of ψ over the plane $z = 0$.

Helmholtz equation (1.8) is obeyed. The elementary plane waves $\psi^{(PW)}(x, y, z) = \exp[i(k_x x + k_y y + k_z z)]$ are solutions to the Helmholtz equation if $k_x^2 + k_y^2 + k_z^2 = k^2$ where (k_x, k_y, k_z) are the x , y and z components of the wave-vector \mathbf{k} of the plane wave. We now consider plane waves propagating at an angle with respect to the optical axis z in z -forward-direction. The solutions of the Helmholtz equation can be expressed in the form

$$\psi^{(PW)}(x, y, z) = \exp[i(k_x x + k_y y)] \exp\left[iz\sqrt{k^2 - k_x^2 - k_y^2}\right]. \quad (1.9)$$

where $\exp\left[iz\sqrt{k^2 - k_x^2 - k_y^2}\right]$ is known as the free-space propagator. In fact, using the value $\psi^{(PW)}(x, y, z = 0) = \exp[i(k_x x + k_y y)]$ of the plane wave at $z = 0$, we can determine the propagated value of the plane wave at $z > 0$ by multiplication with the propagation factor $\exp\left[iz\sqrt{k^2 - k_x^2 - k_y^2}\right]$. We can extend this method to arbitrary wave-fields $\psi(x, y, z)$ by applying the two-dimensional Fourier integral Eq. (A.2) to the unpropagated wave-field

$$\psi(x, y, z = 0) = \frac{1}{2\pi} \iint \tilde{\psi}(k_x, k_y, z = 0) \exp[i(k_x x + k_y y)] dk_x dk_y. \quad (1.10)$$

Here, $\tilde{\psi}(k_x, k_y, z = 0)$ denotes the Fourier transform of $\psi_\omega(x, y, z = 0)$ with respect to x and y . The terms k_x and k_y are the Fourier-space variables which are conjugate to the positions x , y . since Eq. (1.10) corresponds to a decomposition of the unpropagated wave-field into a linear combination of two-dimensional

plane waves $\exp[i(k_x x + k_y y)]$, we obtain the propagated wave-field by multiplying these plane wave components by the free-space propagator

$$\begin{aligned} \psi(x, y, z = \Delta) = & \frac{1}{2\pi} \iint \tilde{\psi}(k_x, k_y, z = 0) \exp \left[i\Delta \sqrt{k^2 - k_x^2 - k_y^2} \right] \\ & \times \exp [i(k_x x + k_y y)] dk_x dk_y. \end{aligned} \quad (1.11)$$

Free-space propagation may be written in compact form introducing the free-space diffraction operator $\mathcal{D}_\Delta = \mathcal{F}^{-1} \exp \left[i\Delta \sqrt{k^2 - k_x^2 - k_y^2} \right] \mathcal{F}$

$$\psi(x, y, z = \Delta) = \mathcal{D}_\Delta \psi(x, y, z = 0). \quad (1.12)$$

Hence, the numerical implementation of this method involves 3 steps [23]:

1. Apply the Fourier transform to the unpropagated wave-field $\psi(x, y, z = 0)$, with respect to x and y .
2. Multiply the obtained expression by $\exp \left[i\Delta \sqrt{k^2 - k_x^2 - k_y^2} \right]$.
3. Apply the inverse Fourier transform to the obtained result, with respect to k_x and k_y .

Note that the numerical implementation is also possible in case of backpropagating a known propagated wave-field to obtain the unpropagated wave-field by using the free-space propagator $\exp \left[-i\Delta \sqrt{k^2 - k_x^2 - k_y^2} \right]$.

1.1.3 Fresnel diffraction

Imaging experiments in this thesis are carried out in the paraxial approximation. Thus, all of the non-negligible wave components of the field make a small angle with respect to the optical axis z [23]. This assumption is valid since the divergence of the waveguide beam, which may be considered as the illumination source at $z = 0$, is on the order of 1 mrad [19]. Hence, using the following binomial approximation leads to

$$\sqrt{k^2 - k_x^2 - k_y^2} \approx k - \frac{k_x^2 + k_y^2}{2k}. \quad (1.13)$$

Substituting the term on the right side of Eq. (1.13) into the free-space diffraction operator \mathcal{D}_Δ yields

$$\psi(x, y, z = \Delta) \approx \mathcal{D}_\Delta^F \psi(x, y, z = 0) \quad (1.14)$$

$$= \exp(i k \Delta) \mathcal{F}^{-1} \exp \left[\frac{i\Delta(k_x^2 + k_y^2)}{2k} \right] \mathcal{F} \psi(x, y, z = 0), \quad (1.15)$$

where \mathcal{D}_Δ^F is known as the Fresnel diffraction propagator. The numerical implementation in the paraxial approximation is analogue to the implementation presented in section 1.1.2 whereas the free-space propagator is replaced by the kernel of the Fresnel propagator $\exp\left[i\Delta(k_x^2 + k_y^2)/2k\right]$, and in a last step the resulting expression is multiplied by the constant phase factor $\exp(ik\Delta)$.

Eq. (1.15) can be rewritten using the convolution formalism Eq. (A.3)

$$\psi(x, y, z = \Delta) = \psi(x, y, z = 0) * h(x, y, \Delta) \quad (1.16)$$

The function $h(x, y, \Delta)$, which is called the real-space form of the Fresnel propagator, is given by

$$\begin{aligned} h(x, y, \Delta) &\equiv \frac{1}{2\pi} \exp(ik\Delta) \mathcal{F}^{-1} \exp\left[\frac{-i\Delta(k_x^2 + k_y^2)}{2k}\right] \\ &= -\frac{ik \exp(ik\Delta)}{2\pi\Delta} \exp\left[\frac{ik(x^2 + y^2)}{2\Delta}\right]. \end{aligned} \quad (1.17)$$

Applying the convolution theorem to Eq. (1.15) by taking the result of Eq. (1.17), the Fresnel diffraction integral can be deduced

$$\begin{aligned} \psi(x, y, z = \Delta) &= -\frac{ik \exp(ik\Delta)}{2\pi\Delta} \iint_{-\infty}^{\infty} \psi(x', y', z = 0) \\ &\quad \times \exp\left[\frac{ik}{2\Delta}((x - x')^2 + (y - y')^2)\right] dx' dy' \end{aligned} \quad (1.18)$$

By expansion of the quadratic term in Eq. (1.18) the Fresnel diffraction integral can be written in the following form

$$\begin{aligned} \psi(x, y, z = \Delta) &= -\frac{ik \exp(ik\Delta)}{2\pi\Delta} \exp\left[\frac{ik(x^2 + y^2)}{2\Delta}\right] \\ &\quad \times \iint_{-\infty}^{\infty} \psi(x', y', z = 0) \exp\left[\frac{ik}{2\Delta}(x'^2 + y'^2)\right] \\ &\quad \times \exp\left[\frac{-ik}{\Delta}(xx' + yy')\right] dx' dy'. \end{aligned} \quad (1.19)$$

This corresponds to the Fresnel-Kirchhoff diffraction integral in paraxial approximation.

1.1.4 Fraunhofer diffraction

A further approximation is often valid in x-ray waveguide experiments. The diffracted field at $z = \Delta$ is in the far-field for propagation distances that are very

large compared to the characteristic length scale of the unpropagated wave-field, for instance the guiding core diameter d of the waveguide. This diffraction pattern is called Fraunhofer diffraction pattern and the approximation is valid if

$$N_F = \frac{kd^2}{2\pi\Delta} \ll 1. \quad (1.20)$$

N_F is known as the Fresnel number. By using this condition, the first exponent in the Fresnel diffraction integral (1.19) may be left out

$$\begin{aligned} \psi(x, y, z = \Delta) = & -\frac{ik \exp(ik\Delta)}{2\pi\Delta} \exp\left[\frac{ik(x^2 + y^2)}{2\Delta}\right] \\ & \times \iint_{-\infty}^{\infty} \psi(x', y', z = 0) \exp\left[\frac{-ik}{\Delta}(xx' + yy')\right] dx' dy' \end{aligned} \quad (1.21)$$

This is known as the Fraunhofer diffraction integral. We can write Eq. (1.21) in a compact form making use of Eq. (A.2) for the two-dimensional Fourier transform

$$\psi(x, y, z = \Delta) = -\frac{ik \exp(ik\Delta)}{\Delta} \exp\left[\frac{ik(x^2 + y^2)}{2\Delta}\right] \tilde{\psi}(k_x = \frac{kx}{\Delta}, k_y = \frac{ky}{\Delta}, z = 0). \quad (1.22)$$

Thus, in the Fraunhofer approximation the field distribution propagated to the plane $z > \Delta$ is obtained by applying the 2D Fourier transform to the field distribution at the plane $z = 0$ in a first step and in a second step, multiplying the result by a complex-valued prefactor.

1.2 Interaction of x-rays with matter

1.2.1 Refraction and absorption of x-rays

In case of wave propagation in a uncharged, non-conducting and non-magnetic medium, the Helmholtz equation in the framework of scala theory reads [22]

$$[\nabla^2 + n^2(x, y, z)k^2] \psi(x, y, z) = 0 \quad (1.23)$$

The quantity $n(x, y, z)$ is known as the index of refraction of the medium and is related to the electrical permittivity $\epsilon(x, y, z)$ of the medium by

$$n(x, y, z) = c \sqrt{\epsilon(x, y, z)\mu_0} = \sqrt{\frac{\epsilon(x, y, z)}{\epsilon_0}}. \quad (1.24)$$

The refractive index for x-rays is typically very close to unity and this index is often expressed in the form [27]

$$n = 1 - \delta + i\beta, \quad (1.25)$$

where δ and β are real numbers. Away from absorption edges, the dispersive part δ of the index of refraction yields

$$\delta = \frac{2\pi\rho_e r_e}{k^2}. \quad (1.26)$$

Here, ρ_e is the electron density and r_e denotes the Thomson scattering length. The imaginary part β which describes the absorption of the x-rays in the medium is related to the linear attenuation coefficient μ by

$$\beta = \frac{\mu}{2k}. \quad (1.27)$$

The values of the dispersive and imaginary parts δ and β are on the order of $10^{-5} - 10^{-7}$ and $10^{-7} - 10^{-9}$, respectively, for hard x-rays.

1.2.2 The projection approximation

In extension to 1.1.2, we now consider two parallel planes $z = 0$ and $z = z_0$, with an object of thickness $t(x, y)$ in between the planes (see Fig. 1.2 (a)). The monochromatic plane wave, which impinges parallel to the propagation axis z at $z = 0$, is then scattered. The perturbed wave $\psi_S(x, y, z)$, which is a solution of the inhomogeneous Helmholtz equation (1.23), may be expressed as a product of the unscattered plane wave $\exp(ikz)$ with an envelope $\psi_E(x, y, z)$

$$\psi_S(x, y, z) = \psi_E(x, y, z) \exp(ikz) \quad (1.28)$$

Note that both the field and its envelope have the same intensity distribution, i.e. $|\psi_S(x, y, z)|^2 = |\psi_E(x, y, z)|^2$, as $\exp(ikz)$ is only a linear phase factor. In the paraxial approximation, neglecting the second derivative in z , Eq. (1.23) yields

$$\left(2ik \frac{\partial}{\partial z} + \nabla_{\perp}^2 + [n^2(x, y, z) - 1]k^2 \right) \psi_E(x, y, z) = 0, \quad (1.29)$$

where the transverse Laplacian is given by $\nabla_{\perp}^2 = \partial^2/\partial x^2 + \partial^2/\partial y^2$. The projection approximation consists of assuming that the value of the wave-field at the exit-surface $z = z_0$, is entirely determined by the phase and the amplitude shifts that are accumulated along streamlines of the unscattered beam [23]. Fresnel diffraction is negligible only if the radius of the first Fresnel zone corresponding

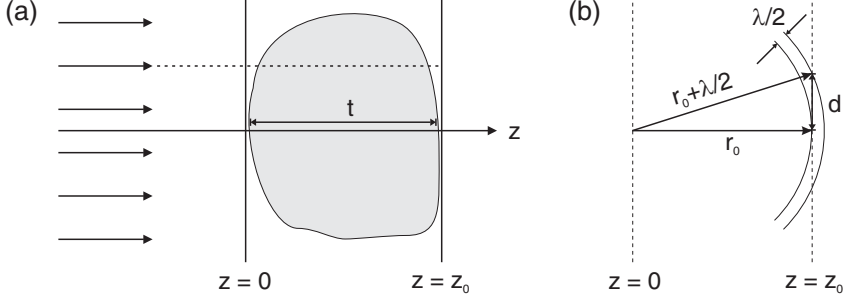


Figure 1.2: (a) Schematic illustrating the propagation of a monochromatic plane wave through a scattering medium of thickness t . The scattering medium is indicated by the grey region and lies in between the planes $z = 0$ and $z = z_0$. (b) The radii r_0 and $r_1 = r_0 + \lambda/2$ delimits the first Fresnel zone. From geometrical considerations follow $d = \sqrt{\lambda r_0 + \lambda^2/4}$ and further $d \approx \sqrt{\lambda t}$ for $r_0 = t$ and $\lambda \ll t$.

to propagation in the object is small compared to the spatial resolution d (see Fig. 1.2 (b))

$$\sqrt{\lambda t} < d. \quad (1.30)$$

This is the usual limitation on the resolution due to Fresnel diffraction [28] and it limits the thickness to 1 μm at an x-ray wavelength of 0.1 nm and a resolution of 10 nm. If condition Eq. (1.30) is fulfilled we can neglect the term $\nabla_{\perp}^2 \psi_E(x, y, z)$ in Eq. (1.29)

$$\frac{\partial}{\partial z} \psi_E(x, y, z) \approx \frac{k}{2i} [1 - n^2(x, y, z)] \psi_E(x, y, z). \quad (1.31)$$

The solution of the partial differential equation (1.31) is given by

$$\psi_E(x, y, z = z_0) \approx \exp \left(-ik \int_{z=0}^{z=z_0} [\delta(x, y, z) - i\beta(x, y, z)] \right) \psi_E(x, y, z = 0), \quad (1.32)$$

where we made use of the first order approximation in δ and β

$$1 - n^2(x, y, z) \approx 2[\delta(x, y, z) - i\beta(x, y, z)]. \quad (1.33)$$

The phase shift $\phi(x, y)$, resulting from the interaction of the modulated wave with matter, reads

$$\phi(x, y) = -k \int_{z=0}^{z=z_0} \delta(x, y, z) dz. \quad (1.34)$$

For a single-material object of projected thickness $t(x, y)$, Eq. (1.34) reduces to

$$\phi(x, y) = -k\delta t(x, y). \quad (1.35)$$

The angle of total reflection $\sqrt{2\delta}$ [27] sets an upper limit to the maximum angular deviation of a wave-field. Accordingly, assuming no multiple reflections of the wave-field propagating through the medium, the projection approximation holds if $\sqrt{2\delta}t < d$ [28]. This yields a thickness of $t < 2 \mu\text{m}$ for $\delta = 10^{-5}$ and $d = 10 \text{ nm}$, close to the result obtained using condition Eq. (1.30). According to Eq. (1.35), the maximum tolerable phase shift is $\phi(x, y) < 1.4 \text{ rad}$ for $\lambda = 0.1 \text{ nm}$. The linear attenuation term is given by

$$2k \int_{z=0}^{z=z_0} \beta(x, y, z) dz = 2k\beta t(x, y) = \mu t(x, y) = \mu_t(x, y). \quad (1.36)$$

The wave-field $\psi_E(x, y, z = z_0)$ then reads

$$\begin{aligned} \psi_E(x, y, z = z_0) &\approx \exp [i\phi(x, y) - \mu_t(x, y)/2] \psi_E(x, y, z = 0) \\ &= \tau(x, y) \psi_E(x, y, z = 0). \end{aligned} \quad (1.37)$$

Here, we introduced the optical transmission function $\tau(x, y)$. In case of weak objects where ϕ and μ are small compared to 1, we may approximate the optical transmission function

$$\tau(x, y) \approx 1 + i\phi(x, y) - \mu_t(x, y)/2. \quad (1.38)$$

Finally, we may express the weak object solution, relating the incoming plane wave to the object outgoing wave $\psi_S(x, y, z = z_0)$, as

$$\psi_S(x, y, z = z_0) = \tau(x, y) \exp(ikt). \quad (1.39)$$

The validity of the weak object approximation is confirmed for the experimental conditions in the hard x-ray energy range [29, 30].

1.3 Imaging regimes

We can now express the propagated wave-field of an object outgoing wave in case of a plane wave illuminated object. Within the Fresnel and the weak object approximation (see section 1.1.3 and 1.2.2), the wave-field in Fourier space at $z \geq 0$ is given by

$$\begin{aligned} \tilde{\psi}(k_x, k_y, z) &= \tilde{\tau}(k_x, k_y) \tilde{h}(k_x, k_y, z) \\ &\approx [\delta_D(k_x, k_y) + i\phi(k_x, k_y) - \tilde{\mu}_t(k_x, k_y)/2] \\ &\quad \times \exp(ikz) \exp \left[-iz(k_x^2 + k_y^2)/2k \right], \end{aligned} \quad (1.40)$$

where δ_D denotes the Dirac delta function representing the directly transmitted beam. To first order in ϕ and μ the corresponding intensity $I = |\psi|^2$ is given in Fourier space by [31]

$$\tilde{I}(k_x, k_y) \approx \delta_D(k_x, k_y) + 2\tilde{\phi}(k_x, k_y) \sin \chi - \tilde{\mu}_t(k_x, k_y) \cos \chi \quad (1.41)$$

with $\chi = (z/2k)(k_x^2 + k_y^2)$. The terms $\sin \chi$ and $\cos \chi$ are known as the phase and amplitude contrast transfer functions (CTF), respectively, of the Fresnel diffraction pattern. Fig. 1.3 (a) shows the one-dimensional CTFs as a function of the normalized Fourier component $\sqrt{z/2\pi k} k_x$, i.e. normalized with respect to the radius of the first Fresnel zone [32]. The CTFs indicate that the image formation is determined by the spatial frequencies which are transmitted depending on the properties of the phase and amplitude components. Accordingly, different imaging regimes are expected as presented in the following:

Contact plane regime: The intensity distribution at the exit plane of the object shows a maximum amplitude contrast and due to the zero in the phase CTE, no phase contrast is visible.

Direct phase contrast regime: With increasing distance z absorption decreases and phase contrast starts to develop. At $\sin \chi = 1$ phase features of the object around this value appear in direct contrast whereas it is unlikely that all features of the imaged object have same characteristic lengths. More importantly, in the near-field imaging conditions, we may put $\sin \chi = \chi$ and by neglecting absorption Eq. (1.41) then becomes

$$\tilde{I}(k_x, k_y) \approx \delta_D(k_x, k_y) + \frac{z}{k}(k_x^2 + k_y^2)\tilde{\phi}(k_x, k_y), \quad (1.42)$$

which is known as the transport-of-intensity equation (TIE) [33]. Applying the Fourier derivative theorem Eq. (A.4) the intensity in real space yields

$$I(x, y) = 1 - \frac{z}{k} \nabla_{\perp}^2 \phi(x, y), \quad (1.43)$$

i.e. contrast from a pure phase object corresponds to the Laplacian of the phase shift. In experiments, direct contrast imaging is usually carried out using a small source to account for the spatial coherence condition. Limitations of direct contrast imaging includes the strong dependence on the detector resolution (pixel size) and correspondingly small field of view (FOV) due to low magnification factors (see section 1.4). On the other hand, this method is relative insensitive to polychromaticity in the radiation source, making this technique interesting for imaging using broad bandwidth in-house sources.

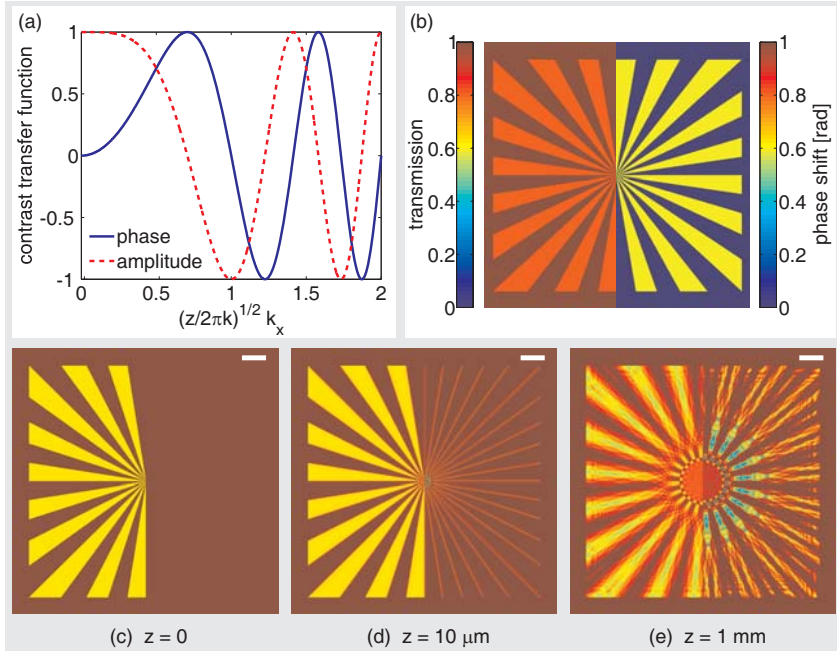


Figure 1.3: (a) Amplitude and phase contrast transfer functions as a function of $\sqrt{z/2\pi k} k_x$. The Siemens star (b) is divided into one half amplitude object of 80% transmission and one half phase object of 0.6 rad phase shift. (c-e) Intensity pattern of the plane wave illuminated Siemens star in the different imaging regimes at 10 keV, the scale bar is $1 \mu\text{m}$. In the contact plane (c) only the amplitude object is visible. With increasing distance (d) the phase object becomes visible and first interference fringes at the edges appear. (e) Further increasing of the distance z leads to 2 phenomena: The interference fringes in the outer regions of lower spatial frequencies becomes larger and the direct resemblance to the object gets more and more lost (holographic regime) towards the center of the object. In the inner part of highest spatial frequencies the resemblance to the object is lost due to the strongly varying CTF. The semirings in (e) of constant transmission and phase shift values correspond to the zeros in the respective contrast transfer functions.

Holographic regime: At $\chi > \pi$ both phase and amplitude lose direct resemblance to the object, becoming in fact holograms. Holographic imaging needs a highly monochromatic and coherent source of small beam cross-section to fully exploit resolution limits. In this case, the phase can be retrieved using holo-

graphic reconstruction (see section 1.5.1). For very large propagation distances z the recorded diffraction pattern is said to be in the far-field. The resolution does not necessary depend on the source size but then, more elaborated algorithms are needed to reconstruct the object (see section 1.5.2).

Fig. 1.3 (b) shows a Siemens star test object divided into a pure amplitude and a pure phase object. As the object has a large range of spatial frequency, the imaging regimes at different propagation distances in Fig. 1.3 (d)-(e) merge for large features to small features from direct contrast to holographic contrast.

1.4 Fresnel scaling theorem

The Fresnel scaling theorem states that a point-source illuminated Fresnel diffraction pattern can be considered as a Fresnel diffraction pattern obtained by plane wave illumination [23].

Within the paraxial and the projection approximation, the wave-field $\psi^{(\infty)}(x, y, z = 0)$ at the exit-surface of an object in case of plane-wave illumination is related to exit-surface wave-field $\psi^{(z_1)}(x, y, z = 0)$ for point-source illumination through

$$\psi^{(z_1)}(x, y, z = 0) = \psi^{(\infty)}(x, y, z = 0) \exp \left[\frac{ik}{2z_1}(x^2 + y^2) \right]. \quad (1.44)$$

Here, z_1 denotes the distance of the point-source from the exit-surface plane $z = 0$ of the object. Inserting Eq. (1.44) into the Fresnel diffraction integral Eq. (1.19) yields

$$\begin{aligned} \psi^{(z_1)}(x, y, z = z_2) &= -\frac{ik \exp(ikz_2)}{2\pi z_2} \exp \left[\frac{ik(x^2 + y^2)}{2z_2} \right] \\ &\times \iint_{-\infty}^{\infty} \psi^{(\infty)}(x', y', z = 0) \\ &\times \exp \left[\frac{ik}{2}(x'^2 + y'^2) \left(\frac{1}{z_2} + \frac{1}{z_1} \right) \right] \\ &\times \exp \left[\frac{ik}{z_2}(xx' + yy') \right] dx' dy'. \end{aligned} \quad (1.45)$$

The geometrical magnification M for point-source illumination, which relates the source size at the exit-surface plane to the illuminated area at the detector plane $z = z_2$, can be expressed by

$$M = \frac{z_1 + z_2}{z_1}, \quad (1.46)$$

and hence

$$\frac{1}{z_2} + \frac{1}{z_1} = \frac{M}{z_2}. \quad (1.47)$$

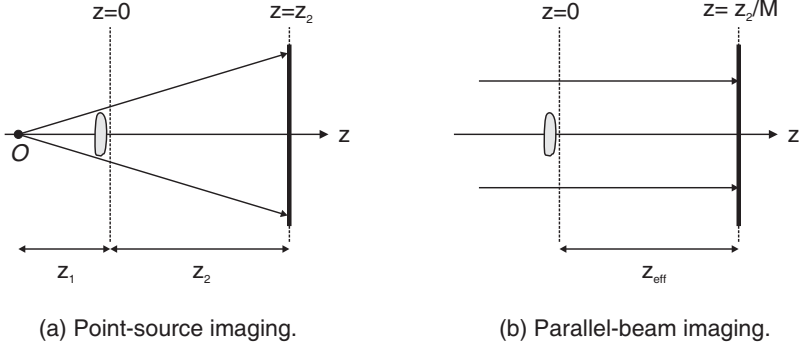


Figure 1.4: Analogy between point-source imaging (a) and parallel-beam imaging (b) under the paraxial and the projection approximation: The diffraction pattern of a point-source illuminated sample recorded at a distance sample-detector z_2 can be taken as the diffraction pattern of a parallel-beam illuminated sample recorded at a distance sample-detector $z_{\text{eff}} = z_2 / M$.

Using Eq. (1.47) the intensity of the propagated wave-field $I^{(z_1)}(x, y, z = z_2) = |\psi^{(z_1)}(x, y, z = z_2)|^2$ can be written as

$$I^{(z_1)}(x, y, z = z_2) = -\frac{k^2}{4\pi z_2^2} \times \left| \iint_{-\infty}^{\infty} \psi^{(\infty)}(x', y', z = 0) \exp \left[\frac{ikM}{2z_2} (x'^2 + y'^2) - \frac{ik}{z_2} (xx' + yy') \right] dx' dy' \right|^2. \quad (1.48)$$

In the limit of $z_1 \rightarrow \infty$, i.e. $M \rightarrow 1$, Eq. (1.48) becomes

$$I^{(\infty)}(x, y, z = z_2) = -\frac{k^2}{4\pi z_2^2} \times \left| \iint_{-\infty}^{\infty} \psi^{(\infty)}(x', y', z = 0) \exp \left[\frac{ik}{2z_2} (x'^2 + y'^2) - \frac{ik}{z_2} (xx' + yy') \right] dx' dy' \right|^2. \quad (1.49)$$

Using direct substitution, it turns out that Eq. (1.48) and Eq. (1.49) are linked to one another via the Fresnel scaling theorem

$$I^{(z_1)}(x, y, z = z_2) = M^{-2} I^{(\infty)} \left(\frac{x}{M}, \frac{y}{M}, z = \frac{z_2}{M} \right). \quad (1.50)$$

Thus, up to a multiplicative constant, the intensity observed at the position (x, y) on the detector is equivalent to the intensity observed at the position

$(x/M, y/M)$ on the detector placed at an effective distance $z_{eff} = z_2/M$ in case of a plane wave illuminated object. Equally, an object that is illuminated by an x-ray waveguide, which acts as quasi point-like source, may be treated as a parallel beam illuminated object. In the following we discuss the above assumption. Using typical parameters $d = 20$ nm for the waveguide guiding core diameter, $z_1 = 1$ mm and $\lambda = 0.1$ nm, the Fresnel number Eq. (1.20) yields $N_F = d^2/(\lambda z_1) = 0.004 \ll 1$, i.e. the Fraunhofer approximation is valid. Hence, the waveguide beam incident on a sample may be described as a spherical wave enveloped by the far-field pattern of the waveguide. We can account for the envelope by introducing an aperture function $A(x, y)$ in Eq. (1.44) [19]

$$A(x, y) \psi^{(z_1)}(x, y, z = 0) = A(x, y) \psi^{(\infty)}(x, y, z = 0) \exp \left[\frac{ik}{2z_1} (x^2 + y^2) \right]. \quad (1.51)$$

Taking the typical divergence of the waveguide beam on the order of 1 mrad into account, the aperture A has a diameter of $a \approx 1$ μm at a distance $z_1 = 1$ mm. Under the condition $z_1 \ll z_2$, satisfied for the experimental conditions, the effective distance is given by $z_{eff} \approx z_1$. Since $\sqrt{\lambda z_{eff}} < a$ for $\lambda = 0.1$ nm Fresnel diffraction effects are negligible, i.e. we can consider $A(x, y) \psi^{(\infty)}(x, y, z = 0)$ as a parallel beam in good approximation. Thus, the waveguide quasi-point source illuminated Fresnel pattern can be considered as a parallel beam illuminated Fresnel pattern. To reduce the effect of the waveguide beam envelope, numerical reconstruction is carried out on the measured diffraction pattern normalized by the empty waveguide farfield pattern recorded at a distance $z_1 + z_2$.

1.5 Object reconstruction

Just as in other x-ray diffraction experiments, only the intensity of the wavefield diffracted at an object is recorded in lensless imaging, phase information is lost (phase problem). The task of the object reconstruction is to determine the complex-valued object function $\psi(x, y)$, i.e. amplitude and phase in the object plane, from measurements of the diffracted intensity $I = |\tilde{\psi}(x, y)|^2$ in the detection plane.

In this thesis two types of algorithms are used to reconstruct the object from simulated and experimentally obtained diffraction patterns: In-line holographic reconstruction and iterative phase retrieval methods. The in-line holographic reconstruction is an one-step deterministic reconstruction where no additional information about the object is needed, and can be applied if the scattered wave of the object interferes with the direct beam. Inherently, numerical implementation of iterative algorithms is more complicated and the obtained solution might be unique but the reconstruction process is not deterministic. However, iterative algorithms can overcome the twin-image problem (see section 1.5.1)

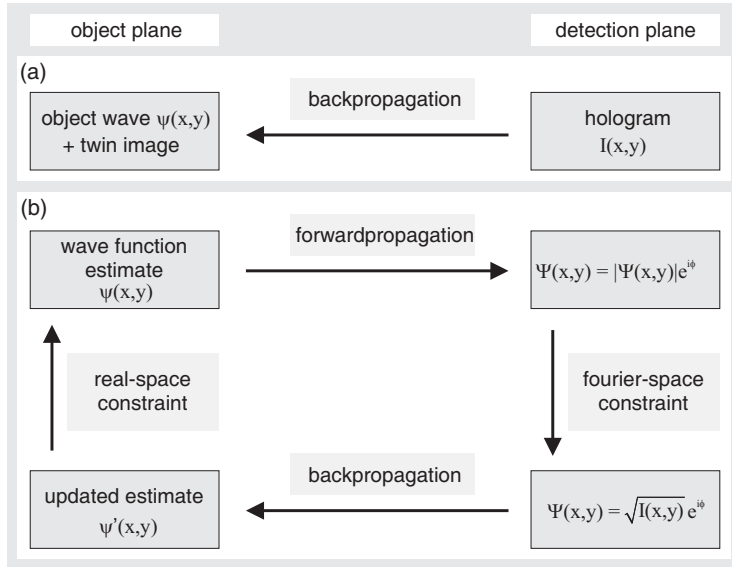


Figure 1.5: In-line holographic reconstruction (a) and general iterative phase retrieval algorithm (b). For further information see main text.

of holographic reconstruction. Apart from the object reconstruction, iterative phase retrieval methods enable the reconstruction of illumination functions such as the waveguide near-field.

Fig. 1.5 illustrates schematically the differences in the phase retrieval methods. The holographic reconstruction consists of applying the free-space diffraction propagator \mathcal{D} (see section 1.1.2¹) on the measured intensity I_H of the hologram, see subfigure (a). In the iterative algorithms the measured intensity is used as the Fourier-space constraint in the detection plane. Additionally, the iterative methods rely on a priori knowledges on the object wave $\psi(x, y)$ in real space, i.e. the real-space constraints in the object plane. Starting from a first guess of the object wave in the object plane, the object is reconstructed by cycling between object and detection plane until a suitable figure of merit singles out a possible solution. A more detailed explanation of the phase retrieval methods is presented in the following sections.

¹Equally, one can also use the Fresnel approximated backpropagation method, see section 1.1.3.

1.5.1 In-line holographic reconstruction

In-line holography or in-line holographic reconstruction was first published by Denis Gabor in 1948 [10]. The idea was to detect the intensity distribution ('in-line hologram') emitted from a sample and then illuminate the in-line hologram by the same reference wave used to illuminate the sample as illustrated in Fig. 1.6. In this 'two-step process' of recording and reconstruction the complex object wave is retrieved by the interference pattern of the unscattered reference wave ψ_r and the scattered object wave ψ_o . In this thesis recording is carried out using detectors and the reconstruction is performed numerically on the computer. The interference pattern of the unscattered and the scattered wave is given by

$$I_H = |\psi_r(x, y, z_0) + \psi_o(x, y, z_0)|^2. \quad (1.52)$$

Assuming that the incoming wave is a plane wave, i.e. $\psi_o(x, y, z_0) \approx A$ where A is a given complex constant, Eq. (1.52) becomes

$$I_H \approx |A|^2 + A^* \psi_o(x, y, z_0) + A \psi_o^*(x, y, z_0) + |\psi_o(x, y, z_0)|^2. \quad (1.53)$$

In waveguide-based x-ray holography the scattered wave is assumed to be much weaker than the reference wave and the term $|\psi_o(x, y, z_0)|^2$ can thus be left out. After recording of the digitized image $I_H(x, y)$, the image is reconstructed by applying the free-space propagator \mathcal{D}_{z-z_0} (see section 1.1.2) on the exit-surface wave-field $AI_H(x, y)$ of the in-line hologram to propagate the wave-field by a distance $z - z_0$, where $z \geq z_0$. Therefore the reconstructed wave-field $\psi_{recon}(x, y, z)$ is given by [23]

$$\begin{aligned} \psi_{recon}(x, y, z) &\equiv \mathcal{D}_{z-z_0}[AI_H(x, y)] \\ &\approx \mathcal{D}_{z-z_0}[A|A|^2 + |A|^2\psi_o(x, y, z_0) + A^2\psi_o^*(x, y, z_0)]. \end{aligned} \quad (1.54)$$

Thus, at the exit surface of the in-line hologram, the reconstructed wave-field $\psi_{recon}(x, y, z)$ consists of a superposition of three terms:

- a term $A|A|^2$ which, up to a multiplicative constant $|A|^2$, is equal to the reference beam (indicated by the solid lines in Fig. 1.6 (b));
- a term $|A|^2\psi_o(x, y, z_0)$ which, apart of a multiplicative constant $|A|^2$, is equal to the scattered wave-field (indicated by the dotted lines in Fig. 1.6 (b)), which creates a virtual image A' of the object;
- a term $A^2\psi_o^*(x, y, z_0)$ which, apart of a multiplicative constant, is equal to the complex conjugate of scattered the wave-field (indicated by the dash-dot lines in Fig. 1.6 (b)), creating a real image A'' of the object.

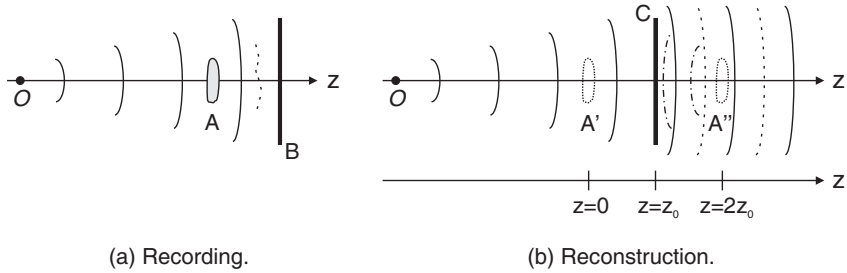


Figure 1.6: Recording and reconstruction of an in-line hologram (schematic adapted from [23]). (a) The sample A is illuminated by a coherent spherical wave-field, originating from the point-source O. The wave-field exiting A is a superposition of the unscattered (solid line) and the scattered (dotted line) wave-field. The interference pattern is recorded as an in-line hologram on the plane B. (b) The in-line hologram situated at the plane C, now without the sample, is illuminated by the same spherical wave as in the recording step. The wave-field downstream of the hologram is determined by three terms, which correspond to the reference beam (solid line), a virtual image A' of the sample (dotted line), and a real image A'' of the sample (dash-dot line). The latter term causes the twin-image problem in in-line holography.

Computational reconstruction is simplified if $z = 2z_0$ in Eq. (1.54) [23]:

$$\psi_{recon}(x, y, 2z_0) \approx A|A|^2 \exp(ikz_0) + |A|^2 \psi_o(x, y, 2z_0) + A^2 \mathcal{D}_{z_0}[\psi_o^*(x, y, z_0)]. \quad (1.55)$$

The free-space propagation of a two-dimensional coherent field through a distance Δz gives the complex conjugate of the free-space propagation of the complex conjugate of that coherent field through a distance $-\Delta z$

$$\mathcal{D}_{z_0}[\psi_o^*(x, y, z_0)] = [\psi_o(x, y, z = 0)]^*. \quad (1.56)$$

This is a result of the reciprocity theorem [23]. Applying this theorem, Eq. (1.55) leads to

$$\begin{aligned} \psi_{recon}(x, y, z = 2z_0) &= A|A|^2 \exp(ikz_0) + |A|^2 \psi_o(x, y, 2z_0) + A^2 [\psi_o(x, y, z_0)]^* \\ &= A^2 [A \exp(-ikz_0) + \psi_o(x, y, z = 0)]^* \\ &\quad + |A|^2 \psi_o(x, y, z = 2z_0). \end{aligned} \quad (1.57)$$

Eq. (1.57) shows that we obtain two contributions by reconstructing the recorded image. The complex conjugate of the reconstructed exit-surface wave-field given

by the first term and a superposed 'twin-image' given by the second term. This also points out the fundamental limit of in-line holography: The quality of the reconstructed image is generally adulterated by the overlap of the real and the virtual image, i.e. the reconstructed image shows undesired artefacts.

We close out this section with two remarks. For numerical implementation, we have used the free-space propagator \mathcal{D}_{z_0-z} instead of \mathcal{D}_{z-z_0} . Physically, it corresponds to illuminate the hologram from the opposite side, i.e. to place the source shown in Fig. 1.6 (b) from the left-hand side to the right-hand side. In reconstructed image, sample features of higher electron density then correspond to lower phase values compared to those of lower electron density features. The retarded phase values are in agreement with the expectations as the phase shift $\phi = -k\delta t(x, y)$ in the optical transmission function is a negative value. Further, the choice of \mathcal{D}_{z_0-z} enables to directly compare phase distributions of holographically and iteratively reconstructed images. We account for the illuminating wave on the exit surface wave-field by applying \mathcal{D}_{z_0-z} on the measured hologram normalized by the empty waveguide far-field intensity. In numerical simulation we set $A = 1$ leading to an additional phase offset in the reconstructed exit surface wave-field. In both, phase reconstruction of measured and simulated holograms, we hence only consider relative phase shifts.

1.5.2 Iterative phase retrieval methods

Gerchberg-Saxton (GS) algorithm

The first algorithm to retrieve iteratively the complete wave function from intensity measurements in the object and detection planes was proposed by Gerchberg and Saxton [12]. The so-called Gerchberg-Saxton (GS) algorithm can be expressed by [23]

$$\psi(x, y) = \lim_{N_{\text{it}} \rightarrow \infty} (\mathcal{P}_1 \mathcal{F}^{-1} \mathcal{P}_2 \mathcal{F})^{N_{\text{it}}} [|\psi(x, y)| e^{i\phi_{\text{initial}}(x, y)}], \quad (1.58)$$

in case of Fraunhofer diffraction, i.e. forward and inverse Fourier transform is used to propagate the respective wave functions. \mathcal{P}_1 and \mathcal{P}_2 are projections operators which are substitutes for the real-space and Fourier-space constraints

$$\mathcal{P}_1 = |\psi(x, y)| \quad \text{and} \quad \mathcal{P}_2 = |\mathcal{F}\psi(x, y)|. \quad (1.59)$$

The parameter N_{it} is the number of times that the operator $\mathcal{P}_1 \mathcal{F}^{-1} \mathcal{P}_2 \mathcal{F}$ is iterated, and $\phi_{\text{initial}}(x, y)$ is the initial guess for the unknown phase which can be chosen as a random distribution of phases. The intensity in the object plane can usually not be measured in lensless x-ray experiments restricting the use of the GS algorithm to pure phase object imaging where the real-space constraint

consists of setting the amplitude of the object wave to one.

Error-reduction (ER) algorithm

Fienup proposed an extension to the GS algorithm, the so-called error-reduction (ER) algorithm, allowing for the reconstruction of complex-valued object function only from the measured intensity in the detection plane by relaxing the real-space constraints:

$$\psi(x, y) = \lim_{N_{\text{it}} \rightarrow \infty} (\mathcal{P}'_1 \mathcal{F}^{-1} \mathcal{P}_2 \mathcal{F})^{N_{\text{it}}} \psi_{N_{\text{it}}=0}(x, y), \quad (1.60)$$

where $\psi_{N_{\text{it}}=0}(x, y)$ is a random initial guess for the complex wave function and the projection operator \mathcal{P}'_1 a known constraint in the object plane. As a widely used constraint, assuming the support of $\psi(x, y)$ is given by the region \mathcal{S} of the x, y plane, we have

$$\mathcal{P}'_1 \psi(x, y) = \begin{cases} \psi(x, y), & (x, y) \in \mathcal{S}, \\ 0, & \text{otherwise.} \end{cases} \quad (1.61)$$

The support \mathcal{S} is the area embedding the object and can be estimated as the half diameter of the autocorrelation of the diffraction pattern which is given by $\mathcal{F}^{-1}[|\mathcal{F}\psi(x, y)|^2]$.

Hybrid Input-Output (HIO) algorithm

As it is the case with the GS algorithm, the distance between an iterate and the next $\|\psi_{N_{\text{it}}+1} - \psi_{N_{\text{it}}}\|$ is non-increasing in the ER algorithm [12]. However, both algorithms suffer often from stagnation problems where $\|\psi_{N_{\text{it}}+1} - \psi_{N_{\text{it}}}\|$ remains approximately constant for a very large number of iterations. To solve this problem, Fienup developed the Hybrid Input-Output (HIO) algorithm valid for $n > 0$:

$$\psi_{N_{\text{it}}+1}(x, y) = \begin{cases} \psi'_{N_{\text{it}}}(x, y), & (x, y) \in \mathcal{S}, \\ \psi_{N_{\text{it}}}(x, y) - \beta \psi'_{N_{\text{it}}}(x, y), & \text{otherwise,} \end{cases} \quad (1.62)$$

with $\psi_{N_{\text{it}}}(x, y) = (\mathcal{P}'_1 \mathcal{F}^{-1} \mathcal{P}_2 \mathcal{F})^{N_{\text{it}}} \psi_{N_{\text{it}}=0}(x, y)$ and $\psi'_{N_{\text{it}}}(x, y) = (\mathcal{F}^{-1} \mathcal{P}_2 \mathcal{F}) \psi_{N_{\text{it}}}(x, y)$. Here, $\psi_{N_{\text{it}}}(x, y)$ can be considered as an input for a non-linear operation impelling the output $\psi'_{N_{\text{it}}}(x, y)$. The so-called feedback parameter β governs the degree of hybridization of the input with the output outside the support and is usually chosen to be a real number between 0.5 and 1. This method attracts the iterate $\psi_{N_{\text{it}}+1}(x, y)$ to near-solutions but, in contrast to the GS and ER algorithm, prevents it to be trapped into local minima and therefore optimizes the convergence of the algorithm [34]. However, depending on the exact problem, the ER

algorithm may converge to a satisfactory solution much faster than the HIO algorithm which might tend to move away from a near-solution (good estimation).

Apart of the GS, the ER and the HIO algorithm, other algorithms such as the shrink-wrapping method were proposed and combinations of different algorithms are used to improve the reconstruction convergence [35]. Further, many of these existing methods may be defined within a general projection formulation [36] in which the well known GS and HIO algorithms arises as special cases.

1.5.3 Phase retrieval simulations

In this section we present applications of the aforementioned phase retrieval methods on simulated Fraunhofer diffraction pattern and Fresnel diffraction pattern. Considerations on discretization of data and on oversampling criteria of diffraction pattern as well as on constraint sufficiency and uniqueness criteria of the reconstruction have to be taken into account.

The numerical implementation of an object reconstruction from its far-field pattern by using the HIO algorithm is shown in Fig. 1.7. In this simulation a Siemens star test object with a transmission of $T = \exp(k\beta t) = 0.96$ and a phase shift of $\phi = 0.4$ rad corresponding to the properties of a $t = 500$ nm thick tantalum layer at 17.5 keV is used. The simulation is carried out assuming plane wave illumination with $\psi^{PW} = 1$. Fig. 1.7 (a) and (b) shows the amplitude and the phase distribution of the optical transmission (object) function, respectively. The size of the object is chosen to $A_S = 256^2$ pixels which is the area where the object function is non-zero (support of the object function). To fulfill the oversampling criterion, the object is placed in an array of $A_{FOV} = 512^2$ pixels, i.e. four times the size of the object support. The array is filled with zeros in order to create a high-density area surrounding the object². The oversampling ratio $\sigma = \frac{A_{FOV}}{A_S} = 4$ is derived from the Shannon sampling theorem [38] (see section B.3 and B.4). The autocorrelation of the object is given by the Fourier transform of the diffraction pattern shown in Fig. 1.7 (c). The autocorrelation support allows to control the sampling sufficiency. The autocorrelation extension and thus its support is confined on A_{FOV} as shown in Fig. 1.7 (d), i.e. the diffraction pattern is oversampled in the sense of Shannon.

²Physically, the high density area corresponds to a mask which completely absorbs the incoming x-rays. In experiments, it is unlikely that the sample is isolated by a mask. Reconstruction of diffraction data is rather carried out on $1 - \psi(x, y)$ equivalent to the reconstruction of $\psi(x, y)$ as $\mathcal{F}[1 - \psi(x, y)] = \delta(k_x, k_y) - \tilde{\psi}(k_x, k_y)$ and the missing low frequency data corresponding to $\delta(k_x, k_y)$ are left out in the reconstruction. This method is based on Babinet's principle which is also valid in the Fresnel regime [37].

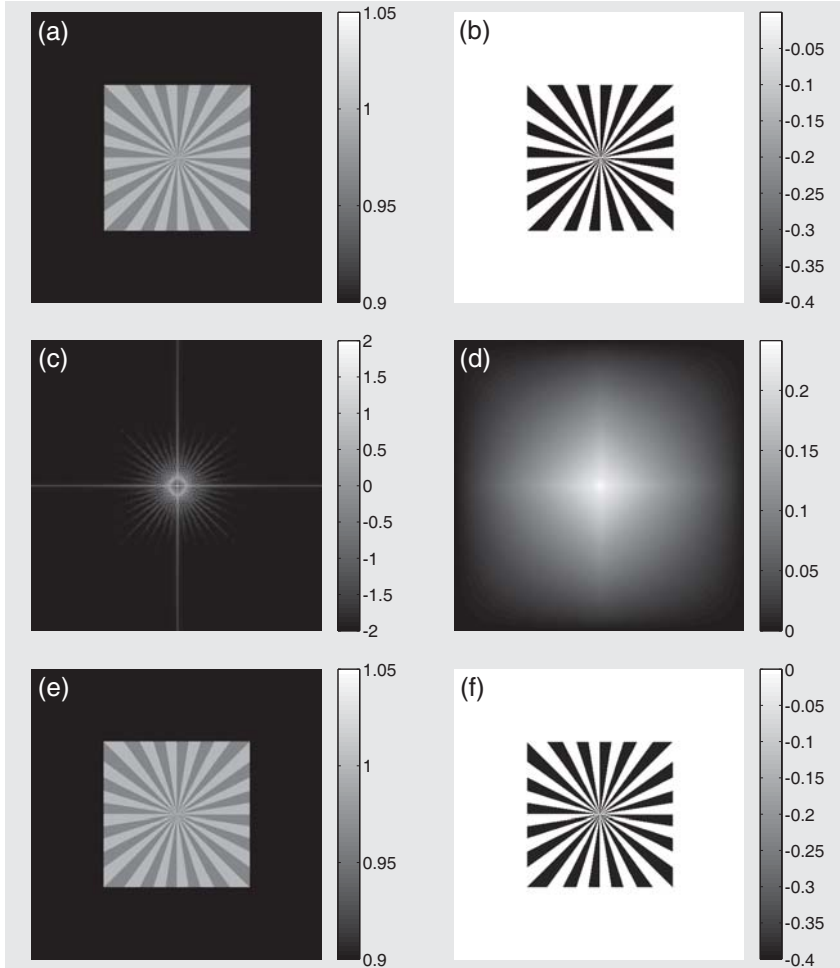


Figure 1.7: (a) Amplitude and (b) phase (in [rad]) of the Siemens star test object. The computational field of view is $A_{FOV} = 512^2$ (c) Farfield diffraction pattern (intensity in log. scale) and (d) corresponding autocorrelation pattern. The autocorrelation extension is confined on A_{FOV} , i.e the oversampling criterion is fulfilled. Reconstructed (e) amplitude and (f) phase after $N_{it} = 1000$ iteration steps using the HIO algorithm with $\beta = 1$. Finest details of the object are reconstructed. The reconstruction error χ^2 is below 10^{-4} .

The Fourier-space constraint in the simulation is given by the root of the far-field intensity. As real-space constraint a support of size A_S filled with ones and embedded in a zero-array of size A_{FOV} is used. The iterative reconstruction starts in the object plane with a random complex field $R = a_0 R_m \exp[-i\phi_0 R_m]$ which was numerically generated as an initial guess. The equally distributed pseudo-random variable R_m on the interval $m = [0, 1]$ and the parameters $a_0 = 0.5$ and $\phi_0 = 0.05$ are assigned to each pixel. The feedback parameter β is set to one. Fig. 1.7 (e) and (f) show the reconstructed amplitude and phase, respectively, after $N_{it} = 1000$ iteration steps. Smallest features of the object are reconstructed both in amplitude and phase. The reconstruction error χ^2 is calculated using the following relation [34]:

$$\chi^2 = \frac{1}{N^2} \sum_{x,y} (|\tilde{\psi}(x,y)| - \sqrt{I(x,y)})^2, \quad (1.63)$$

where χ is the error metric, $\tilde{\psi}(x,y)$ the Fourier transform of the reconstructed object function (multiplied by the support), $I(x,y)$ the intensity corresponding to the diffraction pattern and N^2 the number of pixels (x,y) at which the intensity was determined (corresponding to $N^2 = 512^2$ in the simulation). The low reconstruction error $\chi^2 = 4.7 \cdot 10^{-5}$ underlines the efficiency of the HIO algorithm. Repeated computational trials have all shown reconstruction errors below 10^{-4} demonstrating the robustness of the method. Note that the presented simulation is an idealized case, as neither artifacts due to a pertubated illumination function nor noise were introduced in the diffraction pattern. Whereas the HIO algorithm enabled the succesful reconstruction of the Siemensstar, reconstruction of the same object using the ER algorithm failed as the algorithm stagnated in a non-unique solution, i.e. the ER algorithm is trapped in a local minimum [39] (see section B.6).

Let us now consider phase retrieval simulations of diffraction patterns in the holographic (Fresnel) regime. First, we choose a pure phase Siemens star object with $T = 1$ and $\phi = 0.4$ rad simulated for an photon energy $E = 17.5$ keV. The object size and the computational field of view is $A_S = 256^2$ and $A_{FOV} = 256^2$ pixels, respectively. Fig. 1.8 (a) shows the hologram of the Siemens star simulated for an energy $E = 17.5$ keV, a pixel size of $\Delta x \times \Delta y = 80^2$ nm and a propagation distance $z = 4.5$ mm. Aliasing close to the 'sharp edges' is visible on the hologram. The aliasing effect is due to the use of discrete Fourier transformation (see section B.1) in simulation and does not occur on measured hologram. Aliasing of the propagator used to create the hologram is observed too if $\Delta x \leq \lambda z / L_x$ where L_x is the extent of the computational field of view in x-direction [40] (see sec-

tion B.5). However for the chosen parameters $\lambda z/L_x = 16 \text{ nm} < \Delta x$, i.e. aliasing should be suppressed³.

The Siemens star can be holographically reconstructed by applying the free-space diffraction operator \mathcal{D}_{-z} on the hologram intensity $I(x, y)$

$$\psi(x, y) = \mathcal{D}_{-z}I(x, y). \quad (1.64)$$

Fig. 1.8 (b) shows the phase distribution of the holographic reconstruction. The global structure as well as smallest details in the center of the Siemens star are reconstructed. However, reconstruction is adulterated by twin-image artifacts. Further, the holographic reconstruction does not properly recover the phase distribution of the void and the phase shifting areas of the Siemens star object as illustrated by the histogram shown in Fig. 1.8 (f). In fact, the histogram of the phase distribution would ideally exhibit two sharp peaks distant of 0.4 rad.

The iterative reconstruction methods presented in section 1.5.2 are adapted according to the Fresnel regime. Using the free-space diffraction operator \mathcal{D} , the GS algorithm yields

$$\psi(x, y) = \lim_{N_{\text{it}} \rightarrow \infty} (\mathcal{P}_1 \mathcal{D}_{-z} \mathcal{P}_2 \mathcal{D}_z)^{N_{\text{it}}} \psi_{N_{\text{it}}=0}(x, y), \quad (1.65)$$

where $\psi_{N_{\text{it}}=0}(x, y)$ is a random complex-valued initial guess R of the object function in the sample plane. As the test image is a pure phase object we set the amplitude of the wave function to one (real-space constraint \mathcal{P}_1) at each iteration step in the sample plane. Fig. 1.8 (c) shows the phase reconstruction of the Siemens star after applying $N_{\text{it}} = 2000$ iteration steps of the GS algorithm. In analogy to holographic method, smallest details in the center of the Siemens star are reconstructed. On the other hand, less reconstruction artifacts are observed and phase recovery is improved as demonstrated by the histogram of the phase distribution in Fig. 1.8 (g). Additional real-space constraints in iterative methods can further improve the reconstruction convergence [41, 42]. For this purpose, we enlarged the computational field of view to $A_{\text{FOV}} = 512^2$ pixels leaving the object size and the pixel size unchanged. Using the additional support constraint \mathcal{P}'_1 presented in Eq. (1.61) the iterative method yields

$$\psi(x, y) = \lim_{N_{\text{it}} \rightarrow \infty} (\mathcal{P}_1 \mathcal{P}'_1 \mathcal{D}_{-z} \mathcal{P}_2 \mathcal{D}_z)^{N_{\text{it}}} \psi_{N_{\text{it}}=0}(x, y), \quad (1.66)$$

which we denote as ER-GS algorithm.

³We have used the free-space propagator for simulation whereas the used oversampling condition is derived for the (approximated) Fresnel propagator. Nevertheless the holograms are found to be identical for both propagators.

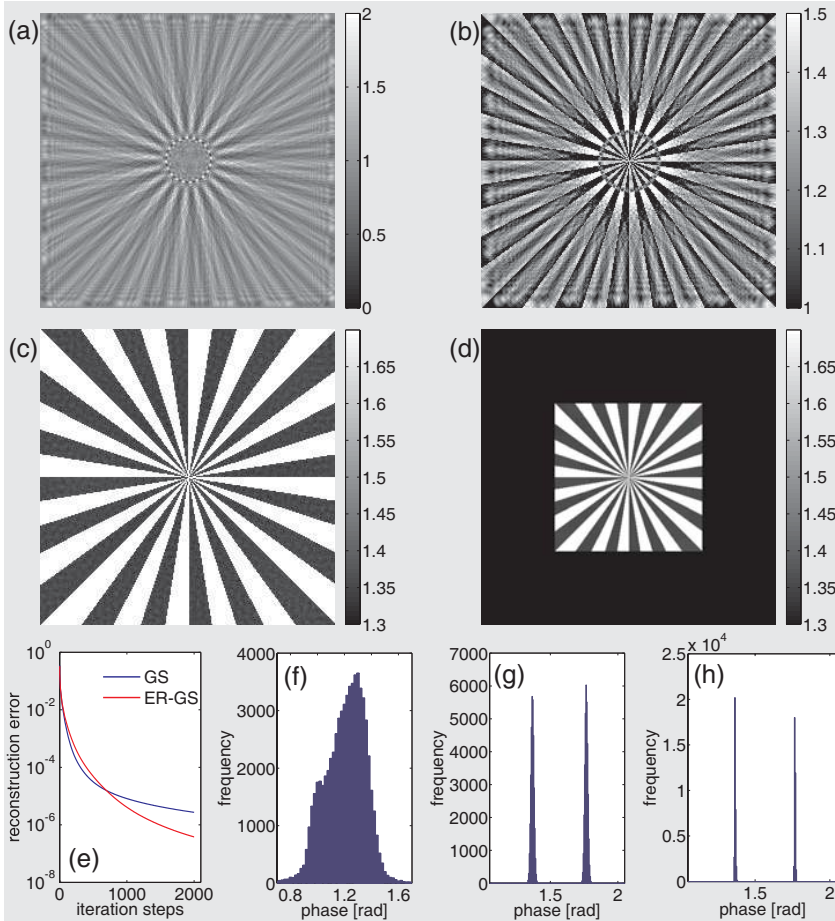


Figure 1.8: (a) Hologram of the Siemens star object ($T = 1$, $\phi = 0.4$), simulated for an energy $E = 17.5$ keV, a pixel size $\Delta x \times \Delta y = 80^2$ nm and a distance $z = 4.5$ mm. (b) Holographic reconstruction, phase in [rad]. Phase reconstruction using (c) GS and (d) ER-GS algorithm. (e) The reconstruction error of the ER-GS algorithm is lower than of the GS algorithm. (f)-(g) Histograms corresponding to the phase distributions in (b)-(d), respectively, exhibiting the improved phase recovery of the ER-GS algorithm compared to GS and holographic reconstruction.

Fig. 1.8 (d) shows the phase reconstruction of the Siemens star after applying $N_{\text{it}} = 2000$ iteration steps of the ER-GS algorithm. Compared to the GS algorithm the reconstruction convergence is optimized as underlined by the run of the error curves in Fig. 1.8 (e). The improved phase recovery is further illustrated by the two distinct peaks in the histogram of the ER-GS reconstructed phase distribution shown in Fig. 1.8 (h). For both, GS and ER-GS reconstruction, the phase shift of 0.40 rad is in excellent agreement with the expected phase shift of 0.4 rad.

Finally, we consider reconstruction of complex-valued object function in the holographic regime without knowledge of the amplitude in the object plane. Fig. 1.9 (a) shows the hologram of a Siemens star test object with $T = 0.96$ and $\phi = 0.4$ simulated for the same parameters as for the pure phase object hologram and a computational field of view $A_{\text{FOV}} = 512^2$ pixels. Fig. 1.9 (b) shows the phase distribution of the holographic reconstruction as obtained by using Eq. (1.64). Compared to the holographic reconstruction presented in Fig. 1.8 (b) the phase distribution shows similar characteristics except enhanced interference effect at the outer region of the object due to diffraction at the mask edges. Fig. 1.9 (c) shows the phase reconstruction of the Siemens star after applying $N_{\text{it}} = 50$ iteration steps of the ER algorithm

$$\psi(x, y) = \lim_{N_{\text{it}} \rightarrow \infty} (\mathcal{P}'_1 \mathcal{D}_{-z} \mathcal{P}_2 \mathcal{D}_z)^{N_{\text{it}}} \psi_{N_{\text{it}}=0}(x, y). \quad (1.67)$$

Fig. 1.9 (d) shows the phase reconstruction of the Siemens star after applying $N_{\text{it}} = 50$ iteration steps of the HIO algorithm

$$\psi_{N_{\text{it}}+1}(x, y) = \begin{cases} \psi'_{N_{\text{it}}}(x, y), & (x, y) \in \mathcal{S}, \\ \psi_{N_{\text{it}}}(x, y) - \beta \psi'_{N_{\text{it}}}(x, y), & \text{otherwise,} \end{cases} \quad (1.68)$$

where the input and output are given by $\psi_{N_{\text{it}}}(x, y) = (\mathcal{P}'_1 \mathcal{D}_{-z} \mathcal{P}_2 \mathcal{D}_z)^{N_{\text{it}}} \psi_{N_{\text{it}}=0}(x, y)$ and $\psi'_{N_{\text{it}}}(x, y) = (\mathcal{D}_{-z} \mathcal{P}_2 \mathcal{D}_z) \psi_{N_{\text{it}}}(x, y)$, respectively, in the Fresnel regime. In contrast to pure phase object phase retrieval the histograms of the iteratively reconstructed objects do not exhibit improved phase recovery compared to holographic reconstruction as shown in Fig. 1.9 (f) and (h), respectively. Nevertheless diffraction effects at the edges of the reconstructed image are efficiently suppressed by iterative algorithms. The error metrics of the ER and HIO algorithm shown in Fig. 1.9 (e) are rather low whereas image reconstruction is not of high quality. Longer runs of the algorithms further decrease the reconstruction errors without improving reconstruction. Hence, both algorithms were trapped in a local minimum.

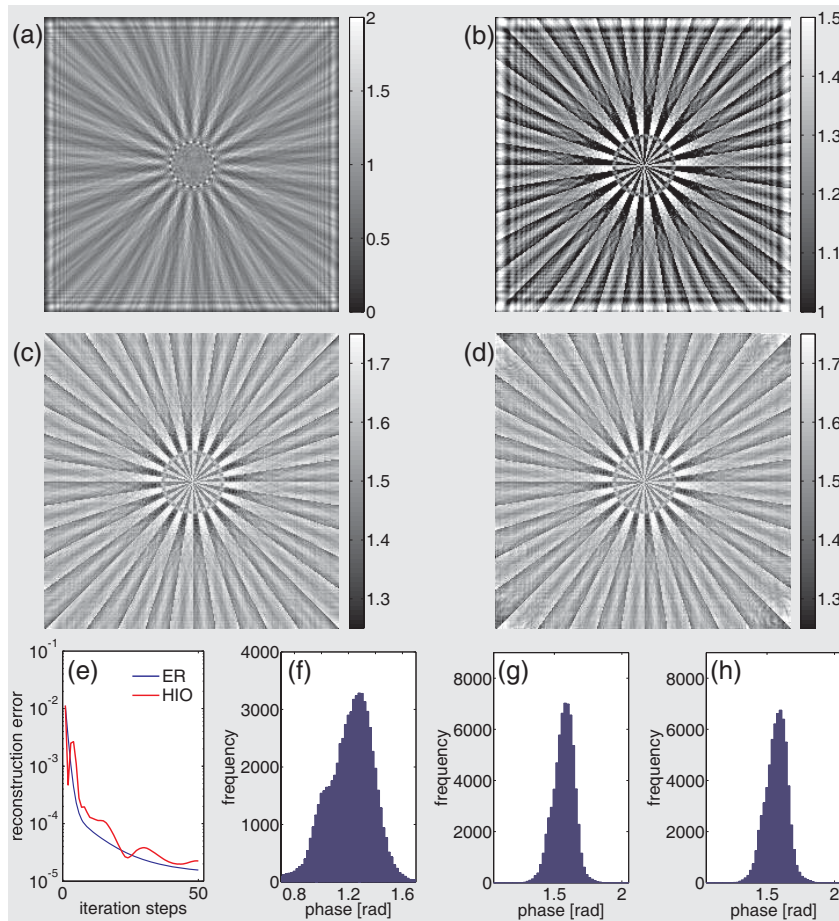


Figure 1.9: (a) Hologram of the Siemens star object ($T = 0.93$, $\phi = 0.4$) simulated for the same parameters as in Fig. 1.8 (a) besides $A_{\text{FOV}} = 512^2$ pixels. (b) Holographic reconstruction, phase in [rad]. Phase reconstruction using (c) ER and (d) HIO algorithm. (e) The reconstruction error of the HIO algorithm is lower than of the ER algorithm. Both error curves yield a minimum at only few iteration steps. (f)-(g) Histograms corresponding to the phase distributions in (b)-(d), respectively, showing no improvements in phase recovery of the iterative methods compared to holographic reconstruction.

This last example of phase retrieval simulation reveals limitation of iterative object reconstruction. It has been shown that complex-valued reconstruction are intrinsically harder than real-valued reconstruction⁴ as it demands a stronger support constraint [43, 44, 45, 46]. The use of a tight but rectangular support might therefore not be sufficient to reconstruct efficiently the complex-valued object function from the Fresnel pattern [44]. To us it is still an open question if improved complex-valued reconstruction from Fresnel pattern of the convex⁵ and centrosymmetric Siemens star object without knowledge of the amplitude in the object plane can be achieved by more elaborated support constraints and/or iterative algorithms. On the other hand, pure phase object reconstruction enabling the use of additional real-space constraints noticeably improves phase recovery. Fortunately, biological samples consisting of low electron density elements act as pure phase objects in the hard x-ray energy range (see section 5.2).

1.6 Conclusion

We have shown that propagation of undisturbed and disturbed waveguide field in free-space can be carried out using free-space or Fresnel diffraction operator and simple Fourier transform depending on the propagation distance. The waveguide-field disturbed by diffraction from a sample is expressed by the product of the optical transmission function with the undisturbed wave-field in the projection approximation. Simulation of the object wave for different propagation distances and feature sizes of the object illustrate the possible imaging regimes. Depending on the imaging regime wave-field in the detection plane can be associated to exit object wave-field using the introduced backpropagation techniques. In particular, the Fresnel pattern of a sample illuminated by a waveguide can be treated as parallel beam propagated Fresnel pattern of the object exit wave after suitable variable transformation. Since in x-ray imaging experiments only the intensity of the object wave is measured we have presented phase retrieval algorithms based on single-step holographic and iterative reconstruction methods. Simulations show that for waveguide-based imaging, a priori

⁴Complex-valued objects are described by the optical transmission function $\tau(x, y) = \exp [i\phi(x, y) - \mu_t(x, y)/2]$ within the projection approximation. For physically thin sample the attenuation term $\mu_t(x, y) = 2k\beta t(x, y)$ can be discarded and the transmission function yields $\tau(x, y) = \exp [i\phi(x, y)]$ for complex-valued pure phase object. If further ϕ is small compared to one the optical transmission function can be approximated by $\tau(x, y) \approx 1 + i\phi(x, y)$. Under this condition, the imaginary unit i is only a multiplicative term in propagation and reconstruction is real-valued.

⁵Recall that in Euclidean space, an object is convex if for every pair of points within the object, every point on the straight line segment that joins them is also within the object.

knowledge of the object leading to strong real-space constraints considerably improves the phase recovery in reconstruction.

2 Waveguide optics

In the previous chapter we have treated image generation and reconstruction based on idealized x-ray sources, i.e. plane waves and spherical waves. In this chapter we present a concept for realization of a waveguide-based point-like (secondary) x-ray source⁶.

We start with a general overview of x-ray optics followed by a section on x-ray waveguides (section 2.1). Propagation inside planar waveguides is studied using the concept of mode propagation by means of analytical calculations and numerical simulations (see section 2.2). We discuss the influence of the mode structure on the coherence and transmission properties (2.3). Finally, we study the near-field and the exit wave-field propagation in the Fresnel and the Fraunhofer regime using a novel waveguide design offering significantly enhanced efficiency (section 2.4).

2.1 State of the art in x-ray optics

The development of x-ray optics plays a key role for improving high resolution imaging using synchrotron radiation. In this context, the aim is to focus the radiation to small beam sizes and eventually enhance the degree of coherence of the x-ray beam in order to ideally get a coherent nanofocus.

X-ray optics can be classified into reflective, diffractive, refractive and absorbing optical elements as shown in Fig. 2.1. Reflective optics such as multilayer mirrors have the advantage of very high gains ($10^5 - 10^6$), i.e. low intensity losses with respect to the incoming synchrotron beam [4, 48, 49]. Focusing can be achieved by elliptical curvatures of the mirrors as in the case of Kirkpatrick-Baez (KB) optics. Quite small spot sizes of $48 \times 46 \text{ nm}^2$ have been reported in the hard x-ray energy regime at 15 keV [50]. Only recently, one-dimensionally beam confinement of sub-10 nm have been demonstrated using a laterally graded multilayer mirror [51]. In contrast to waveguides, mirrors are one-to-one projections of the wave-field in the sense that the degree of coherence of the focal spot is limited to the coherence properties of the synchrotron beam.

The same holds for the most prominent diffractive and refractive optical elements, Fresnel zone plates (FZP) and compound refractive lenses (CRL), respectively. The FZP usually consists of a suitable circular absorbing grating where the highly absorbing material gold with the refractive index n_2 is electron deposited into a pre-structured resist on a low absorbing Si_3N_4 foil. The focal spot size is limited by the thickness of the outer rings of the grating, i.e. the aspect ratios which can be fabricated. Sub-15 nm two-dimensionally beam confinement have

⁶Contents of this chapter have been published in [47] and [20].

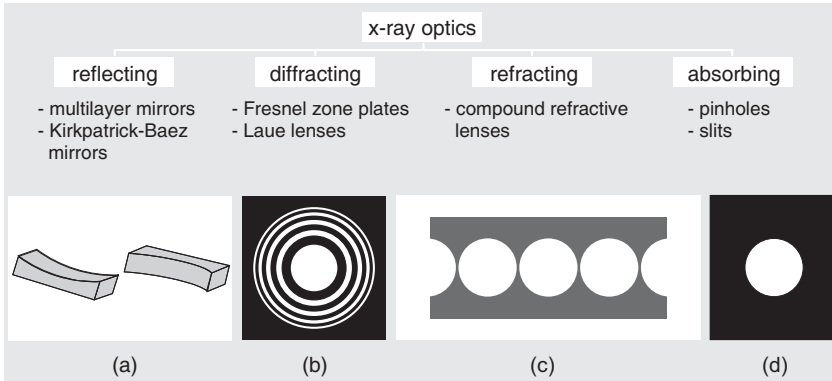


Figure 2.1: Overview on different classes of x-ray optics used for x-ray imaging. Schematics of the Kirkpatrick-Baez mirrors (a), the Fresnel zone plate (b), the compound refractive lenses (c) [53] and the pinhole (d).

been reported at ~ 700 eV and the efficiency was on the order of 1% [1, 3]. In the hard x-ray range significantly higher aspect ratios are needed to preserve the efficiency. FZPs with an aspect ratio of 20 and an outmost zone width of 45 nm reach a beam confinement of approximately 40 nm at 8 keV [52].

Hole array lenses were the first type of CRL manufactured [54]. The lenses consisted of an aluminium or beryllium metal bar with a row of drilled holes in it. Other CRL types exist such as bubble compound refractive lenses (BCRL) or alligator lenses [55, 56]. Highest beam confinement has been achieved by nanofocusing refractive lenses (NFL) made of a large number of lenses in silicon that have parabolic shape. A focal spot size of 47×55 nm² at 21 keV has been reported by two crossed NFLs [5]. Compared to multilayer mirrors the flux density gain is about 1-2 orders of magnitude lower [9].

Finally, x-ray imaging experiments are also carried out using absorbing optical elements such as beam limiting apertures. A pinhole consists of an absorbing foil, e.g. gold, with a small hole up to sub-1 μm diameter in the centre usually fabricated by focused ion beam (FIB). It is used amongst other techniques for holography and ptychography [57, 58]. Compared to the previously mentioned optical elements, the degree of coherence is enhanced with respect to the primary beam. The main disadvantage is the loss of intensity as the photon flux not passing through the aperture is completely absorbed.

As discussed in [47], x-ray waveguides can be used to filter hard x-ray beams [15, 17, 16, 59], being an alternative to beam confinement with conventional x-ray optics such as pinholes. Waveguides can thus provide localized and highly

coherent beams with two-dimensional cross sections down to about $d \approx 10$ nm [60] for diffraction studies at significantly reduced sample volume [61], as well as for coherent x-ray imaging and holography [57, 18, 62]. For optimized high transmission waveguide design [20], simulated transmission can reach values above 90%, if the waveguide is illuminated coherently, i.e. by a plane wave. Furthermore, the coherence properties and cross section of the beam are decoupled from the primary source. Over-illumination and stray radiation, often accompanying other forms of x-ray focusing, is efficiently blocked by the cladding and cap layers, since the radiation in the near-field is confined to $\approx d$. And finally, the photon flux exiting the waveguides can be significantly enhanced by using focusing optics such as KB mirrors, FZPs or CRLs as pre-focusing optics.

2.2 Planar waveguides

The symmetric slab waveguide design is shown in Fig. 2.2 with n_1 and n_2 being the refractive index of the guiding layer and the cladding, respectively.

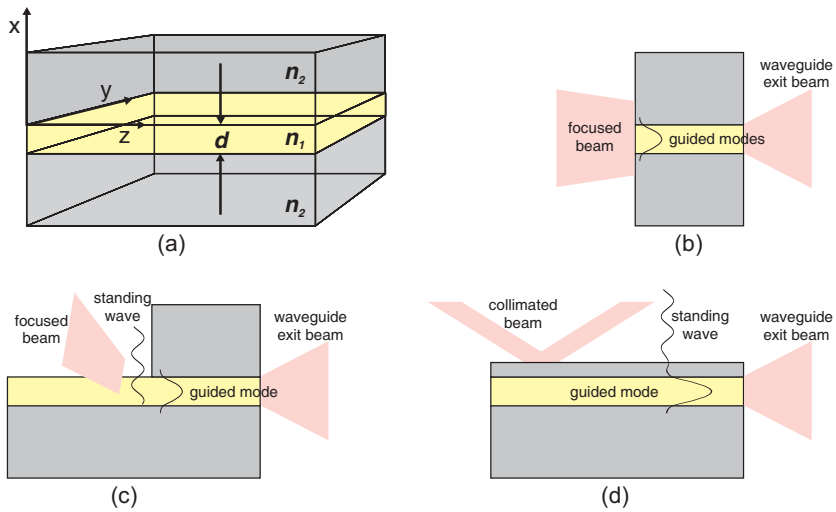


Figure 2.2: (a) Schematic of a dielectric slab waveguide. Front coupling of a prefocused beam directly into the front face of the planar waveguide (b) or via a standing wave above the substrate (c). (d) Flux density enhancement using a collimated beam which resonantly excites a guided mode through a thin upper cladding layer.

The first x-ray waveguide experiment was demonstrated by Spiller and Segmüller in the resonant beam coupler (RBC) scheme where the different waveguide modes are excited by varying the incidence angle through an evanescent wave-field which penetrates the upper cladding layer [63]. The coherent wave-field exiting the waveguide is at worst superposed by strongly reflected and transmitted (primary) beams which may compromise x-ray imaging experiments. To circumvent this severe drawback, we chose the front coupler (FC) scheme where the incident beam is coupled in at the front face of the waveguide. Contrarily to the RBC, no intrinsic flux enhancement is achieved by the FC, but a significant flux density gain compared to the primary synchrotron beam can be obtained by using pre-focusing optics as mentioned in the previous section. Coupling of a pre-focused beam into planar waveguides have been demonstrated using linear FZP or CRL via a standing wave above the substrate first [64, 65].

2.2.1 Analytical solution

An x-ray beam impinging onto a FC waveguide partly propagates through the guiding core of thickness d by total internal reflection if $n_1 > n_2$ (guided modes). The remaining part of the incoming beam is attenuated in the cladding (radiative modes). Here, we consider propagation of the waveguide modes, in particular transverse electric (TE) modes, in z -direction. Assuming an refractive index profile independent of z , the z dependance of the mode fields can be written as $\exp(-i\beta z)$. The one-dimensional reduced wave equation for $\psi(x)$ then reads [66]

$$\frac{\partial^2 \psi(x)}{\partial x^2} + (n^2 k^2 - \beta^2) \psi(x) = 0. \quad (2.1)$$

The propagation constant β is referred to the projection k_z in z -direction of the wave-vector k in the corresponding medium. Note that within the above description the y coordinate is left out as the refractive index and the electric fields are considered to be independent of y .

The solutions of the wave equation (2.1) satisfying the boundary conditions (i) $\psi(x)$ is continuous at the dielectric interfaces $x = 0$ and $x = -d$ and (ii) vanish at $x = \pm\infty$ are given by

$$\psi(x) = \begin{cases} A \exp(-\gamma x), & \text{for } x \geq 0 \\ A \cos(\kappa x) + B \sin(\kappa x), & \text{for } 0 \geq x \geq -d \\ [A \cos(\kappa d) - B \sin(\kappa d)] \exp[\gamma(x + d)], & \text{for } x \leq -d \end{cases} \quad (2.2)$$

where A and B are constants, $\kappa = (k^2 n_1^2 - \beta^2)^{1/2}$ and $\gamma = (\beta^2 - k^2 n_2^2)^{1/2}$. Applying the boundary condition of $\partial\psi(x)/\partial x$ being continuous at the interfaces, we obtain the following system of equations

$$\gamma A + \kappa B = 0 \quad (2.3)$$

$$[\kappa \sin(\kappa x) - \gamma \cos(\kappa d)] A + [\kappa \cos(\kappa d) + \gamma \sin(\kappa x)] B = 0. \quad (2.4)$$

The eigenvalue equation of this homogeneous equation system is given by

$$\gamma [\kappa \sin(\kappa x) - \gamma \cos(\kappa d)] + \kappa [\kappa \cos(\kappa d) + \gamma \sin(\kappa x)] = 0, \quad (2.5)$$

which can also be written in the form [66]

$$\tan(\kappa d) = \frac{2\kappa\gamma}{\kappa^2 - \gamma^2}. \quad (2.6)$$

The intersection points of the functions $\tan(\kappa d)$ and $F(\kappa d) = 2\kappa\gamma/(\kappa^2 - \gamma^2)$ determine the discrete solutions corresponding to the guided modes denoted as $\psi_m(x)$ in the following. The number of guided modes can be calculated by

$$N = \left[\frac{V}{\pi} \right]_{\text{int}}, \quad (2.7)$$

where $[\]_{\text{int}}$ indicates the term is rounded up to the next integer and V denotes the waveguide parameter

$$V := \sqrt{(n_1^2 - n_2^2)k}d. \quad (2.8)$$

Hence, the characteristic properties of the planar waveguide at a given x-ray energy depend on the guiding and cladding materials employed and the thickness of the guiding layer. The graphical solution of the transcendental equation (2.6) as well as the eigen functions of a waveguide supporting 3 guided modes are shown in Fig 2.3.

The electromagnetic field inside the waveguide can be expressed by a superposition of guided modes ψ_m [67]

$$\psi(x, z) = \sum_{m=0}^{N-1} c_m \psi_m(x) \exp(-i\beta_m z), \quad (2.9)$$

sufficiently far away from the waveguide entrance (no contribution of the radiative modes). The amplitude c_m is determined by the overlap integral of the mode $\psi_m(x)$ with the incident electromagnetic field $\psi_{in}(x)$ [64]

$$c_m = \int_{-\infty}^{\infty} \psi_{in}(x) \psi_m(x) dx. \quad (2.10)$$

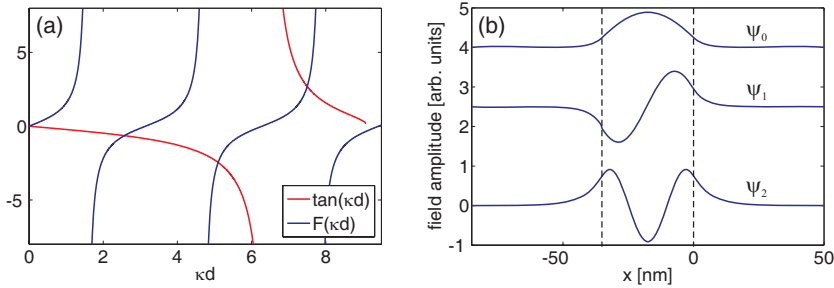


Figure 2.3: (a) The number of intersection points of $\tan(\kappa d)$ and $F(\kappa d)$ for a planar waveguide with $n_1 = 1 - 1.5 \cdot 10^{-6}$, $n_2 = 1 - 5.8 \cdot 10^{-6}$ and $d = 35$ nm indicates 3-mode propagation ($V = 9.1$) for a photon energy $E = 17.5$ keV. (b) Calculated amplitudes of the corresponding eigen functions ψ_0 , ψ_1 and ψ_2 .

We consider the absorption of the electromagnetic wave at the guiding layer/cladding interface by expanding the right-hand side of Eq. (2.9) by a term $\exp(-\mu_m x/2)$ [68]

$$\psi(x, z) = \sum_{m=0}^{N-1} c_m \psi_m(x) \exp[-(i\beta_m + \mu_m/2)z], \quad (2.11)$$

where the effective linear absorption coefficient μ_m is weighted with respect to the intensity distribution of the m th mode

$$\mu_m = \frac{1}{\|\psi_m\|^2} \int_{-\infty}^{\infty} |\psi_m(x)|^2 \mu(x) dx. \quad (2.12)$$

The exact solutions for the electromagnetic field along z inside planar waveguides, taking into account absorption, can be calculated but is comparably time consuming.

2.2.2 Numerical method

The fact that (i) materials have a refractive index close to 1 and (ii) the propagation of modes takes place in the paraxial approximation enables the use of an approximated wave equation. The second argument is related to the critical angle of total reflection θ_c [27]

$$\theta_c \approx \sqrt{2(\delta_2 - \delta_1)}. \quad (2.13)$$

Eq. (2.13) is an expansion of Snell's law

$$n_1 \cos(\theta_i) = n_2 \cos(\theta_r), \quad (2.14)$$

for $\theta_i = \theta_c$ and $\theta_r = 0$. Here, θ_i is the grazing angle of a incident beam propagating in a medium with a refractive index n_1 and θ_r the grazing angle of a refracted beam in a medium with n_2 . As $\delta_2 - \delta_1$ is on the order of 10^{-5} , the k -vector of wave propagating inside the guiding core of the waveguide makes an angle of less than 0.3° . Substitution of the paraxial Ansatz (see also section 1.1.3)

$$\psi(x, y, z) = u(x, y, z) \exp(-ikz) \quad (2.15)$$

into the Helmholtz equation (1.23), which amounts of taking out the fast oscillating term $\exp(-ikz)$, and neglecting the small term $\partial^2 u(x, y, z)/\partial z^2$ yields

$$\left(2ik \frac{\partial}{\partial z} + \nabla_{\perp}^2 + [n^2(x, y, z) - 1]k^2 \right) u(x, y, z) = 0. \quad (2.16)$$

This inhomogeneous paraxial wave equation is called parabolic wave equation (PWE). The PWE was adopted by Leontovich and Fock for radio wave propagation and later on adapted for studying diffraction inside x-ray optics like FZPs and waveguides [69, 70, 60]. Note, that the form of Eq. (2.16) has already been introduced in section 1.2.2 for the scattering of a plane wave on a medium in the projection approximation. Further analogy to x-ray propagation imaging presented in the previous chapter concerns $\psi(x, y, z)$ in Eq. (2.15) which describes the propagation of a plane wave in free-space through the factor $\exp(-ikz)$ and the modulation of the wave-field by the waveguide medium through $u(x, y, z)$.

A numerical implementation of the PWE for waveguide propagation was realized by Christian Fuhse using the finite-difference (FD) method based on the Crank-Nichelson scheme [19, 68, 71, 72]. In case of the slab waveguide design, neglecting the y-dependance, the PWE yields

$$\frac{\partial u(x, z)}{\partial z} = C \frac{\partial^2 u(x, z)}{\partial x^2} + D(x, z)u(x, z), \quad (2.17)$$

with

$$C := -\frac{i}{2k} \quad \text{and} \quad D := -\frac{ik}{2} [n^2(x, z) - 1]. \quad (2.18)$$

The finite-difference method approximates the solutions to PWE by replacing derivative expressions in Eq. (2.17) with approximately equivalent difference

quotients. In case of the Crank-Nichelson scheme, it is second order accurate in Δx and Δz :

$$\begin{aligned} \frac{u_i^{n+1} - u_i^n}{\Delta z} &= \frac{C}{2(\Delta x)^2} [(u_{i-1}^n - 2u_i^n + u_{i+1}^n) + (u_{i-1}^{n+1} - 2u_i^{n+1} + u_{i+1}^{n+1})] \\ &\quad + \frac{D_i^{n+\frac{1}{2}}}{2}(u_i^n + u_i^{n+1}), \end{aligned} \quad (2.19)$$

with $u_i^n := u(x_i, z_n)$ and $D_i^{n+\frac{1}{2}} := D(x_i, z_{n+\frac{1}{2}})$. The area fulfilling the PWE is divided into a finite number of grid points equidistantly spaced by Δx and Δz of a grid $(M_x + 1) \times (2M_z + 1)$ with

$$x_i := i \Delta x, \quad i = 0, 1, 2, \dots, M_x, \quad (2.20)$$

$$z_n := n \Delta z, \quad n = 0, \frac{1}{2}, 1, \frac{3}{2}, 2, \dots, M_z, \quad (2.21)$$

as illustrated in Fig. 2.4 (a). The boundary conditions

$$u(x, 0) = u_0(x, 0), \quad u(x_0, z) = u_0(x_0, z) \text{ and } u(x_{M_x}, z) = u_0(x_{M_x}, z) \quad (2.22)$$

allow for the determination of u_i^{n+1} from u_i^n . The $u_0(x, z)$ are described by an incident plane wave or a damped wave propagating in the cladding, respectively. In fact, we assume that the wave-field is not significantly disturbed by the guided wave-field far away from the guiding core. For a more detailed explanation of the numerical implementation along with the source code we refer to the thesis of Christian Fuhse [19].

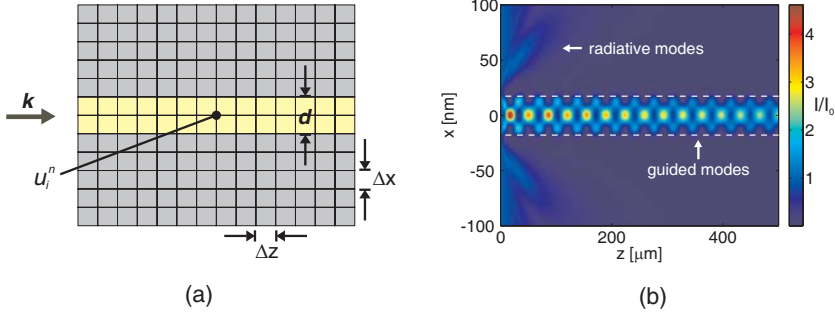


Figure 2.4: (a) The FD calculation of the electromagnetic field u_i^n uses a grid equidistantly spaced by Δx and Δz . The incident field is assumed to be a plane wave impinging normal to the front face. (b) FD calculation inside a waveguide with a 35 nm thick C guiding layer surrounded by a Mo cladding for $E = 17.5$ keV showing 2-mode propagation.

FD simulation of a Mo/C[$d = 35$ nm]/Mo waveguide with a waveguide parameter $V = 9.1$ for a photon energy $E = 17.5$ keV is shown in Fig. 2.4 (b) illustrating 2-mode propagation. Note that based on symmetry considerations a normal incidence plane wave only excites even modes. In fact, even modes are symmetric while odd modes are antisymmetric and the overlap integral (2.10) thus vanishes for all odd modes.

2.3 Transmission and coherence

The beam shape, the coherence and the transmission T (transmitted intensity) strongly depend on the waveguide core diameter d and the waveguide length l [20]. Large slits and pinholes with $d \gg l$ can be considered as apertures in a fully absorbing frame. In contrast, the wave-field behind a device of higher aspect ratio (l/d) is not only determined by a stepwise constant transmission function (diffraction aperture function) where the intensity behind the frame is practically zero and the field behind the aperture is merely altered by a phase shift. The propagation of the wave-field through the optic is rather affected by volume diffraction and interference effects for $d \leq d_c = l \tan(\theta_c) \approx l\theta_c$ [73]. With decreasing d , waveguide modes are excited and for small d the propagation changes from multi-modal to mono-modal waveguiding as shown in Fig. 2.5.

To avoid contributions of radiative modes in the exit wave-field, the length of the waveguide l must be long enough, i.e. the transmission of the cladding T_{cl} for a given energy E and diameter d must be correspondingly small. Inherently, this task becomes more difficult with decreasing d . Further, the absorption in the cladding decreases with increasing E . In order to take the effect of d into account, the differential transmission $\sigma := T/T_{cl}$ of the guiding layer to the cladding is considered. Especially at high energies, x-ray waveguides need very large aspect ratios l/d with $l/d \approx 10^5$ being a typical value, which on the other hand is accompanied by small transmission T [16].

We define the transmission T of a waveguide as the ratio of the intensity $I_{in} = |\psi_{in}|^2$ impinging onto the waveguide and the intensity $I = \int |\psi|^2 dx$ exiting the waveguide

$$T = \frac{I}{I_{in}} \frac{d_{in}}{d}, \quad (2.23)$$

normalized by the size d_{in} of the incident beam at the waveguide entrance and the guiding core diameter d . In case of the FD simulation, the transmission is calculated for $d_{in} = d$. Multi-modal waveguides have an improved efficiency at a given d_{in} compared to the mono-modal waveguides due to the larger d since the field intensity parts in the cladding of the excited modes for multi-modal propagation is smaller than for mono-modal propagation as shown in Fig. 2.6.

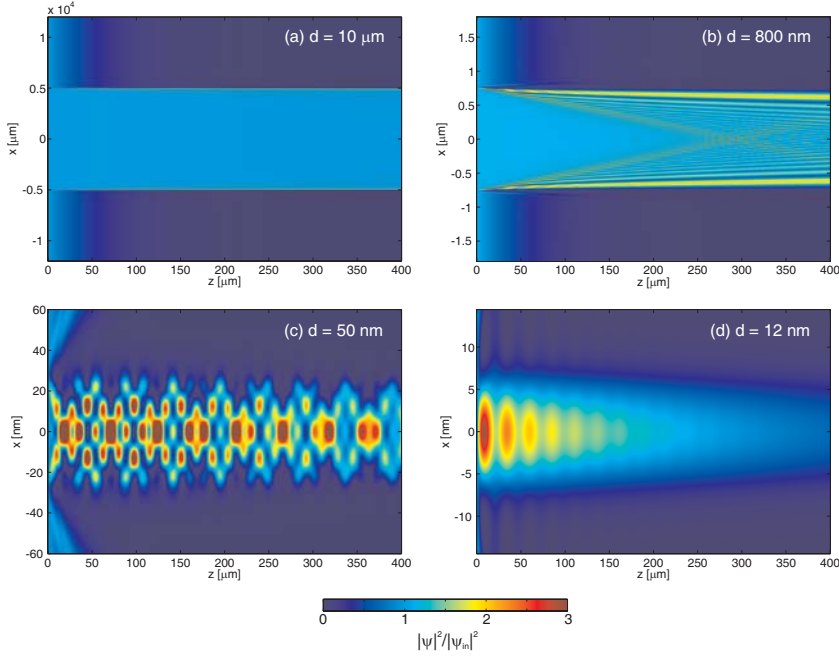


Figure 2.5: Electromagnetic field intensities in a C guiding core surrounded by a Mo cladding at $E = 17.5$ keV. At large d , differences from a plane wave are only visible near the interfaces (a). When d/l falls below θ_c , waves are reflected back into C showing guided wave contributions (b). Further decreasing of d leads to typical interference pattern of multi-mode (c) and mono-modal (d) waveguides.

The beam exiting a mono-modal or multi-modal waveguide is fully coherent if the incident wave-field is a plane wave (independent of the angle of incidence). The deviation of an incident synchrotron beam to an idealized plane wave can be discussed by the concept of coherence lengths. The longitudinal coherence length L_L is given by [27]

$$L_L = \frac{1}{2} \frac{\lambda^2}{\Delta\lambda} \quad (2.24)$$

for partially coherent beams. Typically, monochromators at synchrotron beamline setups have an energy resolution of $\Delta E/E \approx 10^{-4}$ corresponding to $L_L \approx 0.5 \mu\text{m}$ for x-rays with a wavelength of 0.1 nm. The most important parameter to

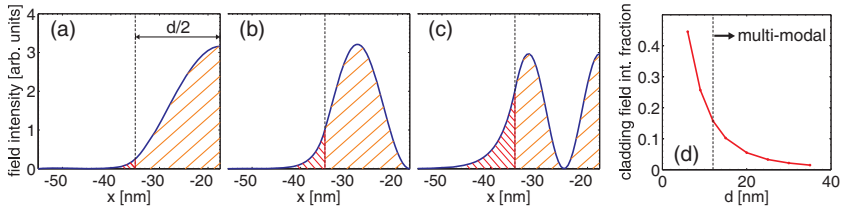


Figure 2.6: (a)-(c) The field intensity parts in the cladding are 0.02, 0.07 and 0.19 for the ψ_0 , ψ_1 and ψ_2 mode, respectively. We used $n_1 = 1 - 1.5 \cdot 10^{-6}$, $n_2 = 1 - 5.8 \cdot 10^{-6}$, $d = 35$ nm and $E = 17.5$ keV for the calculations. (d) The cladding field intensity part strongly decreases at larger guiding core diameter d as shown for the ψ_0 mode. The propagation is mono-modal for $d \leq 12$ nm.

explain the spatial coherence of the incident beam is the transverse coherence length. The transverse coherence length L_T can be calculated by⁷

$$L_T = \frac{\lambda R}{2 D}, \quad (2.25)$$

where D is the synchrotron source extension and R the distance source - waveguide entrance.

A lower degree of longitudinal coherence increases the photon flux exiting the waveguide but might affect the resolution in waveguide-based imaging applications as discussed in chapter 5. In contrast, a lower degree of transverse coherence decreases the transmission since the waveguide essentially accepts only the coherent flux. A more detailed explanation of the transverse coherence effect is given in chapter 4 for the different experimental setups. In summary, the waveguide acts as a spatial filter but does not improve the energy resolution.

2.3.1 Mono-modal waveguides

A planar waveguide supports only the fundamental mode if d is smaller than the critical width W corresponding to the limit of the waveguide parameter $V = \pi$. The critical width is given by [60]

$$W = \frac{\lambda}{2\sqrt{(n_1^2 - n_2^2)}} \approx \frac{\lambda}{2\sqrt{2(\delta_2 - \delta_1)}}. \quad (2.26)$$

⁷Assuming (i) the source is incoherent and (ii) there are no optical elements on the optical path between the source and the waveguide.

Accordingly, the wave-field of a mono-modal waveguide yields

$$\psi(x, y) = c_0 \psi_0(z) \exp [(-i\beta_0 - \mu_0/2)z], \quad (2.27)$$

sufficiently far away from the waveguide entrance. The transmission as a function of the waveguide length l is given by [19]

$$T(l) = \frac{\int |c_0 \psi_0(x) \exp [(-i\beta_0 - \mu_0/2)l]|^2 dz}{\int_{-d}^0 |\psi_{in}|^2 dz}. \quad (2.28)$$

Eq. (2.28) can be simplified (i) assuming plane wave illumination $\psi_{in} = 1$ and (ii) determining numerically the propagation constant β_0 as well as the constants κ_0 and γ_0 . Solving the transcendental eigenvalue equation (2.6), we obtain $\beta_0 W \approx 1.064 \cdot 10^3$ which we used to calculate $\kappa_0 W \approx 1.868$ and $\gamma_0 W \approx 2.526$. We determine $|c_0|^2 \approx 1.979W$ and the transmission for $d = W$ yields

$$T(l) = \frac{|c_0|^2 \exp(-\mu_0 l)}{d} \approx 1.979 \exp(-\mu_0 l), \quad (2.29)$$

where μ_0 is the effective linear attenuation coefficient of the fundamental mode. The length of the waveguide as a function of the differential transmission $\sigma = T/T_{cl}$ can be expressed by [19]

$$l(\sigma) = \frac{\ln(\sigma) - \ln(|c_0|^2/d)}{\mu_{cl} - \mu_0}, \quad (2.30)$$

where μ_{cl} denotes the linear attenuation coefficient of the cladding. The transmission as a function of σ yields

$$T(\sigma) = (|c_0|^2/d)^{1/(1-\mu_0/\mu_{cl})} \sigma^{-(\mu_0/\mu_{cl})/(1-\mu_0/\mu_{cl})}. \quad (2.31)$$

The transmission reaches a maximum for a given σ if μ_0/μ_{cl} is minimal which requires a vacuum guiding layer. Then we find $\mu_0/\mu_{cl} \approx 0.156$ and $T_{vac}(\sigma) \approx 2.246\sigma^{-0.185}$. Note that the presented derivation and calculation is applied within simplified assumptions. Nevertheless, taking into account that the differential transmission σ depends on the experimental setting and requirements, it allows for an estimation of possible waveguide transmission T .

2.3.2 Optimized cladding design

So far, x-ray waveguides essentially consist of one cladding material and one guiding core material. Thus, the transmission T is optimized by choosing low density guiding core materials. We present a novel waveguide design based on an appropriate interlayer between the cladding and the guiding core, relaxing

the requirements for the waveguide length l [20]. Thereby, the absorption of the evanescent tails of the guided modes is significantly reduced, while a second (outer) cladding with a high absorption coefficient is used to efficiently block the radiative modes.

In fiber optics, index profiles have long been used to optimize the propagation properties of visible light, in particular, to reduce dispersion effects [74]. The present design represents a first step towards optimized radiation transport and mode filtering of x-rays by waveguiding in generalized index profiles. The refractive index profile of the two-component Ge/Mo/C/Mo/Ge waveguide is shown in Fig. 2.7, simulated for the photon energy range $E = 12 - 18$ keV and for the optical constants corresponding to ideal (bulk) electron densities [75].

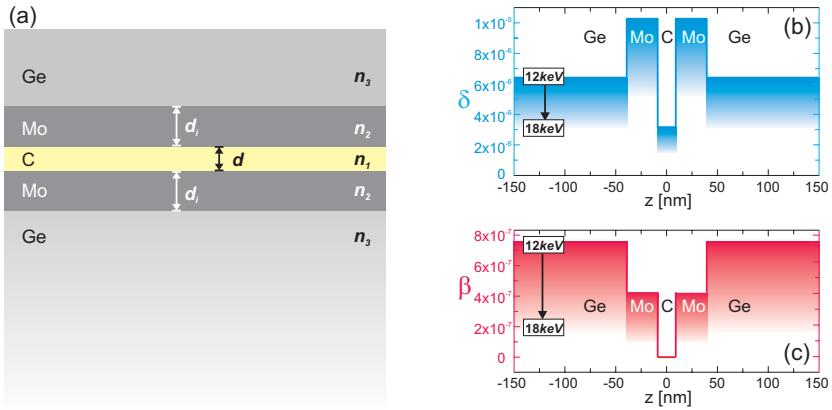


Figure 2.7: (a) Schematic of the two-component waveguide. The profiles of (b) the dispersive δ and (c) the imaginary β parts of the refractive index $n = 1 - \delta + i\beta$, calculated for $E = 12 - 18$ keV.

At 18 keV, the C guiding layer embedded in the high $\delta_{\text{Mo}} = 5.5 \cdot 10^{-6}$ Mo cladding forms a relatively deep potential well. At the same time, a relatively low $\beta_{\text{Mo}} = 9.1 \cdot 10^{-8}$ value of Mo reduces the absorption in the (interlayer) cladding and hence enables an increased transmission T . The thickness $d_i = 30$ nm of the Mo cladding is thin enough so that beam parts of the interlayer do not significantly reduce the absorption of the primary beam. On the other hand, the comparably high $\beta_{\text{Ge}} = 1.7 \cdot 10^{-7}$ enables short waveguide length l of sub-500 μm . Note that, at this energy, the low electron density layer with $\beta_{\text{C}} = 3.5 \cdot 10^{-10}$ contributes less than 2% to the effective absorption $\mu_{\text{eff}} = \mu_m$. In other words C "acts" essentially like a vacuum guiding layer.

The same δ and β characteristics hold for the whole x-ray energy range 12 – 18 keV but is less pronounced at lower energies. In fact, away from absorption edges, the ratio δ/β increases with decreasing wavelength λ . This effect is more pronounced at lower electron densities ρ . For a given layer system at an appropriate energy range, the efficiency of a waveguide is more easily enhanced at higher energies due to the lower β values. Nevertheless, the profiles of δ and β remain their characteristics over several keV so that the waveguiding property remains.

The choice of a favourable outer/inner cladding characteristic depends on the respective absorption edges. The material of the outer cladding should ideally have the absorption edge just below the chosen energy range as the absorption is specifically high at these energies. In contrast, the interlayer material should have the absorption edge just above the chosen energy range to reduce the absorption at the interface guiding layer/cladding. The electron density ρ of the interlayer is usually higher than for the outer cladding leading to an enhanced δ , i.e., ensuring the guided modes to be trapped in a deeper potential well.

Let us now consider the transmission of a planar waveguide with and without an interlayer. More general waveguide design schemes including the two-component cladding need to be treated by FD simulations. The calculations in Fig. 2.8 (a) and (b) are carried out for $l = 400 \mu\text{m}$, $d = 12 \text{ nm}$ and $E = 17.5 \text{ keV}$.

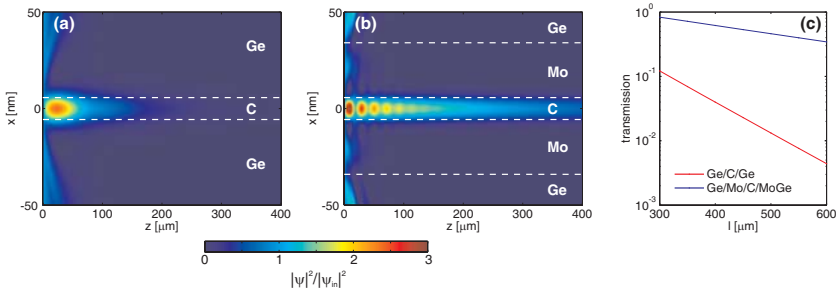


Figure 2.8: (a) and (b) Transmission of a mono-modal waveguide ($d = 12 \text{ nm}$) is strongly enhanced by the presence of Mo interlayer with $d_i = 30 \text{ nm}$. (c) Calculated transmission T as a function of the waveguide length l exhibiting the flux gain of more than a factor 6 even at very short l .

The absorption losses at the interface guiding layer/cladding are strongly reduced by the presence of the Mo interlayer. The transmission $T = 0.618$ of the Ge/Mo/C/Mo/Ge waveguide is more than a factor 15 higher than for the

Ge/C/Ge layer system with $T = 0.040$. The transmission differences are even more favourable at longer waveguide length l as shown in Fig. 2.8 (c).

For many other x-ray energies favourable material combinations can be found. Due to the absorption edge of *Mo* at $E = 20.0$ keV, the efficiency of the Ge/*Mo*/C/*Mo*/Ge waveguide is reduced for x-ray energies of $E \approx 8$ keV. This energy range is quite interesting for biological imaging as the interaction of low electron density elements like C with x-rays is stronger. A more adequate interlayer material is Ni (absorption edge 8.3 keV) and NiO which can easily be deposited on Ge using sputtering techniques as well (see section 3.2).

An optimized waveguide design at an energy range of 6–8 keV is Cr/Ni/Be/Ni/Cr. The absorption of $\beta_{\text{Be}} = 7.4 \cdot 10^{-9}$ ($E = 8$ keV) is lower than $\beta_{\text{C}} = 1.2 \cdot 10^{-8}$. Further, Cr with $\beta_{\text{Cr}} = 2.2 \cdot 10^{-6}$ enables shorter waveguide length l than Ge with $\beta_{\text{Ge}} = 4.4 \cdot 10^{-7}$ ⁸. The comparison of the above mentioned layer system waveguides is shown in Fig. 2.9 for a guiding layer thickness $d = 18$ nm and an interlayer thickness $d_i = 30$ nm.

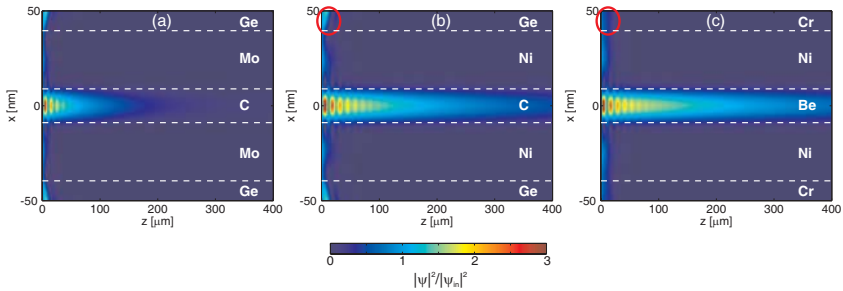


Figure 2.9: At $E = 8$ keV, the transmission increases from $T = 0.040$ of a *Mo* interlayer waveguide (a) to $T = 0.412$ of a *Ni* interlayer system (b), and by choosing a *Be* guiding layer yielding $T = 0.542$ (c). A *Cr* outer cladding enhances the absorption of the radiative modes compared to *Ge* (see red circles for the radiative modes).

The fabrication of multilayer slices with the required dimensions is possible as shown in chapter 3.

⁸Note that Ge has an absorption edge at 11.3 keV. Therefore, Ge is not suitable as an outer cladding material just below 11 keV. Nevertheless, the absorption β_{Ge} is sufficient at $E = 8$ keV taking into account that at lower energies shorter waveguide length are needed due to higher β_{C} .

2.4 Exit wave-field propagation

Due to the filtering properties, the waveguide acts as a secondary source. Thus, the wave-field at the exit of the waveguide determines the quality of the object reconstruction in waveguide-based microscopy. The resolution in holographic imaging is directly related to the beam size of the exit wave-field. Small cross-section at the waveguide exit face leads to an increased divergence of the waveguide beam. Therefore, it is important to know the shape of the waveguide exit wave-field.

The exit wave-field can be simulated using the FD method. Knowing the exit wave-field, the wave-field might be propagated over a distance $z_2 - z_1$ either using FD calculations or free-space propagation as introduced in the first chapter. In case of propagation distances up to several tens of micrometer, the free-space propagator (or the Fresnel propagator) has to be applied. As an example, assuming a beam size of $d = 35$ nm, the Fresnel number Eq. (1.20) yields $N_F = d^2 / \lambda(z_2 - z_1) = 0.64$ for a photon energy $E = 17.5$ keV and a propagation distance $z_2 - z_1 = 50$ μm . Propagation distances of several hundreds of micrometer results in $N_F \ll 1$ and the Fraunhofer approximation can be used.

Fig. 2.10 (a) shows the electromagnetic field intensity inside the Ge/Mo/C/Mo/Ge waveguide as well as the intensity exiting the waveguide and further propagating in vacuum. As expected for a quasi-point source, the waveguide beam in free-space diverges. Fig. 2.10 (b) shows the line scan of the electromagnetic field intensity in Fig. 2.10 (a) at the exit face of the waveguide (distance z_1 , red dashed line) and at a distance $z_2 = 90$ μm (blue dashed line) behind the exit face of the waveguide. To compare the FD simulation to Fresnel simulations (FS), we have applied the free-space propagator to propagate the FD field at z_1 through z_2 (black dashed line in Fig. 2.10 (b)). The FD simulation and the FS simulation are in good agreement. For longer propagation distance z_3 , 190 μm behind z_1 , we have used the Fraunhofer formalism which consists of applying the fast Fourier transform (FFT) on the FD field at z_1 . Fig. 2.10 (d) shows the the field intensity propagated to z_3 using the FD simulation (blue dashed line) and the FFT (black dashed line). Again, the shape of the curves are in good agreement. Starting propagation using Fresnel or Fraunhofer calculations from FD fields at z with $z_1 < z < z_2$, the FS and the FFT propagated fields are not in agreement with the FD propagated field, respectively (not shown in Fig. 2.10). Fig. 2.10 (c) shows the phase distribution of the electromagnetic field inside the Ge/Mo/C/Mo/Ge waveguide as well as the phase distribution of the exiting field propagating in vacuum. Around the propagation distance z_1 (indicated by a black arrow), the tails of the phase distribution along the x -direction is slowly varying. For larger propagation distances $z > z_1$ some pronounced edge effects are visible in the tails of the phase distribution. We assume that these edge

effects causes the propagation of the Fresnel and Fraunhofer calculated fields to fail.

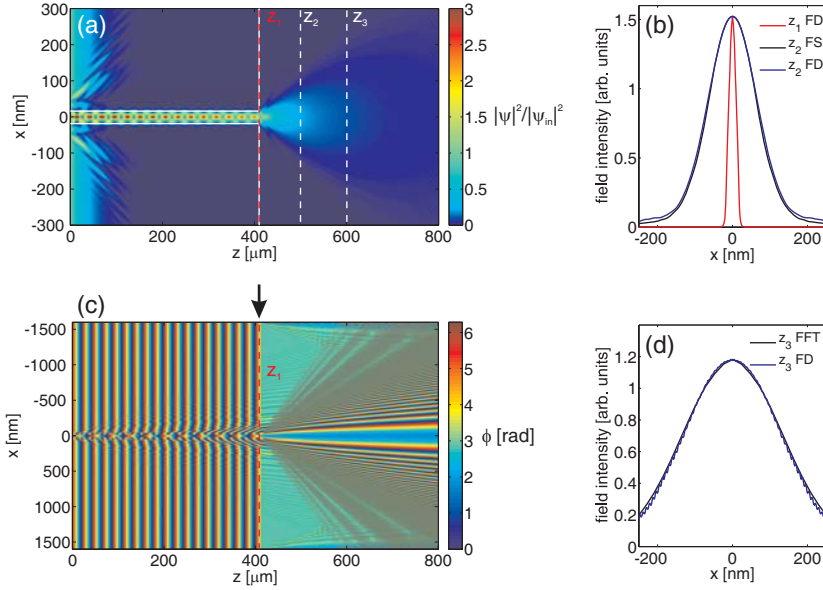


Figure 2.10: (a) Electromagnetic field intensity of the Ge/Mo/C/Mo/Ge for $d = 35$ nm and $E = 17.5$ keV using FD simulation. The dashed lines indicate the guiding core dimension and the exit face of the waveguide. The dotted lines indicate the propagation distance $z_2 = 90$ μm (white) and $z_3 = 200$ μm (white) from the waveguide exit face z_1 (red). (b) Line scans of the propagated intensity (FD simulation) shown in (a) at z_1 (indicated by a red dashed line) and z_2 (indicated by a blue dashed line). The black dashed line indicates the propagation of the FD simulated field at z_1 to z_2 using free-space propagation (FS). (c) Phase distribution calculated using FD simulation. The black arrow indicated the region around $z = z_1$. (d) Line scan of the FD simulation at a distance z_3 indicated by a blue dashed line. The black dashed line indicates the propagation of the FD simulated field at z_1 to z_3 using the fast Fourier transform (FFT).

2.4.1 Waveguide near-field

First, we compare the waveguide near-field of the optimized Ge/Mo/C/Mo/Ge with the Ge/C/Ge layer system shown in Fig. 2.11. The former system does not

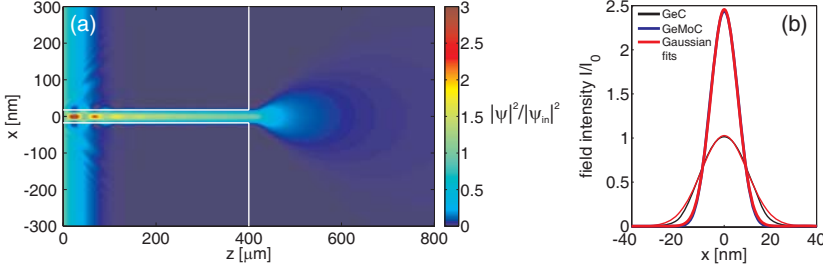


Figure 2.11: (a) Electromagnetic field intensity of the Ge/C/Ge for $d = 35$ nm and $E = 17.5$ keV using FD simulation. (b) Near-field distributions along with Gaussian fits of the waveguide with and without Mo interlayer.

only offer a significantly higher transmission but also a smaller near-field distribution in case of the waveguide length $l = 400$ μm considered here. Gaussian fits to the exit wave-fields yields $\Delta_x = 23.5$ nm for the Ge/C/Ge waveguide compared to $\Delta_x = 13.6$ nm for the optimized waveguide. The higher absorption at the C/Ge interface leads to a damping out of the second mode and, after a propagation length of $l = 300$ μm , the fundamental mode is the only remaining mode.

We now consider the near-field intensities of the two-component waveguides with different layer materials and different guiding layer thicknesses d . The near-field distributions of the Ge/Mo/C/Mo/Ge waveguide with $d = 18$ nm and $d = 9$ nm, respectively, are shown in Fig. 2.12 (a) and (b). For a photon energy $E = 17.5$ keV and a waveguide length $l = 600$ μm , the beam size $\Delta_x = 12.9$ nm is significantly smaller than the guiding layer thickness $d = 18$ nm. In contrast, $\Delta_x = 8.8$ nm is close to $d = 9$ nm. This effect is due to the higher ratio cladding/guiding core intensity part as shown in Fig. 2.6. In fact, for very small guiding core dimensions, the width of the guided modes becomes significantly larger than the guiding core diameter due to the evanescent wave in the cladding [60].

Bergemann et al. [60] pointed out that the task of focusing an x-ray beam is equivalent to that of confining a quantum wave function inside a potential well of height U_0 . Comparing the parabolic wave equation (2.16) for $u = u(x, z)$ and approximated by $n^2 \approx 1 - 2\delta$

$$-\frac{i}{k} \frac{\partial u}{\partial z} = \frac{1}{2k^2} \frac{\partial^2 u}{\partial x^2} - \delta u \quad (2.32)$$

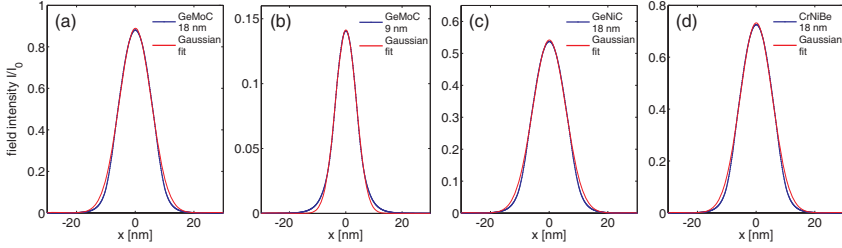


Figure 2.12: Near-field distributions along with Gaussian fits of different waveguide systems simulated for a photon energy $E = 17.5$ keV (a) and (b) as well as for $E = 8$ keV (c) and (d). Lowest FWHM is obtained for the smallest guiding layer thickness $d = 9$ nm (b).

to the time-dependent Schrödinger equation describing a particle of mass m in a potential $U(x)$ [76]

$$-i\hbar \frac{\partial \psi}{\partial t} = \frac{\hbar^2}{2m} \frac{\partial^2 \psi}{\partial x^2} - U\psi, \quad (2.33)$$

where \hbar denotes the Planck constant, one recognizes $t \equiv z$, $\hbar \equiv k^{-1}$, $m = 1$, and $U \equiv \delta$. In analogy to the guided modes in a slab waveguide we consider bound states of a potential well [76]

$$U(x) = -U_0 \Theta(a/2 - |x|), \quad (2.34)$$

where Θ denotes the step function and a the width of the potential well. The energies of a bound state are in the interval $-U_0 \leq E \leq 0$. For a given guiding core diameter d , theoretically highest confinement of x-rays in a slab waveguide is obtained for $\delta \rightarrow \infty$. In ‘quantum analogy’, the wave functions in an infinitely deep potential well $U_0 \rightarrow \infty$ are given by [76]

$$\phi_n(x) = \sqrt{\frac{2}{a}} \sin\left(\frac{n\hbar x}{a}\right), \quad (2.35)$$

where n denotes the quantum number. Considering only the fundamental state $n = 1$ inside the potential well the wave function yields

$$\phi(x) = \sqrt{\frac{2}{a}} \sin\left(\frac{\hbar x}{a}\right). \quad (2.36)$$

Correspondingly, we consider the limiting case $d = W$ of a waveguide supporting only the fundamental mode. The particle position uncertainty Δx of the bound state then yields

$$\Delta x = \sqrt{\langle x^2 \rangle - \langle x \rangle^2}, \quad (2.37)$$

with the expectation values $\langle x \rangle$ and $\langle x^2 \rangle$ given by

$$\langle x \rangle = \int_{-a/2}^{a/2} |\phi(x)|^2 x dx, \quad (2.38)$$

and

$$\langle x^2 \rangle = \int_{-a/2}^{a/2} |\phi(x)|^2 x^2 dx. \quad (2.39)$$

Note that, in case of an infinitely deep potential well Δx is smaller than for finite potential wells as the wave function is only confined in the interval $[-a/2, a/2]$. Evaluating Eq. (2.37) using Eq. (2.36), we obtain a criterion for the universal lower limit of the beam size given by

$$\Delta x = 0.18a = 0.18W. \quad (2.40)$$

The position uncertainty Δx is the root of the variance $(\Delta x)^2 = \langle x^2 \rangle - \langle x \rangle^2$ of the presence probability density $|\psi(x)|^2$ of the bound state. The bound state $\phi(x)$ is of the same shape as the guided mode inside the waveguide. Accordingly, the presence probability density of the bound state is directly comparable to the near-field intensity distribution at the waveguide exit. The near-field intensity distribution of waveguides with $d \simeq W$ can be approximated by a Gaussian function

$$f(x) = A \exp \left[-\frac{(x - x_0)^2}{2\sigma^2} \right], \quad (2.41)$$

where σ^2 is the variance. We might therefore identify Δx with σ . The considered beam sizes of the near-field distribution are given by the full width at half maximum $\text{FWHM} = 2\sqrt{2\ln 2}\sigma$ as obtained by Gaussian fits (see Fig. 2.12). Accordingly, the lower limit presented in Eq. (2.40) corresponds to a minimal focusing of $0.42W$ in terms of FWHM of the near-field distribution.

Numerical calculations of the electromagnetic field intensity inside the waveguide show that an ideally minimal focusing of $0.42W$ can not be reached. In fact, the exponentially decaying wave-field outside the guiding core diverges for $d \rightarrow 0$ causing the near-field width to increase again for a certain value $d < W$. The minimal near-field width of a Ge/Mo/C/Mo/Ge waveguide (critical width $W = 12$ nm) simulated for $l = 600$ μm and $E = 17.5$ keV is $\Delta_x = 7.7$ nm ($0.64W$) at $d = 5.3$ nm ($0.44W$). Fig. 2.13 shows the simulated near-field width Δ_x as a function of the guiding layer thickness d .

The FWHM of the near-field distribution of the Ge/Ni/C [$d = 18$ nm]/Ni/Ge and the Cr/Ni/Be [$d = 18$ nm]/Ni/Cr waveguide are of the same order of magnitude ($l = 300$ μm , $E = 8$ keV). Due to more favourable refractive index difference $n_2 - n_1$, $\Delta_x = 13.0$ nm of the later waveguide is smaller than $\Delta_x = 13.3$ nm of the former waveguide as shown in Fig. 2.12 (c) and (d).

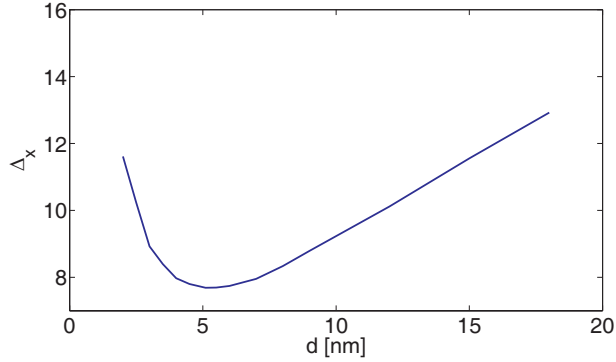


Figure 2.13: FWHM Δ_x of the near-field distribution as a function of the guiding layer thickness d , simulated for a Ge/Mo/C/Mo/Ge waveguide with $l = 600 \mu\text{m}$ and $E = 17.5 \text{ keV}$. For $d = 5.3 \text{ nm}$, highest beam confinement with $\Delta_x = 7.7 \text{ nm}$ is expected.

2.4.2 Waveguide far-field

So far, it is not possible to measure the waveguide near-field directly. The spatial resolution of the measurable intensity is restricted to the resolution of the detectors nowadays available. Scintillator-based detectors⁹, optimized for high resolution imaging, reach spatial resolution on the order of $\approx 1 \mu\text{m}$ which is, obviously, not sufficient to detect intensity distribution in the nm-range [77]. Therefore, x-ray waveguide properties are measured in the far-field regime taking advantage of the divergence of the waveguide beam.

In the small-angle approximation, the intensity of the Fraunhofer diffraction pattern of a one-dimensionally waveguide is given by [22]

$$I(2\theta) \propto \left| \int \psi(x) \exp(ik2\theta x) dx \right|^2, \quad (2.42)$$

where 2θ is the exit angle of the waveguide beam (see Fig. 2.14). Thus, the far-field intensity represents the square modulus of the Fourier transform of the near-field which is given by the field at the end face of the waveguide.

⁹The detectors consist of a scintillator, a light microscopy optic and a charge-coupled device (CCD). The scintillator converts part of the x-ray absorbed by a material into a visible-light image which is projected onto the CCD by the light optics.

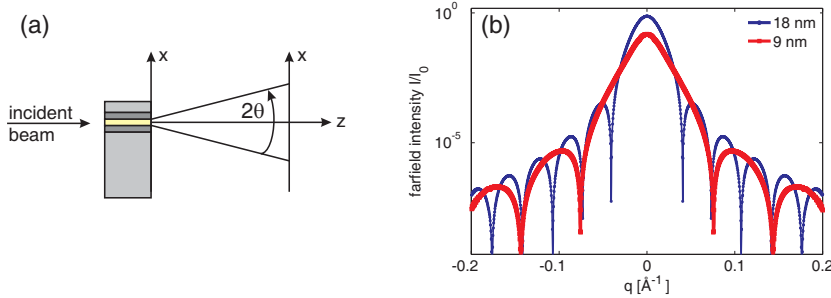


Figure 2.14: (a) The Fraunhofer diffraction pattern of a planar waveguide is a function of the angle 2θ in the (x, z) plane. (b) Far-field intensity as a function of the momentum transfer q . The far-fields of the $d = 18$ nm and $d = 9$ nm waveguides are calculated from the near-field distributions shown in Fig. 2.12 (a) and (b), respectively. The corresponding FD simulations are performed with $\Delta x = 0.1$ nm, $M_x = 16000$, $\Delta z = 100$ nm and $M_z = 1500$.

Instead of using the exit angle 2θ , the far-field might also be displayed in reciprocal space by the momentum transfer q

$$q = \frac{4\pi}{\lambda} \theta, \quad (2.43)$$

dropping the wavelength dependence of the far-field. The divergence of the waveguide beam increases with smaller guiding layer thicknesses as shown in Fig. 2.14 (b). Gaussian fits yield a width $\Delta_q = 0.0227 \text{ \AA}^{-1}$ for $d = 9$ nm and $\Delta_q = 0.0222 \text{ \AA}^{-1}$ for $d = 18$ nm. Compared to the near-field FWHM Δ_x obtained above, the differences in Δ_q are significantly less pronounced. However, reducing d leads to more pronounced tails which enhances the effective numerical aperture, i.e. the covered range in reciprocal space. The oscillation of the tails corresponds to the periodicity $\Delta q = 2\pi/d$ in good approximation but also depend on the exact waveguide length l .

2.4.3 Mode beating effect

A waveguide supporting more than one mode shows a periodically alternating electromagnetic field (mode beating) as shown in Fig. 2.15. Correspondingly, an oscillating confinement of the fields depending on the propagation distance is observed as illustrated by the dashed lines in Fig. 2.15 (a) as well as oscillating near-field profiles as shown in Fig. 2.15 (b). Thus, the exit wave-field will depend on the exact length of the waveguide. The FWHM of the simulated near-field

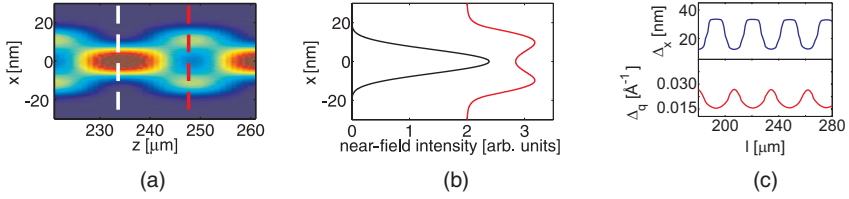


Figure 2.15: (a) Electromagnetic field intensity inside the Ge/Mo/C [$d = 35$ nm]/Mo/Ge waveguide calculated for $E = 17.5$ keV within a range of 221–261 μm in propagation direction z . (b) Field intensities which correspond to the dashed lines in (a) illustrating differences in possible mode structures. (c) FWHM of the simulated near-field distribution (top) and far-field distribution (bottom) as a function of the waveguide length l .

Δ_x and the corresponding far-field intensity Δ_q as a function of the waveguide length l are plotted in Fig. 2.15 (c).

The near-field width is minimal $\Delta_x = 12.6$ nm in the considered waveguide length range of 221 – 261 μm , well below the guiding layer thickness of 35 nm, whereas the maximal width is $\Delta_x = 33.5$ nm. The corresponding FWHM of the far-field intensity are $\Delta_q = 0.0252 \text{ \AA}^{-1}$ and $\Delta_q = 0.0114 \text{ \AA}^{-1}$, respectively. The periodicity of the oscillation is approximately 15 μm .

2.5 Conclusion

The main result of the current chapter is the improved waveguiding property by changing from a 3 layer sequence to a 5 layer sequence waveguide: The improvement is due to the introduction of an additional inner cladding layer adjacent to the guiding layer which reduces the interface attenuation of the guided modes and trap the guided modes in a deep potential wall. The blocking of the radiative modes is achieved by a strongly absorbing outer cladding material.

3 Fabrication of x-ray waveguides

In this chapter we describe the fabrication of multilayer x-ray waveguides. Two-dimensionally confining x-ray waveguides are obtained by combining two multilayer slices in a crossed geometry.

We present the technical concept and fabrication of waveguides with the design as described in section 2.3.2. In particular, the waveguide consist of a Ge/-Mo/C/Mo/Ge optical layer sequence optimized for an x-ray energy range of 12 – 18 keV.

Furthermore, we discuss additional details which are needed to implement the general technical concept. Amongst the additional problems to solve is the fixing of a top Ge plate on the optical layers. As an alternative to the Ge plate, chemical deposition of a thick Ni cap layer is presented.

This chapter also addresses technological measures to improve the transparency properties of the waveguide. In particular, different polishing techniques are presented in order to clean the entrance and the exit faces of the waveguide.

3.1 Fabrication steps

The fabrication steps for a representative waveguide system are shown schematically in Fig. 3.1. First, a Mo/C/Mo optical layer sequence is deposited on a 3 mm thick single crystal Ge substratee, see subfigure (a). A sputtered Ge layer (polycrystalline) of 1 μm thickness serves as first capping layer above the optical films, finishing the block denoted as the WG wafer.

An additional thick and absorbing capping layer is needed to block the beam areas not impinging onto the waveguide entrance. Therefore, a second so-called cap wafer (Ge, 440 μm) is bonded onto the WG wafer by an alloying process. Bonding was achieved by a thin InSn alloy as shown in subfigure (b). The alloy is 'sandwiched' between the WG and cap wafers, under pressure and heated up under vacuum conditions as illustrated in subfigure (c).

The resulting one-dimensional waveguide 'sandwich' is then cut into slices by a wafer dice as shown in subfigure (d). The cutting process leads to smearing of material at the entrance and exit faces. Therefore the multilayer slices were further treated using the Focused Ion Beam (FIB) polishing as illustrated in subfigure (e).

Finally, two-dimensionally confining x-ray waveguides are obtained by gluing two polished waveguide slices on top of each other in a crossed geometry, see subfigure (f).

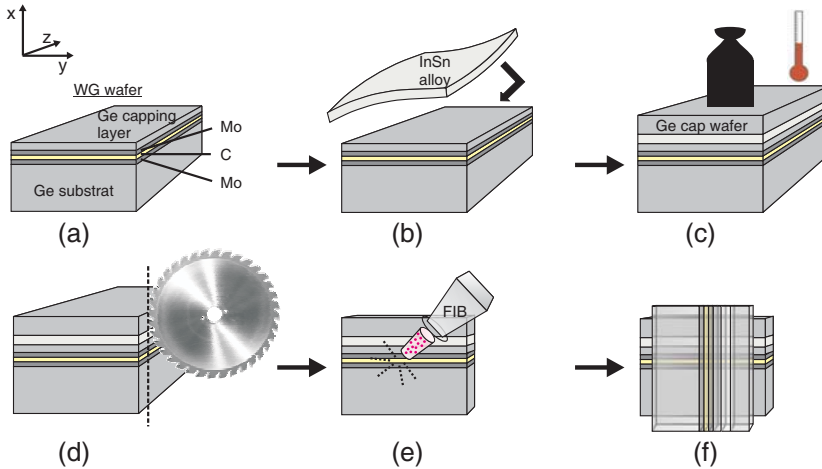


Figure 3.1: Schematic illustrating the different steps of the waveguide fabrication.

3.2 Deposition of optical layers

The optical films are deposited using Magnetron sputtering (MAK, US Inc.). The use of magnetron cathodes enables the homogeneous deposition on the large $70 \times 70 \text{ mm}^2$ face of the Ge substrates. The inert gas employed is Ar at a pressure of 1.8×10^{-3} mbar which leads to pure and dense layers avoiding their oxidation. The average target voltage and the average target current was 334.5 V and 240 mA in case of Mo as well as 575 V and 810 mA in case of C, respectively.

The thickness of the individual layers is controlled by reflectivity measurements (Incoatec GmbH). Fig. 3.2 shows the calibration curves of a SiO/Mo and a SiO/Mo/C layer sequence on a Si substrate measured at a photon energy of $E = 8.048 \text{ keV}$ (Cu-*K* line). The experimentally obtained reflectivity curves are modeled using the Marquardt curve fitting algorithm [78]. The thickness of the Mo layer obtained in (a) is 30.2 nm and the thickness of the C layer in (b) is 19.2 nm. The roughness of the individual layers is sub-6 Å allowing for high transmission of the x-ray waveguides. The parameters as obtained from modeling of the reflectivity curves are summarized in Tab. 1.

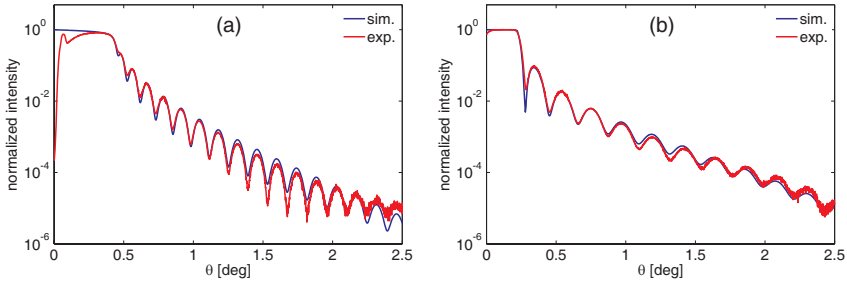


Figure 3.2: Measured reflectivity as a function of the angle of incidence θ along with the simulation of (a) SiO_2/Mo and (b) $\text{SiO}_2/\text{Mo}/\text{C}$ layer sequence on a Si substrate.

SiO_2/Mo				
N	material	thickness [nm]	roughness [nm]	density [g/cm^3]
1	Mo	30.24	0.48	10.22
2	SiO_2	1.07	0.57	2.10
substrat	Si	-	0.52	2.33
$\text{SiO}_2/\text{Mo}/\text{C}$				
N	material	thickness [nm]	roughness [nm]	density [g/cm^3]
1	C	19.21	0.44	2.30
2	Mo	0.96	0.45	10.22
3	SiO_2	0.98	0.47	2.10
substrat	Si	-	0.59	2.33

Table 1: Thickness and roughness of the individual layers as obtained from modeling of the reflectivity curves using the Marquardt algorithm.

3.3 Wafer cleaning

The waveguide sample without additional beam blocking material is cut into blocks of $10 \times 10 \text{ mm}^2$ by the wafer dicer. These blocks have to be cleaned after contact with the contaminated cutting water. The same holds for the tailored cap wafers. For the cleaning process, the samples are successively put into the following solutions:

- ammonia cleaner RW77 (Tickopur) 5% concentration, 15 min ultrasonic bath;

- distilled water, 15 min ultrasonic bath;
- acetone, 15 min ultrasonic bath;
- methanol, 15 min ultrasonic bath;
- distilled water, 15 min ultrasonic bath;
- distilled water and isopropanol dip, then drying of the samples with nitrogen.

3.4 Bonding process of the Ge cap wafer

The top face of the WG wafer and the cap wafer consist of Ge. Both faces are bonded by the use of an InSn alloy (see below), shown in Fig. 3.3. In order to improve the bonding interlayers of Cr and Ni are deposited on both Ge faces using electron beam evaporation (Leybold Univex 350). The thin Cr layer (3 nm thickness) acts as an adhesive layer between the Ge and the relatively thick (120 nm) and strongly absorbing Ni layer.

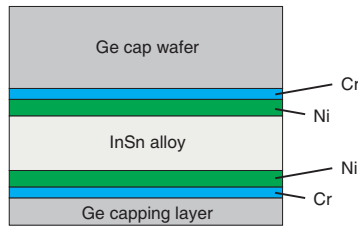


Figure 3.3: Schematic illustrating the layer sequence above the optical layers in case of a waveguide with a bonded beam blocking material. Note that the Cr and Ni layers are not shown in Fig. 3.1.

The bonding material must ensure adhesion and wetting properties on the Ni faces. Different alloys were tested, lead and lead-free alloys. Only In containing alloys offered sufficient wetting on the Ni faces. In alloys have some favourable properties such as the low melting point [79]. Best adhesion properties were obtained with the In52Sn48 alloy in form of 25 μm thick ribbon (GPS Technologies GmbH, indalloy number 1E, $T_{\text{solidus}}=118^\circ\text{C}$). To further improve the bonding process, the alloy ribbon which is 'sandwiched' between the Ni faces of the WG and cap wafers is put under a pressure of $p = 1 \text{ bar}$ ¹⁰, and heated up

¹⁰We have used a weight of 3 kg which is put onto the top face of 3 equidistantly placed samples, each having a lateral extension of $10 \times 10 \text{ mm}^2$.

to $T = 250^\circ\text{C}$ under vacuum conditions (sub-1 mbar). The reproducibility of the bonding process is improved if the fabrication steps are carried out under clean room conditions in order to avoid contaminations at the interfaces of the materials.

Due to the thickness of the In₅₂Sn₄₈ layer, the alloy must behave as a beam blocking material on a wide x-ray energy range, too. The transmission of a 500 μm thick In layer at an energy range of 8-20 keV [80] is shown in Fig. 3.4 giving an estimate for the beam blocking behaviour. Note that, the transmission of Sn with an atomic number of 50 is even lower than of In with an atomic number of 49. In summary, the In₅₂Sn₄₈ alloy offers a sufficiently high primary beam absorption for most waveguide applications up to 18 keV.

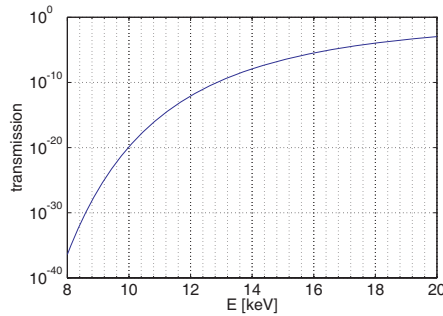


Figure 3.4: Transmission of a 500 μm thick In layer as a function of photon energy.

3.5 Electroless Nickel plating

Electroless nickel plating (EN) is an alternative for the Ge cap wafer. Ni offers higher absorption than the In₅₂Sn₄₈ alloy as shown in Fig. 3.5 making the electroless nickel plating technique suitable for x-ray waveguides operating at energies even up to 20 keV. Due to the K absorption edge, Ni is less applicable as a beam blocking material for energies below 8.33 keV.

In analogy to the bonding process, a 3 nm thick Cr and a 120 nm thick Ni layer is deposited on the Ge capping layer of the waveguide block by electron beam evaporation (see Fig. 3.6). We used a low Phosphor EN electrolyte solution (Enfinity 4LF, Enthone) for the deposition of a wear resistant and uniform beam blocking layer onto the Ni face. The deposited NiP layer has a 2-4 weight % P concentration and thus does not decrease the absorption properties significantly compared to a pure Ni layer. Although the 4LF solution is suitable for

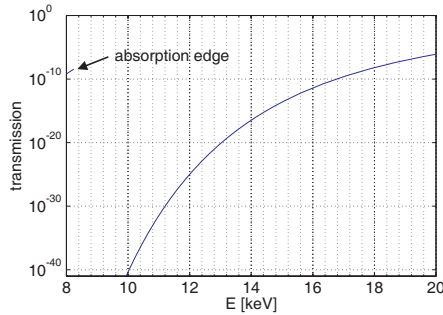


Figure 3.5: Transmission of a 500 μm thick Ni layer as a function of photon energy.

the deposition on non-metallic surfaces, the electron beam evaporated Ni layer optimizes the deposition of the NiP layer.

EN is an auto-catalytic chemical technique where the EN activation and the deposition rate is controlled by the temperature and the ph-value of the solution. The process relies on the presence of a reducing agent (sodium hypophosphite) which reacts with the metal ions to deposit the NiP alloy.

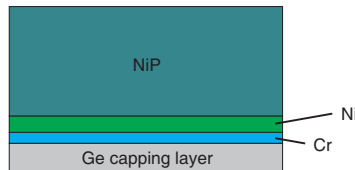


Figure 3.6: Schematic illustrating the layer sequence above the optical layers in case of an EN fabricated waveguide.

We chose a 200 ml EN solution and a glass ph-meter in a non-reactive beaker glass placed on a heating plate (see Fig. 3.7). A magnetic stirrer is used to control the electrolyte circulation. The solution is heated up to $T = 83^\circ\text{C}$ and depending on the exact electrolyte composition the ph-range for the EN activation is 5.4 – 5.6. In order to prevent sample motion, the sample is fixed on a non-reactive teflon holder by a masking lacquer (Toluol-PVC-lacquerGalvano resist SLOWAX, Schlötter Galvanotechnik) which is not affected by the electrolyte and easily removable after deposition.

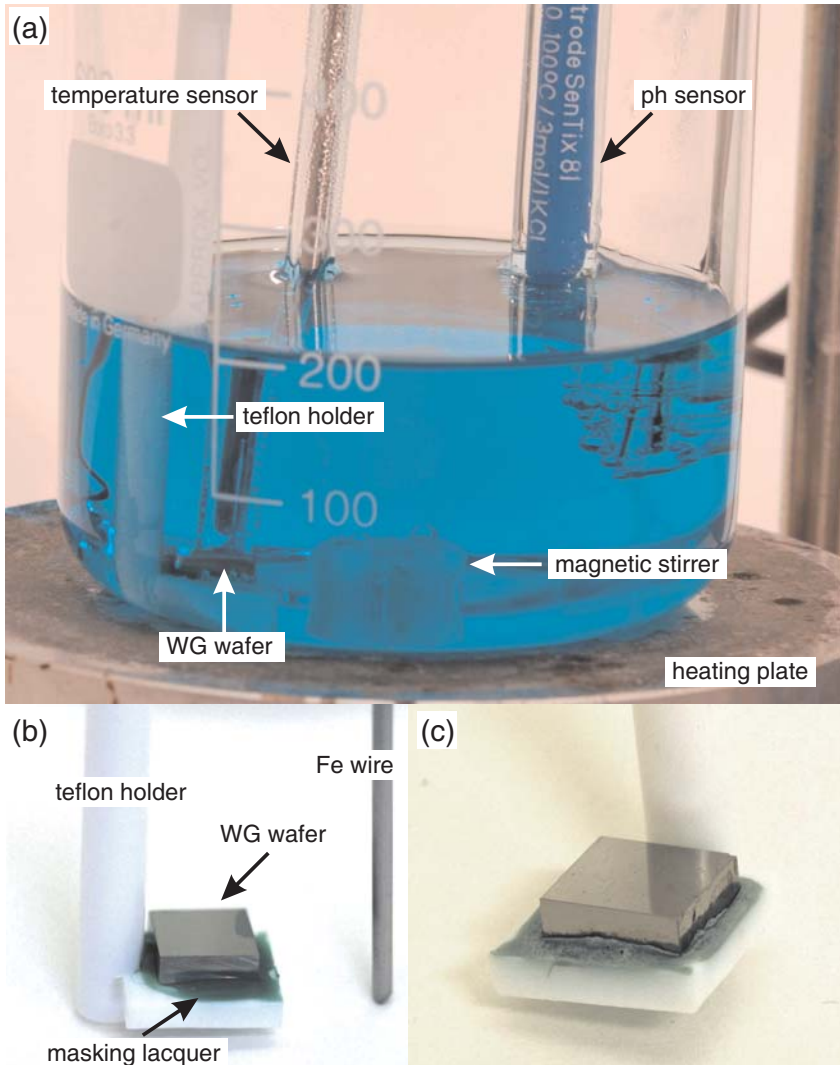


Figure 3.7: (a) Electroless nickel bath along with the WG wafer and the different constituents for the EN process. (b) The WG wafer fixed on the teflon holder using a masking lacquer before plating and the Fe wire used for activation of the EN process. (c) Semi bright Ni deposit on the WG wafer surface after 1 h of EN plating.

Ni and less noble metals self-initiate nickel plating since they have self-catalytic acting surfaces. We observed that the waveguide sample hardly self-initiates nickel plating. We assume that the thin Ni layer on the top face of the waveguide does not have the self-catalytic properties of bulk Ni samples. Initiation of the nickel plating process can be achieved by activating the surface. Activation can be achieved by seeding the surface with self-catalytic metals. One way of doing this is to simply contact the surface with a self-catalytic metal. The activation of the waveguide block includes two steps. First, the sampled is dipped in a 1:80 HCl solution (pickling, removes oxides) for a few seconds only preventing the acid to affect the optical layers of the waveguide. After placing the holder in the solution, the deposition starts by activating the Ni face by a corrosion-free (to prevent contamination of the bath) Fe wire previously dipped in a 1:2 HCl solution. After contact with the Fe wire, instantaneously blistering at the waveguide surface indicate the initiation of the nickel plating process.

The deposition rate at the beginning is approximately 22 $\mu\text{m}/\text{h}$ and can be increased by choosing higher temperatures up to 89°C or higher ph-values up to 6.2. A 0.1 higher ph-value or a 1°C higher temperature increases the deposition rate by 1.5 $\mu\text{m}/\text{h}$. The Ni content in a 200 ml solution is 1 g at the beginning corresponding to 100 % activity. The Ni consumption is approximately 0.2 mg/h for a 10×10 mm² WG block surface. Thus, after 10 h the activity is still 80 %, and for a roughly 200 μm thick NiP layer there is no need to regenerate the electrolyte solution during the EN process. However, in practice, it is difficult to avoid evaporation of the electrolyte solution. Further, even if the faces of the WG wafer on which the NiP layer should not be deposited are protected by the masking lacquer, there might be additional unwanted Ni deposition on the sample and Ni precipitation in the solution. Therefore, it is recommended to choose at least a 400 ml solution for thick NiP layers.

Several factors may lead to problems in the EN process such as organic or metal impurities in the electrolyte bath. Most likely, the restricted sample pre-treatment (acid treatment might affect the optical layers) causes often observed roughness on the deposited layers.

In the following, a detailed description of the EN process used is presented:

- passivating of the following constituents in a HNO₃ solution for 60 min: 1000 ml beaker glas, teflon sample holder, magnetic stirrer, temperature and pH sensor;
- rinsing of the constituents using acetone and distilled water;
- bath formulation 200 ml with the Enfinity 4LF solution: 100 ml distilled water, 47.5 ml part B, 12.5 ml part C, 2.4 ml part D, 37.5 ml distilled water;

- placing of the beaker glass on the heating plate which is connected to the temperature control unit, bath circulation using the magnetic stirrer (maximum speed circulation), capping of the beaker glass using an aluminium foil;
- heating-up of the bath: 83°C, at stable temperature the pH value should be 5.5 ± 0.1 (pH regulation possible using NaOH (1 ml for +0.2 pH value increase) or HCl);
- low-to-middle speed circulation, fixing of the lower side of the waveguide sample on the teflon holder using the masking lacquer;
- dipping of the sample holder in 1:80 HCl solution for a few seconds, circulation stop, placing of the sample holder in the solution, sample should be approximately on the level of the stirrer;
- dipping of the corrosion-free Fe wire in 1:2 HCl solution for 10 s, careful contacting of the Fe wire on the sample surface for a few seconds until blistering at the sample surface is observed;
- low-to-middle speed circulation, process duration 10 h, continuous checking of the temperature, the pH-value and the quality of the sample surface (semi bright deposits are expected).

A widely used alternative to EN is electroplating which has also been tested on the WG wafer. Compared to electroplating, EN has two crucial advantages. It provides an even deposit regardless of sample geometry, and once the sample is activated, there is no need for a conductive contact on the face to be deposited.

3.6 Cutting process

In the first fabrication step, the approx. 3 mm thick WG wafer is cut into $10 \times 10 \times 3 \text{ mm}^3$ blocks using a dicing saw (DISCO DAD 321) and a diamond dicing blade (DISCO NBC-ZB 1070 59x0.15x40). The sample is fixed on the lower side on a dicing tape sheet (Type: 1008RL-11.0, Ultron Systems Inc.). The optical layers are protected by a synthetic resin lacquer (Illmar P4, Pieplow & Brandt GmbH). A thin lacquer film is coated on the sample surface using a paint brush and is then dried for 2 h. The lacquer is removed using acetone after cutting. Cutting at a feed rate of 0.5 mm/s is carried out in a two step process preventing breakage of the WG wafer. The base of the first cut remains 2.5 mm away from the waveguide base. The second cut goes through the total height of the WG wafer. The cutting of the WG wafer with an additional bonded cap wafer was successful down to a slice thickness of sub-150 μm . The difficulty in this cutting process

relies on the fact that the relatively ductile InSn alloy (tensile strength 1720 PSI [81]) is surrounded by the comparably hard Ge substrate and cap wafer. The reproducibility of the sample cuts is higher for the thicker slices, sub-400 μm slices sometimes suffering from a chipping of the cap wafer. Concluding on the difficulties of the cutting process: In view of the large lateral sample dimensions compared to the desired sample thickness, the brittleness of the sample material and the different mechanical properties of the waveguide constituents it is rather astonishing that intact sample slices of sub-150 μm can be prepared.

The WG wafer with the EN fabricated cap layer have the opposite problem of an enhanced NiP layer hardness (Vickers Hardness Number $VHN = 700 \pm 30$ HV [82]) compared to the Ge substrate and the optical layers. Further, the effect of compression stress at the Ge/(Ni-NiP) interface might be taken into account. The compressional stress induced by the dicing blade is able to produce shear strain at the Ge/metal interface resulting in crack formation starting at the Ge surface (see Fig. 3.8). A breakage of the Ge substrate part of the slices is often observed while the NiP layers usually remained intact. We obtained slices down to minimal 1 mm thickness.

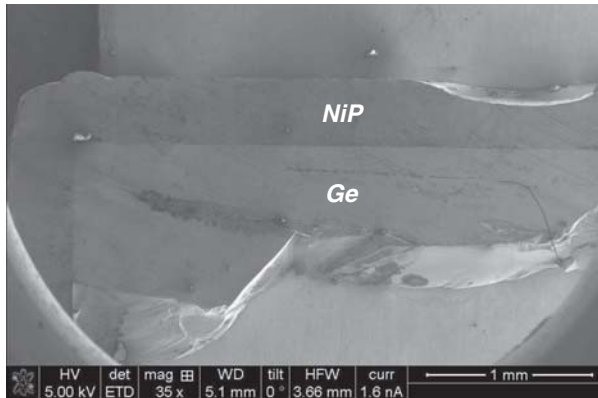


Figure 3.8: Scanning electron microscopy (SEM) image of an EN fabricated waveguide slice. The Ge substrate of the WG wafer is broken at the lower side.

3.7 Waveguide polishing

Highly efficient Ge/Mo/C/Mo/Ge waveguides need slice thicknesses of sub-500 μm . Therefore, the EN fabricated slices are mechanically polished after

cutting, applying the same sample preparation technique as used for transmission electron microscopy (TEM) samples. For the polishing, the WG slice is glued (Cristalbond mounting wax 40-8150, Buehler) on a borosilicate glass (Gebr. Rettberg GmbH) between two additional Si wafers which are used to fix the waveguide and to determine the actual thickness of the slice during polishing. The waveguide is successively polished with wet abrasive paper (kernel: PS11 P500C + P1000C, Klingspor, lubricant: water) and a diamond paste (Winter diaplast SS D15-D1, lubricant: Winter diaplastol, Saint-Gobain GmbH) on a dimpling disc (Beta Grinder-Polisher, Buehler).

Although the 'TEM' technique enables polishing up to 1 μm face roughness, an additional FIB (Nova 600 Nanolab, FEI) polishing step is needed to bare the entrance and exit sides of the waveguide slices (see Fig. 3.9). As mentioned above, cutting leads to smearing of material at the slice faces in case of bonded waveguides, too. Typical parameters for the FIB polishing of the optical layers and creating of markers are shown in Tab. 2. Given these parameters, one FIB area is limited to approximately 350 μm length along the guiding layer of the waveguide (y-direction of the horizontally placed waveguide). The polishing of such an area takes about 70 min. The markers (not shown in Fig. 3.9) are used to localize the FIB areas on the on-axis microscope in an experiment on one hand and to achieve orthogonality of two-crossed waveguide slices on the other hand.

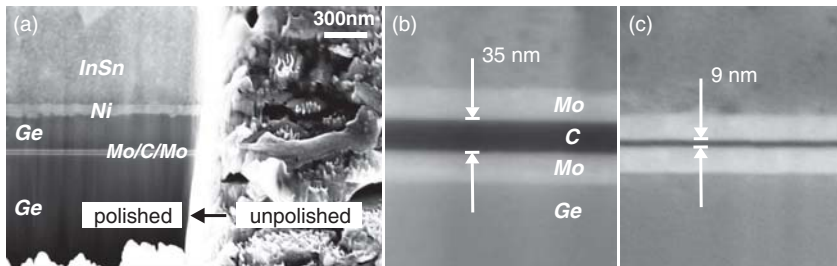


Figure 3.9: (a) SEM image of a bonded waveguide slice showing the waveguide exit sides before and after FIB polishing. The 35 nm and 9 nm C guiding layers are clearly identified as shown in the high resolution images (b) and (c), respectively. SEM parameters: (a) accelerating voltage EHT = 10 kV, working distance WD = 4 mm, magnification mag = 200 kx; (b) EHT = 10 kV, WD = 3 mm, mag = 200 kx; (c) EHT = 10 kV, WD = 4 mm, mag = 300 kx.

Fig. 3.9 (a) shows the exit sides of a bonded waveguide slice after FIB polishing, exhibiting the C guiding layer, the Mo interlayers, the Ge cladding, the evaporated Ni layer and the bonding InSn alloy. The 3 nm thick Cr layer can hardly

be identified. The right hand side of the scanning electron microscopy (SEM) image Fig. 3.9 (a) clearly demonstrates the need for polishing. The 35 nm C and the 9 nm C waveguide layer systems are exemplarily shown in 200 kx and in 300 kx magnification (SEM: Leo Supra 135, Zeiss NTS) in Fig. 3.9 (b) and (c), respectively.

Parameter	Optical layers	Marker
EHT [kV]	30	30
Ion current [nA]	5	5
x-size [μm]	10-350	10-20
y-size [μm]	10	60-150
z-size [μm]	1	0.8-1
Rotation [deg]	-10	0
Dwell time [ns]	300	300
Overlap (x,y-direction) [%]	50	50
Scan Type	CCS Raster	RCS Raster

Table 2: The table shows the FIB parameters that were used to clean the optical layers and to create markers. For further description see [83, 84].

3.8 Crossing of multilayer slices

Two polished waveguide slices are glued on top of each other by a solvent free two part epoxy resin adhesive (UHU Plus schnellfest, working time 5 min, final strength 1900 N/cm^2), applied only to the Ge sides away from the interaction of the optical films. Orthogonality is achieved by marking the adhesive bond sites by FIB polished $10 \times 80 \mu\text{m}^2$ areas and in-situ stereo light microscopy (Stemi DV4, ZEISS, 32x magnification) during the bonding process.

First crossed waveguides are fixed on a $200 \mu\text{m}$ thick W lamella as shown in Fig. 3.10. The lamella has a thin $500 \mu\text{m}$ slab on a level of the optical films. The strongly absorbing W suppresses possible higher harmonics of the primary beam. The P10 beamline Petra 3 setup dedicated to waveguide-based imaging uses a small W pinhole to suppress residual scattering of the beam exiting the Kirkpatrick-Baez (KB) mirrors [85]. Here, the waveguide slices are fixed on an adapted and easily removable iron holder.

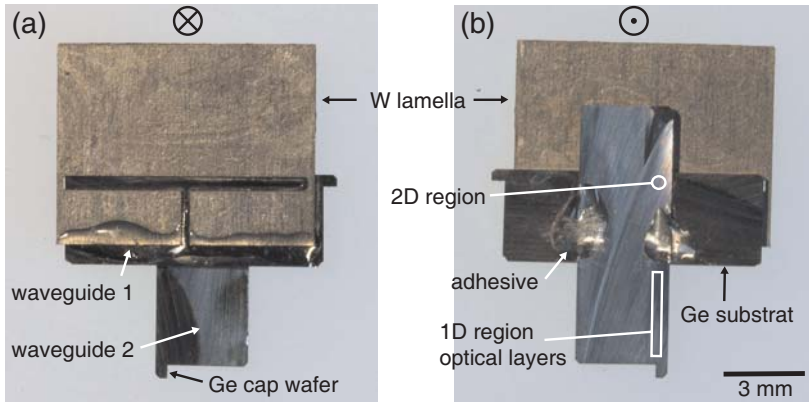


Figure 3.10: Two crossed waveguide fixed on a W lamella, shown from the front side (a) and from the back side (b) where the two-dimensional confined waveguide beam exits.

3.9 Conclusion

Magnetron sputtering is an ideal technique for the fabrication of multilayer slices due to the low interface roughness and the controlled thickness of the optical films. Further, the possibility of sputtering interlayers such as Ni and NiO (reactive sputtering) improves the transmission properties of waveguides at lower x-ray energies.

An additional beam blocking material above the optical layers is needed to absorb the tails of the primary beam. Considering waveguides with an additional Ge cap wafer, bonding by use of an InSn alloy and subsequent cutting proved to be efficient and relatively simple fabrication techniques to obtain thin waveguide slices. The difficulties in the cutting process of EN fabricated waveguide might be overcome by plating pre-cut waveguide slices. The use of mechanical and FIB polishing was not only successful to clean the waveguide entrance and exit sides but further enabled to correct the waveguide length up to sub-1 μm .

At high x-ray energies and relatively large primary beam diameters EN fabricated waveguides offer higher absorption allowing for shorter waveguide lengths.

As discussed in [47], the serial arrangement of two crossed multilayer slices glued onto each other presents a compact device, where the horizontal and the vertical focal planes of the waveguide are close to each other (within the thickness of the second waveguide). Important advantages of this scheme are the compatibility

with a wide range of thin layer deposition techniques, geometric parameters and material choices. Compared to channel waveguides prepared by electron lithography, smaller guiding core diameters and more complex layer systems become amenable.

4 Experiments I: X-ray waveguide characterization

In this chapter the angular acceptance, the transmission and the far-field properties of planar and two-crossed waveguides are investigated¹¹.

In section 4.1, an extended study of the planar waveguide properties as a function of the waveguide length, the guiding layer thickness and the photon energy is presented. The direct coupling of a pre-focused beam into planar waveguides is demonstrated and the transmission properties of the waveguides depending on the experimental setups are discussed (section 4.2). The characterization of two crossed waveguides is presented in section 4.3. From far-field measurements, the beam diameter in the effective confocal plane of the two crossed waveguide is retrieved using an iterative algorithm. Finally, first results of waveguide characterization at the novel holography endstation dedicated to waveguide-based x-ray imaging are presented (section 4.4).

4.1 Direct coupling into planar waveguides

In this section, we focus on the planar waveguide experiments carried out using an essentially unfocused synchrotron beam. The Ge/Mo/C/Mo/Ge waveguides measured have guiding layer thicknesses $d = 9 - 35$ nm. We demonstrate transmission and far-field properties subject to waveguide length and photon energy, along with finite-difference (FD) simulations.

4.1.1 Experimental setup BM20 beamline, ESRF

The experiments were performed at the BM20 bending magnet beamline at the third-generation synchrotron facility ESRF (Grenoble, France) where the waveguides are characterized using synchrotron radiation. The third-generation synchrotron at the ESRF operates at a rather high electron energy of 6 GeV enabling high brightness, small angular divergence and small source sizes [27]. The x-ray beam of the bending magnet source with an angular divergence of 2.8 mrad is defined by a double Si(111) monochromator, placed in the middle between two conjugate Pt mirrors for higher harmonic rejection as shown in Fig. 4.1. The energy resolution of $1.5 - 2.5 \cdot 10^{-4}$ for an energy range of 5 - 35 keV increases with decreasing wavelength. The beam size at the horizontally placed waveguide was maximal 0.04 mm (vertical) \times 2 mm (horizontal) as controlled by motorized entrance slits. Thus, the waveguide entrance front side was placed in an essentially unfocused monochromatic beam. The effect of stray radiation from the slit edges is reduced by setting the distance of the entrance slits to the waveguide to sub-15 cm. We chose an energy range of 11.5 - 18 keV for

¹¹Contents of this chapter have been published in [47], [20] and [85].

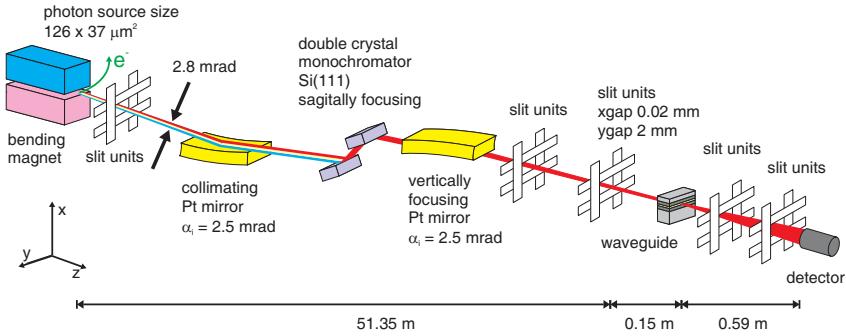


Figure 4.1: Schematic of the experimental setup at the BM20 beamline. Drawing adapted from [86].

the experiments, depending on the waveguide length l . The total photon flux impinging onto the front face of the waveguide was $1 - 3 \cdot 10^7$ photons/sec (slit settings $0.02 \text{ mm} \times 2 \text{ mm}$), depending on the ring current. The waveguide beam was measured using an one-dimensional NaI scintillator, positioned at a distance of 0.59 m from the waveguide.

4.1.2 Waveguide alignment

Fig. 4.2 shows the sample holder with four waveguides placed on the diffractometer.

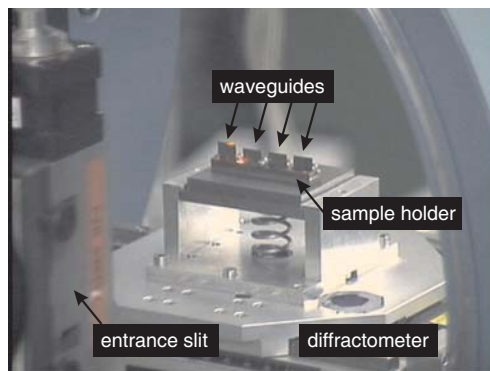


Figure 4.2: Waveguides placed on the diffractometer of the BM20 beamline.

First, the entrance of the waveguide was placed horizontally in the rotation center of the 6-circle Huber diffractometer using laser and a telescope for rough alignment. The diffractometer offers 3 translational degrees of freedom x (perpendicular to the propagation direction and the waveguide guiding layer), y (perpendicular to the propagation direction and collinear to the waveguide guiding layer) and z (collinear to the propagation direction) as well as 3 rotational degrees of freedom α (around the y axis), β (around the z axis) and γ (around the x axis). The detector rotates at an angle 2θ with respect to the z axis. In a second step, the position of the edges of the waveguide are determined by blocking the synchrotron beam by means of the waveguide. Knowing the distance of the guiding layer from the top of the waveguide, the latter is aligned by subsequent waveguide translation x and waveguide rotation α_i measurements at the height of the waveguide guiding layer as shown in Fig. 4.3. The waveguide is aligned for maximum intensity I exiting the waveguide. Note that the entrance slits and the detector slits are wide open offering higher photon flux and thus, facilitating the alignment procedure. As the waveguide guiding core is extended in y direction and the beam size d_{in} of the incident beam 3 orders of magnitude larger than the guiding layer thickness d , the rotation angle β does not play an important role in detecting the waveguide beam but should be $\beta \approx 0^\circ$ with respect to the yz plane. The same holds for the rotation angle $\gamma \approx 0^\circ$ with respect to the xy plane.

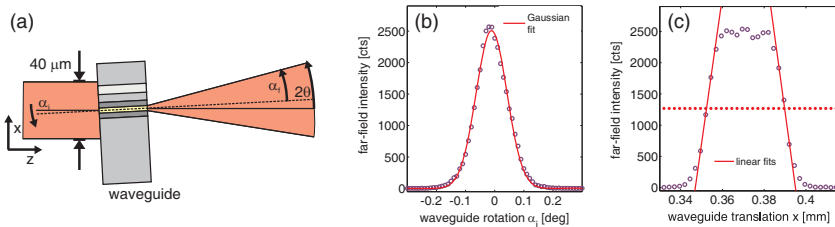


Figure 4.3: Integrated far-field intensity as a function of waveguide rotation (angle of incidence α_i) and translation through the beam (x) along with Gaussian and linear fits (solid lines). The $I(x)$ scan enables a precise measurement of the beam size d_{in} of the incoming synchrotron radiation.

4.1.3 Angular acceptance

The angular acceptance of the waveguide is determined by rotating the waveguide by an angle α_i and measuring the far-field intensity at a fixed angle $2\theta = 0$ of the detector. The far-field intensity I as a function of the waveguide rotation

α_i along with Gaussian fits are shown in Fig. 4.4. Subfigure (a)-(c) correspond to measurements of Ge/Mo/C/Mo/Ge waveguides with guiding layer thicknesses $d = 35$ nm, $d = 18$ nm and $d = 9$ nm, respectively. In case of (a) the photon energy was $E = 11.5$ keV whereas (b) and (c) were measured using an x-ray energy $E = 13.5$ keV.

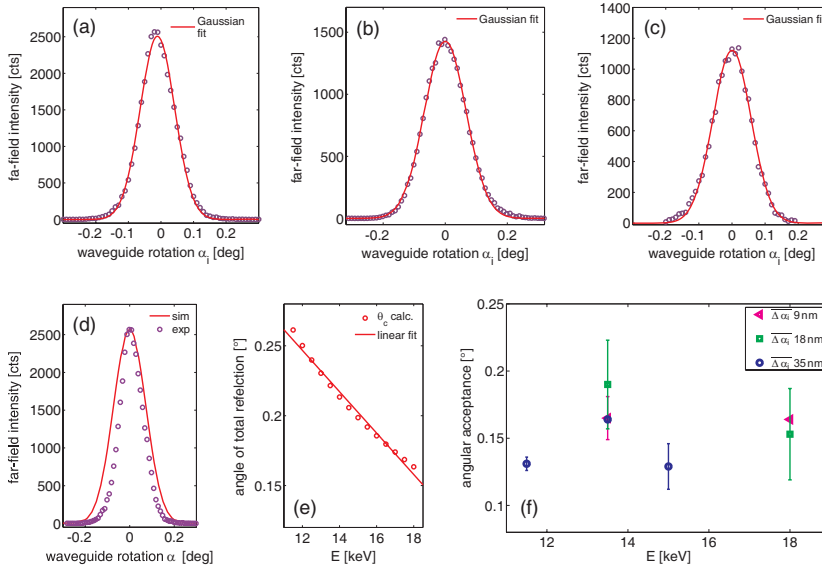


Figure 4.4: Measured far-field intensity of the Ge/Mo/C/Mo/Ge waveguide as a function of the waveguide rotation α_i in case of guiding layer thicknesses $d = 35$ nm (a), $d = 18$ nm (b) and $d = 9$ nm (c), respectively, along with Gaussian fits. (d) Angular acceptance measurement shown in subfigure (a) along with FD simulation. (e) Energy dependence of the angle of total reflection θ_c for the C/Mo interface, along with linear fit. (f) The angular acceptance as a function of the photon energy shows no clear evidence of energy on the mean FWHM $\overline{\Delta\alpha}_i$.

We compared the experimental data of the angular acceptance to FD simulations as exemplarily shown in Fig. 4.4 (d) for $d = 35$ nm. Gaussian fit to the experimental data yields a FWHM $\Delta\alpha_i = 0.125^\circ$ which is 73% of the simulated value ($\Delta\alpha_i = 0.171^\circ$). At the moment there is no explanation for this deviation. The difference in experimentally obtained angular acceptance and finite-difference

simulation is less pronounced in case of smaller guiding layer thicknesses (not shown in Fig. 4.4).

The angular acceptance depends on the angle of total reflection $\theta_c \approx \sqrt{2(\delta_{\text{Mo}} - \delta_{\text{C}})}$ at the C/Mo interface. The high δ_{Mo} value leads to high θ_c values, i.e., enhances the angular acceptance of the Ge/Mo/C/Mo/Ge waveguide compared to Ge/C/Ge waveguides. As predicted by theory, the calculated θ_c [75] decreases with increasing photon energy E as shown in Fig. 4.4 (e). In fact, δ_{C} (dispersive part of the refractive index) of the low electron C material varies less with photon energy as δ_{Mo} of the comparably high electron density material Mo. Further, we expected a slight guiding layer thickness dependence on the angular acceptance due to the mode excitation dependence on the angle of incidence.

Out of a series of angular acceptance measurements for waveguides of different length l (the angular acceptance is independent of l), we calculated the mean values $\overline{\Delta\alpha_i}$ for each photon energy. The FWHM $\overline{\Delta\alpha_i}$ from Gaussian fits of the waveguide rotation measurements as a function of the photon energy E are shown in Fig. 4.4 (f). The maximum standard deviation is 0.033° for a given energy E and guiding layer thickness d . In case of $d = 18$ nm and $d = 9$ nm we could observe a decrease of $\overline{\Delta\alpha_i}$ with increasing photon energy whereas for $d = 35$ nm this was not the case. The FWHM $\overline{\Delta\alpha_i}$ are summarized in table 3.

The angular acceptance of the Ge/Mo/C/Mo/Ge waveguides is in the range of the divergence (mrad) of Kirkpatrick-Baez mirrors and Fresnel zone plates, enabling the use of pre-focusing optics for direct coupling of the beam. This is also one of the main advantages compared to resonant beam coupling waveguides and planar waveguides using standing wave above the substrate (see section 2.1) which are comparably sensitive to the angle of incidence α_i of the incoming synchrotron radiation.

4.1.4 Transmission

After careful alignment of the waveguide translation z , the angle of incidence α_i and the rotation angle γ (may influence the propagation distance of the beam through the waveguide), the transmission T of the waveguides was determined for $\alpha_i = 0$ and $2\theta = 0$. As introduced in section 2.3, the transmission of a waveguide is calculated as the ratio of the intensity I_{in} impinging onto the waveguide front face and the intensity I exiting the waveguide

$$T = \frac{I}{I_{in}} \frac{d_{in}}{d}, \quad (4.1)$$

normalized by the size d_{in} of the incident beam at the waveguide entrance and the guiding core diameter d .

35 nm C layer						
E [keV]	l [μm]	T_{exp}	T_{sim}	$T_{\text{exp}}/T_{\text{sim}}$ (%)	E [keV]	$\overline{\Delta\alpha_i}$ [deg]
11.50	460	0.165	0.627	26	11.50	0.131
11.50	690	0.140	0.847	29	13.50	0.164
15.00	460	0.512	0.847	60	15.0	0.129
15.00	690	0.379	0.714	53		
18 nm C layer						
E [keV]	l [μm]	T_{exp}	T_{sim}	$T_{\text{exp}}/T_{\text{sim}}$ (%)	E [keV]	$\overline{\Delta\alpha_i}$ [deg]
12.50	300	0.177	0.413	43	13.50	0.190
12.50	480	0.083	0.197	42	18.00	0.153
13.00	300	0.287	0.462	62		
13.00	480	0.164	0.236	69		
13.50	300	0.315	0.513	61		
13.50	480	0.205	0.279	73		
14.00	300	0.404	0.565	72		
14.25	480	0.218	0.350	62		
9 nm C layer						
E [keV]	l [μm]	T_{exp}	T_{sim}	$T_{\text{exp}}/T_{\text{sim}}$ (%)	E [keV]	$\overline{\Delta\alpha_i}$ [deg]
13.50	200	0.256	0.305	84	13.50	0.165
13.50	300	0.072	0.107	67	18.00	0.164
13.50	390	0.036	0.044	84		
13.50	470	0.013	0.018	71		
15.50	300	0.209	0.324	65		

Table 3: Transmission and angular acceptance of planar Ge/Mo/C/Mo/Ge waveguides with guiding layer thicknesses $d = 35$ nm, $d = 18$ nm and $d = 9$ nm. On the left: the experimentally obtained transmission T_{exp} and the simulated transmission T_{sim} as a function of the photon energy E and the waveguide length l . On the right: The mean angular acceptance $\overline{\Delta\alpha_i}$ (FWHM) as function of E . The $\overline{\Delta\alpha_i}$ values are calculated from individual determinations of $\Delta\alpha_i$ as obtained from angular acceptance measurements of waveguides with different lengths.

The transmissions of the 35 nm and 18 nm C layer waveguide for 15.0 keV and 13.5 keV with waveguide lengths of 460 μm and 300 μm , respectively, are above $T = 0.5$ whereas the measured transmission of the 9 nm guiding layer waveguide is maximal $T = 0.256$ ($l = 200$ μm). The transmission T as a function of the waveguide length l for a photon energy $E = 13.5$ keV is shown in Fig. 4.5 (a). It indicates the strong transmission dependence of the 9 nm C guiding layer waveguide to the waveguide length. Likewise, Fig. 4.5 (b) illustrates the depen-

dance of the transmission on the energy of the incoming synchrotron beam. As expected, the transmission increases for larger guiding layer thicknesses. The experimental results, summarized in table 3, are below the efficiencies simulated by FD, but the overall trend is in agreement with the simulations. Most of the waveguides measured reached above 60% of the ideal (theoretical) transmission.

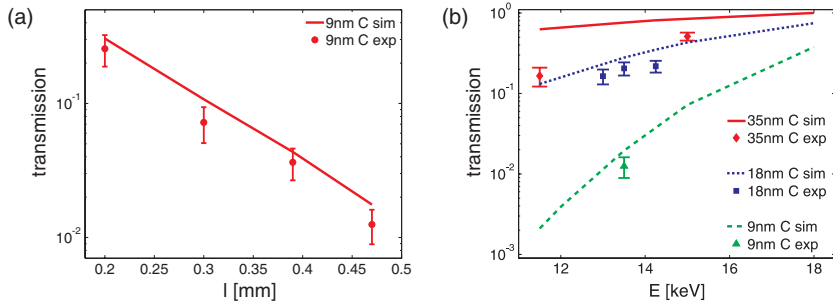


Figure 4.5: (a) Simulated and measured transmission T as a function of the waveguide length l for a 9 nm C waveguide ($E=13.5$ keV). (b) Simulated and measured transmission T as a function of the photon energy E for waveguides of length $l = (460 \pm 10)$ μm and of different guiding layer thicknesses.

4.1.5 Far-field properties

First, the shift of far-field intensity is measured with changing incidence angle α_i to align the angle of incidence to $\alpha_i = 0$, i.e., to align the entrance beam exactly perpendicular to the waveguide front end. In these scans, the center (maximum) of the far-field distribution is always found to be $\alpha_f \approx 0$. Correspondingly, the maximum position is constant in the waveguide coordinate system. Conversely, at a constant primary beam, tilting of the waveguide shifts the far-field pattern in proportion to the tilt angle α_i , as discussed in [20]. The total intensity decreases with increasing $|\alpha_i|$ as shown in Fig. 4.6 for Ge/Mo/C/Mo/Ge waveguides with guiding layer thicknesses $d = 35$ nm, $d = 18$ nm and $d = 9$ nm. Note that, if we had measured the intensity of a beam exiting an assumingly leaky area of the beam blocking material, the position of maximum intensity $2\theta_{\max}$ would not have been changed for different angle of incidence α_i .

Next, we compared the shape of far-field pattern of the waveguides. The far-field distributions as a function of the reciprocal coordinate $q = 4\pi\theta/\lambda$ for the different guiding layer thicknesses d are shown in Fig. 4.7 (a), along with the respective FD simulations. The obtained FWHM $\Delta_{q_{\text{exp}}}$ approximated by Gaussian fits (not shown in Fig. 4.7) are larger than expected from FD simulations.

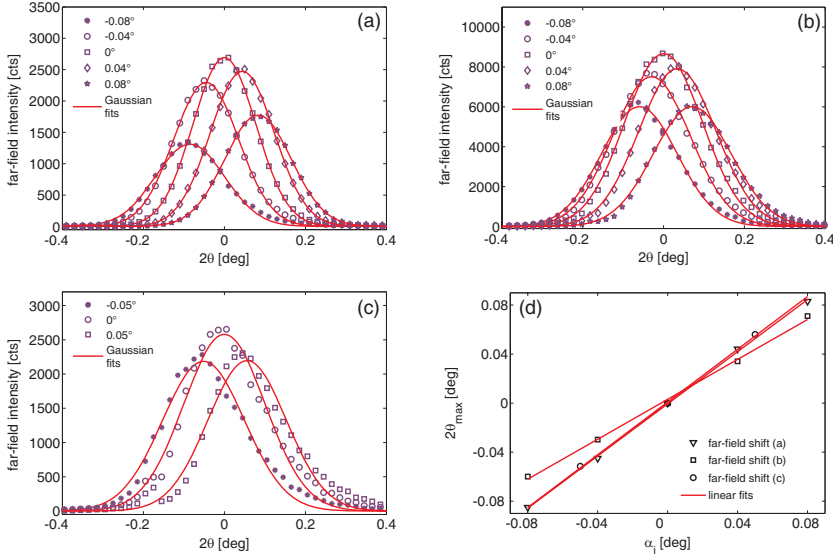


Figure 4.6: (a)-(c) Far-field intensity as function of 2θ for different incidence angle α_i , along with Gaussian fits. Subfigures (a)-(c) show measurements of the $d = 35$ nm, $d = 18$ nm and $d = 9$ nm C guiding layer waveguides, respectively. (d) The maximum position of the far-field is always approximately collinear with the axis of the (tilted) waveguide, i.e., the slopes of the curves $2\theta_{\max}(\alpha_i)$ obtained from linear fits are close to 1.

In case of the 35 nm guiding layer C, $\Delta_{f_{\text{exp}}} = 0.0185 \text{ \AA}^{-1}$ is 14% larger than the simulated value for the waveguide length $l = 690 \mu\text{m}$. As shown in the simulation 4.7 (b), a 35 nm guiding layer C waveguide supports multiple modes, leading to a periodically alternating field distribution (inside the waveguide) by interference of the modes. In section 2.4.3 we have shown that depending on the exact length of the waveguide slice, varying exit fields and thus far-field patterns of different FWHM are obtained. For comparably long waveguide length and/or lower energy, the second mode is more and more damped out by absorption. Within the experimental condition ($E = 11.5$ keV), the simulated FWHM of the far-field are in the range of $0.0155 - 0.0160 \text{ \AA}^{-1}$ for $l = 690 \pm 15 \mu\text{m}$, not including the experimentally obtained value. Accordingly, the width of the near-field distribution must be correspondingly lower than the simulated FWHM $\Delta_{z_{\text{sim}}} = 23.2$ nm, i.e. $\Delta_z = 20.0$ nm.

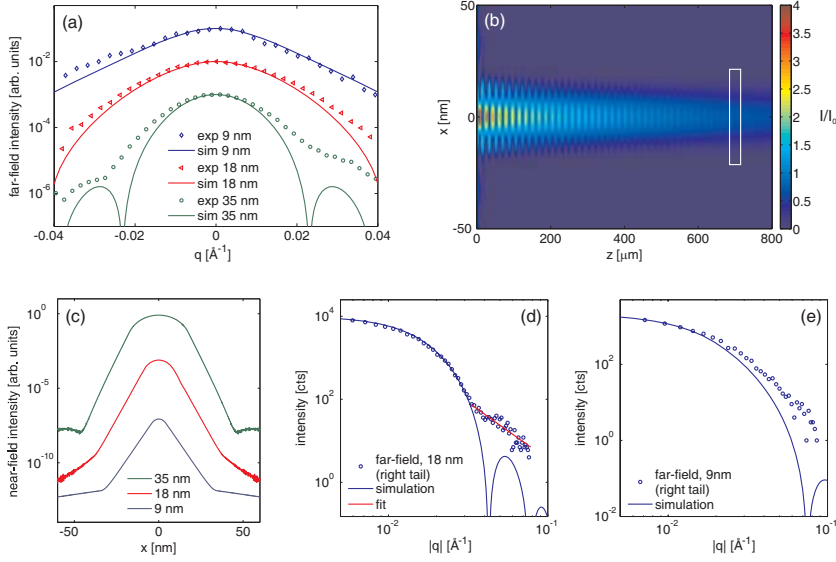


Figure 4.7: (a) The far-field intensity distributions for $\alpha_i = 0$ as a function of q , along with simulations, exhibit the guiding core dimension dependence on the far-field width. The curves are shifted for clarity. (b) The periodically alternating field oscillations are successively damped out, and for $l = 690 \pm 15 \mu\text{m}$ (white box), no significant near-field width periodicity is present in the simulation. (c) The simulated near-field distributions (shifted for clarity), corresponding to the far-field simulations in (a), indicate the broadening for increasing guiding layer thicknesses. (d) Far-field distribution of the 18 nm C waveguide shown in (a) on double logarithmic scale, along with FD simulation (solid blue line) and a quasilinear (algebraic) fit (solid red line). (e) Far-field distribution of a 9 nm C waveguide ($l = 300 \mu\text{m}$, $E = 13.5 \text{ keV}$) on the same scale and q -range as in (d).

The 18 nm C guiding layer waveguide has a length of $l = 300 \mu\text{m}$ and was measured using a photon energy $E = 13.5 \text{ keV}$. Gaussian fit to the far-field yields a FWHM $\Delta q_{\text{exp}} = 0.0257 \text{ \AA}^{-1}$ which is 9% higher than the simulated width ($\Delta q_{\text{sim}} = 0.0233 \text{ \AA}^{-1}$). Accordingly, we expect a near-field width $\Delta z = 11.3 \text{ nm}$ ($\Delta z_{\text{sim}} = 12.6 \text{ nm}$). The experimentally obtained divergence of the 9 nm C guiding layer waveguide ($l = 460 \mu\text{m}$, $E = 15.5 \text{ keV}$) differs by 2% from the simulated value ($\Delta q_{\text{exp}} = 0.0254 \text{ \AA}^{-1}$ and $\Delta q_{\text{sim}} = 0.0248 \text{ \AA}^{-1}$). Hence, the corresponding width of the near-field distribution must be $\Delta z = 8.4 \text{ nm}$ ($\Delta z_{\text{sim}} = 8.6 \text{ nm}$). The simulated near-fields are shown in Fig. 4.7 (c).

Fig. 4.7 (d) shows the line shape of the far-field distribution on a double-logarithmic scale along with the curve from the FD simulation. As discussed in [20], the far-field distribution of the 18 nm C waveguide exhibits pronounced algebraic tails $I \propto q^{-\nu}$, which are not well described by a Gaussian lineshape. A comparison to the simulation shows that the tails of the beam with an experimental exponent of about $\nu = 2.7$ forms an envelope to the oscillations with periodicity $\Delta q = 2\pi/(18 \text{ nm})$, which occur in the simulations. Note that in the simulations, the guiding layer thickness results in far-field oscillations, notwithstanding the continuity of the near-field and its derivative at the interface. However, the experiment only shows algebraic tails, which may be attributed to thickness fluctuations and/or roughness in the waveguide channel.

Fig. 4.7 (e) shows the far-field distribution of the 9 nm C waveguide. The oscillations with periodicity $\Delta q = 2\pi/(9 \text{ nm})$ shift the tails of the far-field to higher q -values. Due to the low photon flux impinging onto the front face of the waveguide and thus exiting the waveguide, the tails in the high q -range could not be measured. However, it becomes obvious from the measurements and simulations, that the decay of intensity as a function of q is comparably low in case of the 9 nm C waveguide.

Finally, we discuss the far-field distribution of the 35 nm C waveguide. In contrast to the previous mentioned far-field patterns, the measured curve shown in Fig. 4.7 (a) exhibits two shoulders which can be attributed to the side maxima of the simulations. The filling of the minima might be caused by small imperfections of the waveguide interfaces. Further, the tails of the far-field distribution are not symmetric which is not fully understood yet. In line with the larger far-field width compared to the simulation, the 'maxima' of the tails are shifted to higher q -values.

4.1.6 Beam blocking materials

In this section we address the beam blocking materials used for the waveguides. In particular, we analyzed the efficiency of the InSn alloy and the NiP layer, which are on top of the first 1 μm thick Ge cap layer (see chapter 3). Note that the x-ray beam impinging onto to the front end of the waveguide has a width of 40 μm (vertical), and therefore also hits the additional cap layers in case of the aligned waveguide as shown schematically in Fig. 4.3 (a).

The attenuation length of the beam blocking materials InSn, NiP and Ge decreases with increasing energy. At a waveguide length $l = 300 \mu\text{m}$ and a photon energy $E = 18.0 \text{ keV}$, Ge and In have an (theoretical) intensity transmission of $T_{\text{Ge}} = 1.1 \cdot 10^{-4}$ and $T_{\text{In}} = 4.2 \cdot 10^{-3}$, respectively [75]. The InSn layer of the waveguide has a thickness of approx. 2 – 3 μm . The photon intensity of the primary beam was $\approx 1 \cdot 10^7 \text{ cps}$ at a width of 40 μm (vertical). Consequently,

we expect an enhanced background signal for the measured far-field intensity of the waveguide of approx. $10^3 - 10^4$ cps. This is demonstrated in Fig. 4.8 (a), showing the far-field intensity as a function of the waveguide translation x . For x-ray beam energies up to 15.5 keV, the background signal is constantly below 10^2 cps ($T_{\text{Ge}} = 1.2 \cdot 10^{-6}$ and $T_{\text{In}} = 2.6 \cdot 10^{-4}$ at $E = 15.5$ keV). Note that longer waveguide lengths enable the use of higher photon energies.

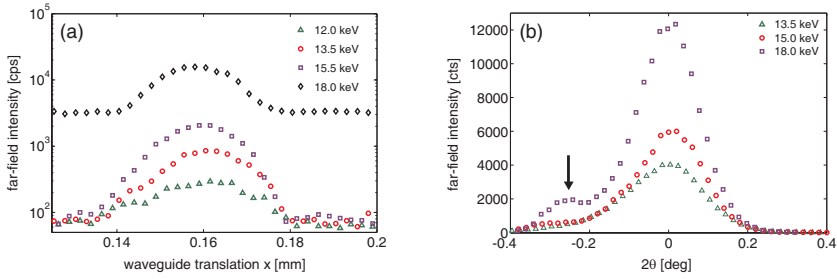


Figure 4.8: (a) InSn beam blocking material: The far-field intensity as a function of the waveguide translation z exhibits the enhanced background signal at $E = 18.0$ keV compared to the curves measured using lower photon energies. (b) NiP beam blocking material: The far-field intensity distribution as a function of 2θ indicates a leaky area of the beam blocking material (arrow).

Next, we measured the energy dependance of a 18 nm C waveguide with a NiP beam blocking layer and a slice thickness $l = 340 \mu\text{m}$. Fig. 4.8 (b) shows the far-field intensity as function of 2θ for an energy range $E = 13.5 - 18$ keV. The theoretical absorption $T_{\text{Ni}} = 2.6 \cdot 10^{-6}$ of Ni at $E = 18.0$ keV indicate that the the 340 μm thick NiP layer should be sufficient to block the primary beam of $I \approx 1 \cdot 10^7$ cps. However, a side maximum is shown at the higher energy curves. We attribute this maximum to a leaky area of the beam blocking materials or at the layer interfaces. In the present experimental setup, beam parts of leaky area are likely to be observed due to the large horizontal primary beam size of 2 mm.

4.1.7 Conclusions

The two-component waveguides combine small guiding core dimensions, i.e. high divergences of the exiting beam, with high transmissions. We have demonstrated for the first time sub-20 nm beam confinement with transmission $T > 0.5$ using a planar waveguide. Compared to Fresnel zone plates, Laue lenses and and compound refractive lenses, the achieved (secondary) source size in one dimension is lowest with the 9 nm C waveguide. Sub-10 nm beam confinement has

been demonstrated using Kirkpatrick-Baez mirrors too, at a specially dedicated beamline [51].

Simulation of the transmission and the far-field intensity distribution are in semiquantitative agreement, but also show that the simulation is still too idealized. The reproducible and well defined tails of the far-fields may be employed to increase the effective numerical aperture and thus resolution in waveguide based holography. The tailoring of the near-field evanescent wave and the corresponding algebraic tails in the far-field will indeed be an important next step in optical design. Finally, the used beam blocking material proved to be efficient up to energies of 15.5 keV for waveguide length $l = 300 \mu\text{m}$.

4.2 Direct coupling of a pre-focused beam into planar waveguides

This section demonstrates the direct coupling of focused synchrotron beam into the front face of a planar two-component waveguide using Kirkpatrick-Baez mirrors and Fresnel zone plates. Locating the waveguide in the focus of a pre-focused device allows for the combination of the high flux density provided by the focusing device with an even smaller beam size and well-defined intensity distribution of multi-modal and mono-modal waveguide.

4.2.1 ID22 experiment: setup and results

In contrast to the bending magnet beamline BM20, the ID beamlines at the ESRF take advantage of insertion devices (ID's) which are introduced in the straight sections of the storage ring [27].

Two undulator systems are installed at the beamline ID22 [87]: One ex-vacuum undulator (U42) with a magnet period of $\lambda_U = 42 \text{ mm}$ and one in-vacuum undulator (U23) with a magnet period of $\lambda_U = 23 \text{ mm}$, which were used simultaneously in the experiment. The energy distribution of the undulator radiation is harmonic and each harmonic has an energetic width of $\Delta E/E \approx 10^{-2}$. The undulators are operated with different harmonics, depending on the energy. The maximum intensity of the undulator spectrum as a function of the energy can further be fixed by the gap opening, as discussed in [88].

As it is the case at the BM20 beamline, for monochromatization and suppression of high energy contributions a combination of mirrors and monochromator crystals can be used, located in the optical hutch of the beamline. The ID22 mirror is made of Si with additional Pd and Pt coating which are separated laterally. The two silicon single crystals used as monochromators provide a x-ray beam with a monochromacy of $\Delta E/E \approx 10^{-4}$. Three different beam modes

can be chosen: monochromatic, pink (without monochromators) and white (without monochromators and mirrors).

A Kirkpatrick-Baez (KB) mirror optic [89, 90] was used to increase the photon flux density in front of the waveguide (see Fig. 4.9). The KB is located in the first experimental hutch of the beamline. For the experiment, the waveguide was placed in the focal spot of the KB. Two elliptically curved RH coated Si mirrors demagnified the x-ray source into a spot of $8 \mu\text{m} \times 3.7 \mu\text{m}$ in horizontal and vertical direction, respectively, at a photon energy $E = 12.0 \text{ keV}$. The spot size of the KB mirrors was measured by translation of a Au stripe, recording both the transmitted intensity by a diode and the AuL_α fluorescence by a silicon drift detector (Vortex-EX, SII NanoTechnology Inc.) [29]. The respective nominal focal distances are $f_h = 190 \text{ mm}$ and $f_v = 390 \text{ mm}$ from the middles of the horizontally and vertically focusing mirrors, respectively [48]. The far-field of the KB mirrors at a distance of 2.955 m from the focal spot is shown in Fig. 4.10.

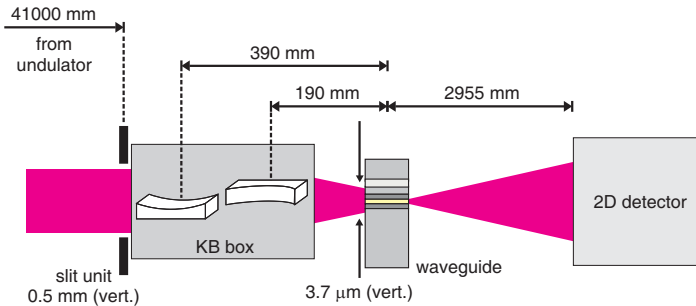


Figure 4.9: Focusing of the x-rays onto the front end of the waveguide using a KB mirror system and recording of the waveguide beam on a 2D detector. The experiment at the beamline ID22 is carried out in the so-called pink beam mode.

The experiment was carried out in the pink beam E mode using the intrinsic monochromaticity of the undulators and the bandpass of the KB mirror system, resulting in about $\Delta\lambda/\lambda \approx 0.02$. In addition, the flat horizontally deflecting Pd coated Si mirror was used for higher harmonic rejection. The waveguide was placed horizontally on a Huber stage (Huber Diffractionstechnik, Rimstig, Germany) equipped with additional microstep translation stages (Micos GmbH, Eschbach, Germany) for the high resolution translational axes. The two-dimensional detection of the waveguide far-field was carried out using a charge-

coupled device (CCD) camera (PI-LCX:1300, 1340×1300 pixels, $20 \times 20 \mu\text{m}^2$ pixel size, Princeton Instruments) positioned at a distance of 2.955 m from the waveguide.

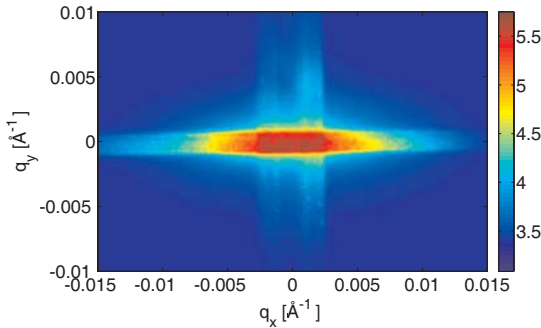


Figure 4.10: Far-field as a function of the reciprocal coordinates q_x and q_y of the focused beam from the Kirkpatrick-Baez mirror system. The intensity in [cts] is encoded in the colormap. The visible pattern in the far-field is very likely caused by imperfections on the surface of both mirror.

Fig. 4.11 (a) shows the far-field pattern as a function of q_x and q_y of the 9 nm C waveguide with a length $l = 340 \mu\text{m}$ as measured on the 2D detector (exposure time 0.1 s). Compared to the far-field of the KB mirrors (see Fig. 4.10), the waveguide pattern is strongly extended in vertical direction due to the significantly reduced beam size. The linescan of the diffraction pattern along q_y shown in Fig. 4.11 (b) exhibit pronounced maxima and minima in the center and at the left tail which are not described by theory. We attribute these fringes to the smeared exit face of the waveguide which has not been polished prior to this first measurement using a pre-focused x-ray beam.

The far-field pattern as a function of the waveguide rotation α_i is shown in Fig. 4.11 (c). Gaussian fit to the measured curve yield a FWHM of $\Delta_{\alpha_i} = 0.131^\circ$. Hence, the angular acceptance of the waveguide is not altered by the focused beam impinging onto the front face of the waveguide.

The total photon flux exiting the waveguide was $1.6 \cdot 10^6$ ph/s as measured by a diode. With a photon flux of $3.5 \cdot 10^{11}$ ph/s impinging onto the front face of the waveguide and a beam size of the focused beam $D_v = 3.7 \mu\text{m}$ vertical to the waveguide guiding layer, the transmission is calculated to $T_{\text{exp}} = 0.002$. The measured transmission is significantly lower than the simulated transmission of $T_{\text{sim}} = 0.020$.

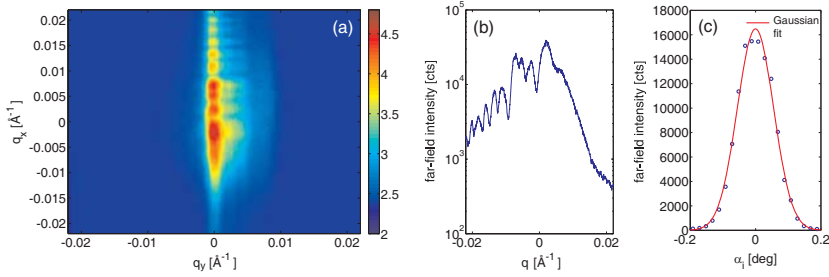


Figure 4.11: (a) Far-field distribution of the unpolished 9 nm C waveguide as a function of q_x and q_y (logscale colorbar in units [cts]). (b) The linescan of the farfield presented in (a) shows characteristic fringes. (c) Measured angular acceptance along with Gaussian fit.

We attribute the discrepancy to the fact that the simulation assumes a coherent plane wave impinging on the waveguide (under normal incidence angle), while the wave front of the KB focus may not be well described by an idealized plane wave. Hence, we must take several factors into account which lower the effective transmission of the waveguide for the given setup. The beam cross-section of 0.5 mm in front of the KB and the focal length of 390 mm (vertical focusing) results in a KB beam convergence of 0.07° . Taking the convergence angle of 0.07° of the incident beam into account, the simulated value reduces to $T_{\text{sim}} \approx 0.018$. Next, we consider the effect of partial coherence of the beam. From the theory of coherence propagation (Gaussian shell model) [91] we can calculate the degree of coherence in front of the KB. The emittance ϵ_S of a Gaussian shell model (GSM) source is given by [91]

$$\epsilon_S = \sigma_S \sigma'_S, \quad (4.2)$$

where σ_S is the source size and σ'_S the source divergence. The transverse coherence length at the undulator source ξ_S can be calculated by

$$\xi_S = \frac{2\sigma_S}{\sqrt{4k^2\epsilon_S^2 - 1}}, \quad (4.3)$$

and the degree of coherence q_S then yields

$$q_S = \frac{\xi_S}{\sigma_S}. \quad (4.4)$$

Using the definition of the angular width θ_{Ξ} of the coherent part of the beam

$$\theta_{\Xi} = \frac{\sqrt{4 + q_S^2}}{2k\sigma_S}, \quad (4.5)$$

we can determine the coherence length $\Xi(z)$ of the beam at a distance z from the source by

$$\Xi = \sqrt{\xi_S^2 + \theta_{\Xi}^2 z^2}. \quad (4.6)$$

In the vertical direction, the source size $\sigma_{S_{\text{vert}}} = 30 \mu\text{m}$ and the source divergence $\sigma'_{S_{\text{vert}}} = 5 \mu\text{rad}$ from the undulator yield a degree of coherence of $q_S = 0.18$ at the source. At a distance of 41 m from the undulator the coherence length is calculated to $\Xi_y = 85.9 \mu\text{m}$. Cutting the beam size by the 500 μm vertical slit size in front of the KB, the degree of coherence of the beam illuminating the KB increases to 0.17. Thus in front of the KB, as in its focus, about 17% of the flux is coherent in the vertical direction. Since the mono-modal waveguide accepts only the coherent flux a factor of about three in the discrepancy can thus be attributed to partial coherence. Consequently, the calculated transmission yield $T_{\text{calc}} \approx 0.003$ and thus is in approximate agreement with the measured transmission of $T_{\text{exp}} = 0.002$.

4.2.2 ID22-NI experiment: setup and results

The ID22-NI experiment is performed in the second experimental hutch of the ID22 beamline. The second hutch is under clean room condition avoiding enhanced sample contamination, and the room temperature is controlled up to $\pm 0.01^\circ$ reducing drift effects of the optical elements and motorized positioning systems. As in the case of the ID22 experiment, a KB mirror is used to pre-focus the synchrotron beam onto the front face of the waveguide. Two bent Si mirrors with graded multilayer coatings (30 W/B₄C layers with a period of 4.7 nm at the center [4]) ideally focus the x-ray beam down to sub-100 nm in both direction (at $E = 20.5 \text{ keV}$ [4]). In the present experimental setup, the focal spot in horizontal direction was $D_{\text{horz}} = 286 \text{ nm}$ at a photon energy $E = 17.5 \text{ keV}$, as measured by translation of the waveguide through the beam. The focal lengths of the vertically focusing first mirror and the horizontally focusing second mirror are $f_v = 280 \text{ mm}$ and $f_h = 93 \text{ mm}$, respectively [4].

The experiment was carried out in the pink beam mode using the intrinsic monochromaticity of the undulators and the bandpass of the KB mirror system, resulting in $\Delta\lambda/\lambda \approx 0.016$. The horizontally deflecting Pd coated Si mirror was used for higher harmonic rejection. As shown in Fig. 4.12, the waveguide was vertically placed on a compact rotator (Attocube Systems, Germany), fixed on an

additional translational stage (Princeton Instruments, Germany). The detector (CCD camera FRELON 2000, 2048×2048 pixels, $2.4 \times 2.4 \mu\text{m}^2$ effective pixel size, Analog Transient Electronics Group (ATEG) of the ESRF Instrument Support Group) was positioned at a distance of 1.185 m from the waveguide.

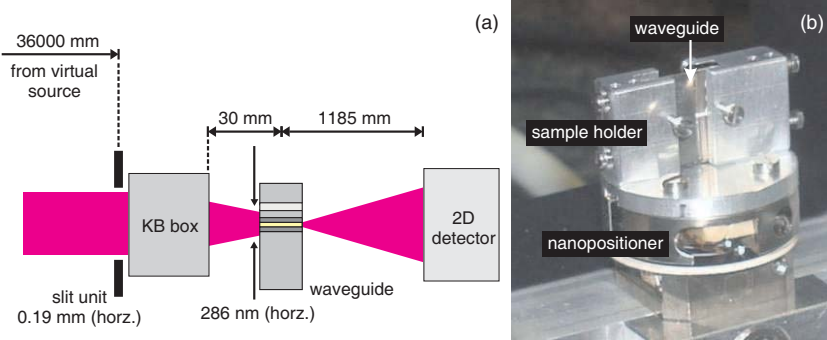


Figure 4.12: (a) Schematic of the ID22-NI experimental setup. (b) The waveguide is vertically placed on a compact rotator.

To corroborate the assumption that the 'blurred' far-field measured at the ID22 setup is due to a smeared exit face of the waveguide, we made a measurement with a polished waveguide at the ID22-NI beamline. The far-field pattern of the 18 nm C waveguide with a length $l = 1$ mm is shown in Fig. 4.13 (a)¹². In contrast to the previously presented waveguide far-field pattern, a uniform and flat intensity distribution is visible in the center. The high frequency fringes in horizontal direction are KB mirror effects (mirror imperfections). The waveguide far-field integrated over the KB area is shown in Fig. 4.13 (b). Gaussian fit (not shown) to the measured curve yields a FWHM of $\Delta q_{\text{exp}} = 0.0186 \text{ \AA}^{-1}$ which is substantially below the simulated FWHM of $\Delta q_{\text{sim}} = 0.0225 \text{ \AA}^{-1}$. Further, additional fringes are visible at the tails. The side maxima are separated by a mean value of $\Delta q_{\text{max}} = 0.0024 \text{ \AA}^{-1}$ as determined by Gaussian fits and correspond to a quasi-periodicity of $\Delta x_{\text{max}} = 262 \text{ nm}$ in the sample plane. This distance can not be attributed to a periodicity of the optical layer arrangement. In fact, the Mo/C/Mo optical layer sequence has a combined thickness of 78 nm. Besides, the Mo interlayer yields a transmission $T_{\text{Mo}} = 1.5 \cdot 10^{-8}$ which is 8 orders of magnitude lower than $T_{\text{C}} = 0.9$ of the guiding layer, at the given length and energy.

¹²Note that the FRELON CCD does not count true photons.

The total photon flux in the focal spot of the KB beam with a horizontal spot size of $D_h = 286$ nm was $1.7 \cdot 10^{10}$ ph/s and the integrated far-field intensity of the waveguide exiting beam was $3.0 \cdot 10^7$ ph/s, as measured by a diode.

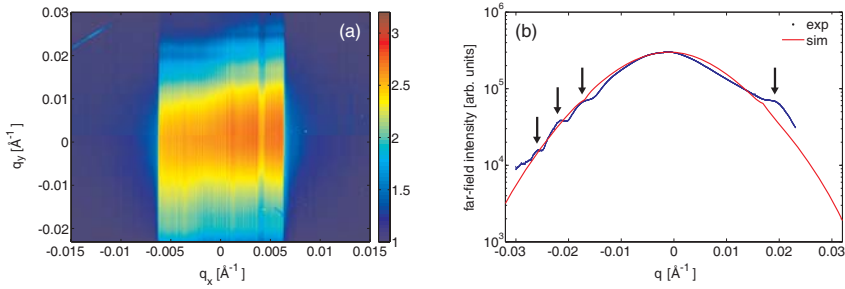


Figure 4.13: (a) Far-field distribution of the polished 18 nm C waveguide as a function of q_x and q_y (rotated by 90° , logscale colorbar: I [arb. units]). (e) Linescan (summed over the KB area) of the far-field presented in (a) along with simulation. The black arrows indicate the side maxima.

The measured transmission $T_{\text{exp}} = 0.028$ is significantly lower than predicted by finite-difference calculations ($T_{\text{sim}} = 0.331$) assuming plane wave illumination under normal incidence. Using the GSM formalism and the parameters for the source size and source divergence of the ID22 undulator, we can calculate the degree of coherence in horizontal direction. A virtual source realized by a $10 \mu\text{m}$ slit at a distance of 27 m downstream from the undulator provides a nearly completely coherent beam over the $190 \mu\text{m}$ horizontal KB slit size located at a distance of 36 m from the virtual source. The KB beam of the ID22 NI setup yields a convergence angle of 0.10° in horizontal direction. Taking the convergence of the KB beam into account, the simulated transmission reduces to $T_{\text{sim}} = 0.125$ which is still significantly below the measured transmission of $T_{\text{exp}} = 0.028$.

4.2.3 ID1 experiment: setup and results

The x-ray beam of the undulator at the ID1, ESRF, is defined by a double Si(111) monochromator, placed in the middle between two conjugate Rh coated Si mirrors for higher harmonic rejection [92]. A fixed beam-stop located after the monochromator vessel intercepts the white beam and the Bremsstrahlung radiation. The energy resolution of the x-ray beam is $\Delta E/E < 10^{-4}$. We used a Fresnel zone plate (FZP) as pre-focusing optic (see Fig. 4.14). The FZP is made of Au/Si and has a diameter of $200 \mu\text{m}$.

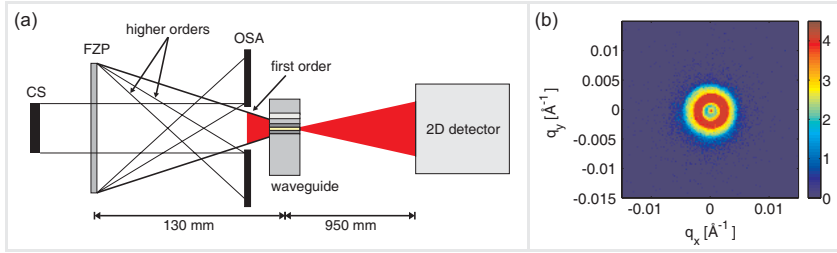


Figure 4.14: (a) Schematic of the experimental setup at the ID1 using a Fresnel zone plate as pre-focusing optic. (b) Far-field pattern of the focused beam from the FZP as a function of q_x and q_y (logscale colorbar in units [cts]).

A central beam stop (CS) with a diameter of $60\ \mu\text{m}$ was positioned in front of the FZP to block the primary beam. By using an order sorting aperture (OSA), placed behind the FZP, only the first order of the focused beam propagates to the focal plane of the FZP. The waveguide ($d = 35\ \text{nm}$, $l = 400\ \mu\text{m}$) was positioned vertically on a Huber goniometer in the focal plane of the FZP. The focal spot size of the FZP in horizontal direction is $D_{\text{horz}} = 220\ \text{nm}$ at a photon energy $E = 8.0\ \text{keV}$, as measured by translation of the waveguide through the beam. The total flux impinging onto the front face of the waveguide was $4.7 \cdot 10^9\ \text{ph/s}$. A low noise direct counting pixel detector (Maxipix, ESRF) with a pixel size of $55\ \mu\text{m}$ and an active area of 256×256 pixels was used to record the far-field pattern of the waveguide beam at a distance of $0.95\ \text{m}$ from the waveguide. A vacuum flight tube was placed in between the waveguide and the detector to prevent absorption and scattering by air.

The far-field shown in Fig. 4.15 (a) is a combination of two accumulations (exposure time each 5 s) with the detector shifted in y-direction to increase the field of view. The far-field pattern of the polished $35\ \text{nm}$ C waveguide shows similar characteristics as the diffraction pattern presented in Fig. 4.13 (a). On one hand, the far-field is not fully symmetric. On the other hand, a uniform and flat intensity distribution in the center is framed with characteristic fringes. Gaussian fit to the linescan shown in Fig. 4.15 (b) yield a FWHM of $\Delta q_{\text{exp}} = 0.0148\ \text{\AA}^{-1}$ compared to $\Delta q_{\text{sim}} = 0.0159\ \text{\AA}^{-1}$ obtained from the simulated far-field distribution.

In analogy to pre-focusing by KB mirrors, the angular acceptance of the FZP pre-focused waveguide is on the same order as for waveguides illuminated by essentially unfocused beam: Gaussian fit to the far-field distribution measured as a function of α_i yield a FWHM of $\Delta \alpha_i = 0.127^\circ$ as shown in Fig. 4.15 (c).

The focal spot was approximately 6 times larger in horizontal direction as the guiding layer thickness, resulting in a flux of $7.5 \cdot 10^8\ \text{ph/s}$ at the entrance.

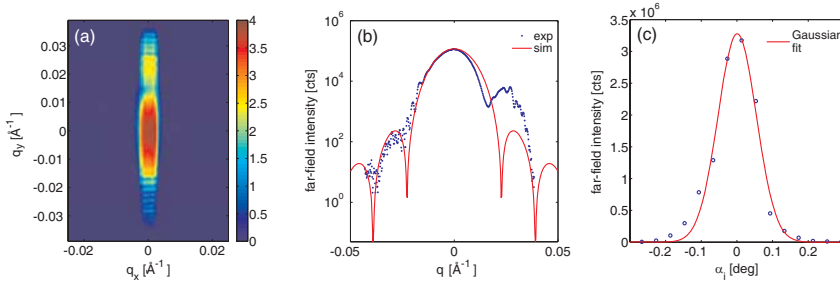


Figure 4.15: (a) Far-field pattern of the 35 nm C waveguide as a function of q_x and q_y (rotated by 90°). (b) Linescan (summed over the FZP area) of the far-field presented in subfigure (a) along with simulation. (c) Measured angular acceptance along with Gaussian fit.

The total photon flux exiting the waveguide of $1.7 \cdot 10^7$ ph/s thus corresponds to a transmission $T_{\text{exp}} = 0.023$ which is only 8% of the simulated transmission ($T_{\text{sim}} = 0.294$) assuming plane wave illumination under normal incidence angle. The FZP diameter of 0.2 mm defining the beam size and the focal length of 130 mm result in a beam convergence of 0.09° . The simulated transmission reduces to $T_{\text{sim}} = 0.256$ taking the convergence of the FZP beam into account. In the horizontal direction, the source size $\sigma_{\text{S}_{\text{horz}}} = 134 \mu\text{m}$ and the source divergence $\sigma'_{\text{S}_{\text{horz}}} = 208 \mu\text{rad}$ from the undulator yield a degree of coherence of $q_s = 0.001$ at the source. At a distance of 46 m from the undulator source the coherence length is calculated to $\Xi_y = 21.5 \mu\text{m}$. Cutting the beam size by the $200 \mu\text{m}$ horizontal slit size in front of the FZP, the degree of coherence of the beam illuminating the FZP increases to 0.11. Since the waveguide essentially accepts only the coherent flux¹³, a factor of about ten of the discrepancy between the measured and simulated transmission can be attributed to the partial coherence of the beam. Taking the convergence of the FZP beam and the effect of partial coherence into account, the measured transmission of $T_{\text{exp}} = 0.023$ is in good agreement with the calculated transmission of $T_{\text{calc}} \approx 0.027$.

4.2.4 Conclusions

The measurements of the planar Ge/Mo/C/Mo/Ge waveguide using pre-focusing optics demonstrate that a coherent flux of $10^6 - 10^7$ ph/s is obtained corresponding to a gain in flux density of about 10 – 100 compared to the beam in front

¹³Strictly speaking, only a mono-modal waveguide acts as a perfect coherence filter. However, numerical simulations of the coupling process show that even for a waveguide with three modes, coherence is already significantly filtered.

of the pre-focusing optics. A higher coherent flux and thus a higher gain in flux density is expected for less 'conservative' waveguide systems as used in the presented experiments (for example: using a photon energy $E = 17.5$ keV at the beamline ID22 NI, the length of the 18 nm C waveguide can be reduced to 600 μm). On the other hand, the experiments and simulations show that the gain in flux density cannot be enhanced by pre-focusing optics with higher angular acceptance as the transmission of the waveguide significantly decreases with increasing convergence angle of the incident focused beam.

4.3 Two crossed waveguides

In this section we demonstrate direct coupling of a pre-focused beam into a two crossed waveguide. The optimized waveguide length of each waveguide slice results in a highly confined beam in two dimensions. The near-field of the obtained secondary source is reconstructed from the far-field measurements using an iterative algorithm.

4.3.1 Experimental setup ID22-NI beamline, ESRF

The experiment was carried out at the ID22-NI undulator beamline of the ESRF. Two undulators were used simultaneously, working at the second and fifth harmonic, respectively. The radiation was used in the so-called pink mode (no crystal monochromators) at a photon energy of $E = 17.5$ keV, taking advantage of the intrinsic monochromaticity of the undulators and the bandpass of the multi-layer KB mirror system, resulting in $\Delta\lambda/\lambda \approx 0.016$. In addition, a flat horizontally deflecting Pd-coated Si mirror was used at 0.15 degree incidence angle for higher harmonic rejection. The focus of the KB mirrors was characterized by translation of an Au stripe, recording both the transmitted intensity by a diode and the AuL_α fluorescence by a silicon drift detector (Vortex-EX, SII NanoTechnology Inc.). The measured focal spot size was $D_{\text{horz}} = 129$ nm (FWHM of fluorescence intensity) in the horizontal and $D_{\text{vert}} = 166$ nm (FWHM of fluorescence intensity) in the vertical direction, respectively. The total intensity in the focal spot was on the order of 10^{11} ph/s, depending on the ring current and the slit settings in front of the KB. A low noise direct photon counting pixel detector (Maxipix, ESRF [93]) with a pixel size of 55 μm and an active area of 256×256 pixels was used to measure the far-field pattern at a distance of 3.09 m from the waveguide.

4.3.2 Waveguide alignment

The waveguide system consists of two planar waveguide slices, each with a guiding layer thickness $d = 35$ nm, in a crossed geometry. The first horizontal com-

ponent (planar waveguide-1) with length $l_1 = 400 \mu\text{m}$ and the second vertical component (planar waveguide-2) with a length $l_2 = 207 \mu\text{m}$ are glued on each other (see section 3.8). The two crossed waveguide was aligned in terms of three translations and two rotations (Attocube Systems, Germany) in the focal plane of the KB. We first aligned each waveguide slice separately resulting in a first guess of the x and y positions (perpendicular to the propagation direction z) and the incident angles (around the x and y axis) for alignment of the two crossed waveguide. The alignment of the waveguide was facilitated by the fact, that only the combined thickness of the waveguide slices $l_1 + l_2$ is thick enough to block completely the incoming beam. Hence, the photon flux exiting the aligned horizontal planar waveguide and propagating through the vertical slice even not perfectly aligned was measurable. Finally, an iterative procedure of translation and rotation measurements enabled the alignment of the two crossed waveguide.

4.3.3 Transmission

The total flux exiting the waveguide was $6.4 \cdot 10^8$ ph/s as measured by a single photon counting diode (integrated far-field intensity). The intensity of the KB beam used as reference value was $2.7 \cdot 10^{11}$ ph/s. The corresponding transmission of the two crossed waveguide $T_{\text{exp}} = 0.052$ is significantly lower than the value of $T_{\text{sim}} = 0.916$ obtained by simulation assuming plane wave illumination under normal incidence angle. As presented in section 4.2.1, the effect of partial coherence and the convergence angle of the beam must be taken into account. First, we calculate the degree of coherence in front of the KB. In the vertical direction, the source size $\sigma_{\text{vert}} = 30 \mu\text{m}$, the source divergence $\sigma'_{\text{vert}} = 5 \mu\text{rad}$ and the 63 m distance from the undulator yield a degree of coherence of 0.18 at the source. Cutting the beam size by the $400 \mu\text{m}$ vertical slit size in front of the KB, the degree of coherence of the beam illuminating the KB increases to 0.33. In the horizontal direction, on the other hand, a virtual source realized by a $10 \mu\text{m}$ slit at a distance of 27 m downstream from the undulator, provides a nearly completely coherent beam over the $190 \mu\text{m}$ horizontal KB slit size. Thus in front of the KB, as in its focus, about 33% of the flux is coherent. Since the waveguide essentially accepts only the coherent flux, a factor of three in the discrepancy can thus be attributed to partial coherence. The highly confined KB beam of the ID22 NI setup yields a convergence angle of 0.10° and 0.08° in horizontal and vertical direction, respectively, as determined from the measured KB far-field (Fig. 4.16). Taking the effect of partial coherence and the convergence angles into account, the calculated transmission reduces to $T_{\text{calc}} \approx 0.229$.

The remaining factor of about 4-5 must be due to other factor(s). The most likely reason is the finite depth of focus (DOF), which must be compared to the

thickness of the waveguide slices. If, for example, the first vertically oriented slice (planar waveguide-1) was exactly in the focus, the entrance of the second slice (planar waveguide-2) would already be displaced by $400\ \mu\text{m}$, corresponding to the thickness of planar waveguide-1. We estimate the depth of focus by $DOF \leq 2z_R$, where $z_R = k\sigma_{\text{KB}}^2$ is the Rayleigh length, k the wavenumber, and σ_{KB} the lateral width of the focus, to $DOF_{\text{vert}} = 440\ \mu\text{m}$ and $DOF_{\text{horz}} = 266\ \mu\text{m}$, for the two directions, respectively. Since the DOF is likely to be smaller for a partially coherent beam (see coherence factor above), this may very well account for the 4-5 fold intensity ratio not explained by the coherence argument. Note that the equality in the expression for the DOF holds only in the limit of full coherence.

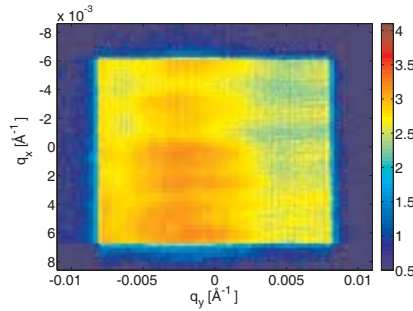


Figure 4.16: KB mirror far-field as a function of the reciprocal coordinates q_x and q_y . The intensity is encoded logarithmically in the colormap.

4.3.4 Far-field pattern

Fig. 4.17 (a) shows the measured far-field pattern of the two crossed waveguide as a function of the two reciprocal space coordinates q_x and q_y after combination of 15 accumulations (exposure time 2 s each) with the detector shifted in the xy -plane to increase the field of view. A relatively uniform and flat intensity distribution in the center is framed by a characteristic arrangement of vertical and horizontal fringes. We attribute the fringes to interference of the wave ψ_{xy} guided by both planar waveguide slices, with the wave components $\psi_x t_y$ and $\psi_y t_x$. The latter terms denote the waves guided only by one of the planar waveguide slices and attenuated by the other, with simultaneous diffraction from its planar interfaces. Fig. 4.17 (b) shows a two-dimensional representation of the simulated planar waveguide-1 and planar waveguide-2 far-field, obtained by multiplication of the respective simulations of planar waveguide slices. The simulation is based on the finite-difference algorithm to obtain the simulated

electromagnetic field distribution of the propagating modes inside the planar waveguides and the near-field distributions. The far-fields are obtained by a fast Fourier transformation (FFT) of the near-field distribution. The simulation does not account for the simultaneous diffraction at the planar interfaces of the planar waveguides but illustrates the form of the far-field around the maximum intensity. As mentioned above, only the combined thickness of the two crossed slices $l_1 + l_2$ is thick enough to completely block the beam, while a single slice exhibits measurable transmitted photon flux. At the same time, the finite planar waveguide contributions do not impede holographic imaging, as shown in chapter 5.

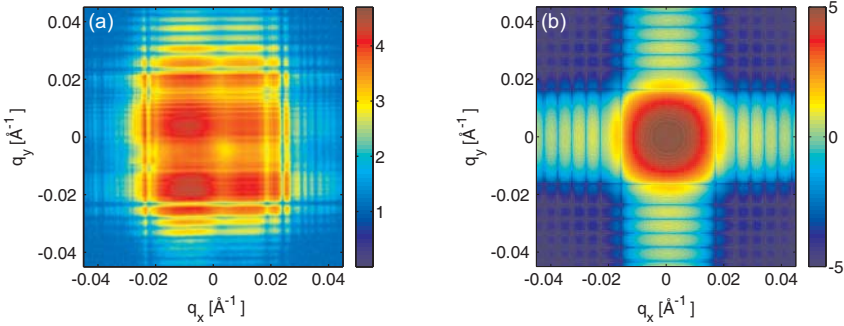


Figure 4.17: (a) and (b) Measured and simulated far-field pattern of the two crossed waveguide, the intensity is encoded logarithmically in the colormap (I [cps] and I [arb. units], respectively).

4.3.5 Near-field reconstruction

To corroborate this and to further characterize the near-field distribution in amplitude and phase, we have adapted an inverse scattering approach, where the near-field is reconstructed iteratively from the measured far-field pattern by use of the error-reduction (ER) algorithm [34], introduced in section 1.5.2:

$$\psi(x, y) = \lim_{N_{\text{it}} \rightarrow \infty} (\mathcal{P}'_1 \mathcal{F}^{-1} \mathcal{P}_2 \mathcal{F})^{N_{\text{it}}} \psi_{N_{\text{it}}=0}(x, y), \quad (4.7)$$

where the real-space constraint is given by

$$\mathcal{P}'_1 \psi(x, y) = \begin{cases} \psi(x, y), & (x, y) \in \mathcal{S}, \\ 0, & \text{otherwise.} \end{cases} \quad (4.8)$$

By application of a support constraint in the exit plane of the two crossed waveguide with a cross section of $\mathcal{S} = 150 \times 150 \text{ nm}^2$ (smoothed by an error function),

the near-field intensity in a virtual plane behind the two crossed waveguide can be retrieved iteratively in intensity and phase. Fig. 4.18 (b) shows the reconstructed near-field intensity, obtained after $N_{\text{it}} = 1000$ iterations and an initial guess of a Gaussian amplitude with FWHM = 35 nm. The reconstruction for $N_{\text{it}} = 1000$ did not show any significant differences with respect to shorter and longer runs, e.g. $N_{\text{it}} = 10$ or $N_{\text{it}} = 10000$, underlining the rapid convergence. The ER reconstruction always yields a flat exit wavefront (no curvature). The reconstructed near-field must thus be associated with a virtual plane which can be considered as the effective confocal plane of the two crossed waveguide. The high beam confinement is also in agreement with the autocorrelation function of the field at the exit surface of the two crossed waveguide calculated as the modulus of the FFT applied to the measured far-field intensity. The beam confinement in both directions due to the 2D waveguide effect is clearly evidenced by the center maximum, visible in Fig. 4.18 (a). The nearly isotropic shape indicates that the two crossed waveguide-source can be described as quasi point-like. The full width of the autocorrelation function (FWHM) obtained by Gaussian fits was 14.2 nm and 17.9 nm for the vertical and horizontal direction, respectively. Note that for the calculations the far-field is placed in a 5 times larger grid filled with zeros to obtain sufficiently sampled reconstructions.

Next, we have compared the reconstructed near-field distribution to finite-difference simulations of the planar waveguide slices. A waveguide with a 35 nm C guiding layer supports three modes, leading to a periodically alternating field distribution by interference of the modes (mode beating), as shown in Fig. 4.18 (c) for a closeup of a 17.5 keV simulation (see also section 2.4.3). A Fourier transformation of the field with respect to the propagation direction z decomposes the simulated electromagnetic field into the guided modes which are shown in Fig. 4.18 (d). Δk corresponds to the difference between the respective propagation constants β_m and the wavenumber k in free space. In Fig. 4.18 (d) only the ψ_0 and the ψ_2 modes are visible, the ψ_1 mode is not excited by a plane wave impinging on the waveguide at normal incidence due to symmetry. The observed difference $\beta_0 - \beta_2 = 2.28 \cdot 10^{-4} \text{ nm}^{-1}$ is in excellent agreement with the analytical result. Due to the periodically alternating field, a corresponding oscillating confinement of the fields depending on the propagation distance is obtained, as illustrated by dashed lines in Fig. 4.18 (c), and the corresponding near-field profiles in Fig. 4.18 (e). Thus, the exit wave field will depend on the exact length of the WG slice. The FWHM (full width at half maximum) of the simulated near-field intensity Δ_x [nm] and the corresponding far-field intensity Δ_q [\AA^{-1}] as a function of the waveguide length l are plotted in Fig. 4.18 (f). Finally, Fig. 4.18 (g) and (h) show the comparison of the FD simulation and the ER reconstructions for the vertical and horizontal direction, respectively. The width (FWHM) of the Gaussian fit to the near-field intensity distributions obtained by

ER reconstruction is 9.2 nm and 9.6 nm, compared to 12.5 nm and 13.6 nm of the FD simulation, for the vertical and horizontal direction, respectively.

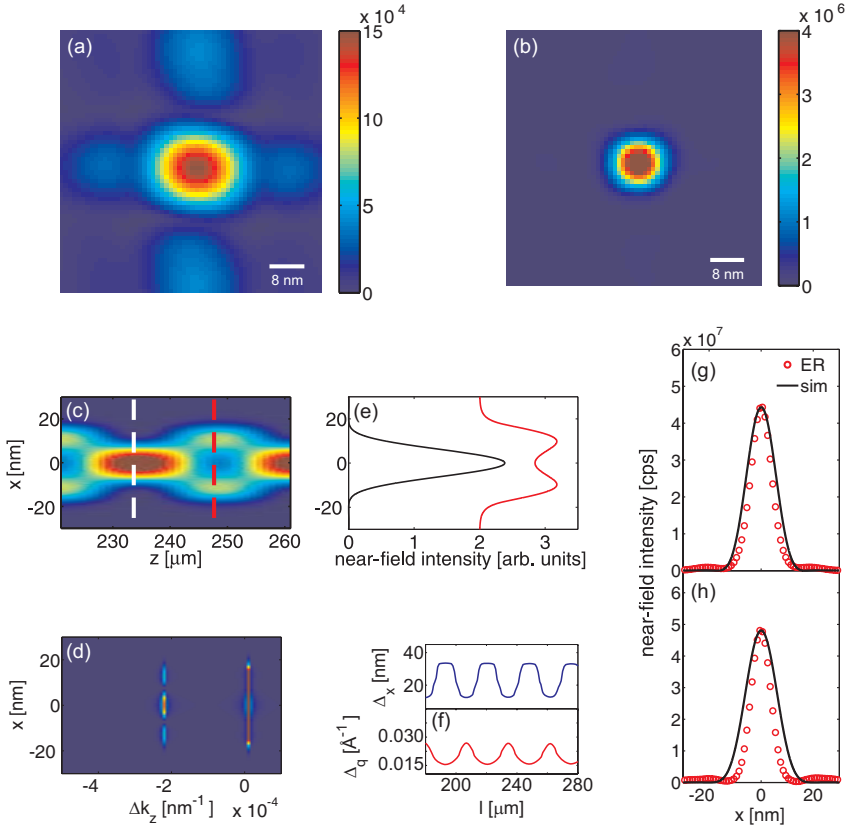


Figure 4.18: (a) Autocorrelation of the measured far-field distribution shown in Fig. 4.17. (b) Reconstructed near-field intensity obtained from the ER algorithm. (c) Simulated electromagnetic field intensity inside the planar waveguide at $E = 17.5$ keV within a range of 221 – 261 μm in propagation direction z . (d) Fourier transformation with respect to z of the simulated electromagnetic field in the planar waveguide showing the modes ψ_0 (right) and ψ_2 (left). (e) Field intensities which correspond to the dashed lines in subfigure (c) illustrating the mode beating. (g) and (j) Reconstructed intensity along with the simulated near-field intensity of the planar waveguide-1 and planar waveguide-2.

4.3.6 Conclusions

The formation of a two-dimensional waveguide quasi-point source has been demonstrated by combination of two crossed planar waveguide structures, in a compact geometry, with the horizontal and vertical focus coinciding within 207 μm . A total flux in the waveguide beam of $6.4 \cdot 10^8$ ph/s was achieved by focusing a KB beam into the front face of the waveguide. From measurements of the far-field diffraction pattern, the phase and amplitude of the near-field distribution is retrieved using the error-reduction algorithm. In agreement with FD field simulations (forward calculation), the reconstructed exit wave intensity distribution (inverse calculation) exhibits a FWHM below 15 nm in both dimensions, i.e. below the focal spot size of other focusing optics currently achieved in the hard x-ray energy range. The crossed waveguide device is used for holographic imaging as shown in chapter 5.

4.4 Waveguide setup for new holography endstation

We present first results of Ge/Mo/C/Mo/Ge waveguide measurements obtained at the new holography endstation [85] of the P10 coherence beamline, Petra III (Hamburg, Germany). The holography endstation is dedicated inter alia to waveguide-based imaging experiments.

4.4.1 P10 beamline: experiments and results

The P10 coherence beamline is currently under construction. In the experimental setup used for the experiments the x-ray beam of the undulator is defined by a double crystal Si(111) monochromator (mirrors will be installed later on). The holography endstation [85] uses Pd coated silicon and Pd coated silica KB mirrors for vertically and horizontally focusing, respectively. As presented in [94], the focal spot size was minimal $D_{\text{horz}} = 203$ nm in the horizontal and $D_{\text{vert}} = 221$ nm in the vertical direction, respectively, at a photon energy of $E = 7.9$ keV. The intensity in the focal spot of the KB beam was $2 \cdot 10^{11}$ ph/s. The waveguide was positioned in the focal spot of the KB system using a goniometer mounted upside down on a vibration-reduced extension arm with three miniaturized translations and two miniaturized rotations (Attocube Systems, Germany), along two directions, orthogonal to the optical axis. An additional translation below the rotation was used to select the whole range of the waveguide along its guiding layer. A more detailed description of the endstation setup can be found in [85]. A noise-free single-photon counting detector (Pilatus, SLS [95]) with a pixel size of 172 μm and an active area of 487×619 pixels was used to measure the far-field pattern at a distance of 5.15 m from the waveguide.

First measured far-fields of a planar 35 nm C waveguide and a two crossed 35 nm C waveguide with waveguide slice thicknesses of 200 μm each are presented in Fig. 4.19. Fig. 4.19 (a) shows the characteristic far-field pattern of a horizontally placed planar waveguide with polished entrance and exit faces. The total photon flux exiting the waveguide was approx. $6 \cdot 10^7$ ph/s.

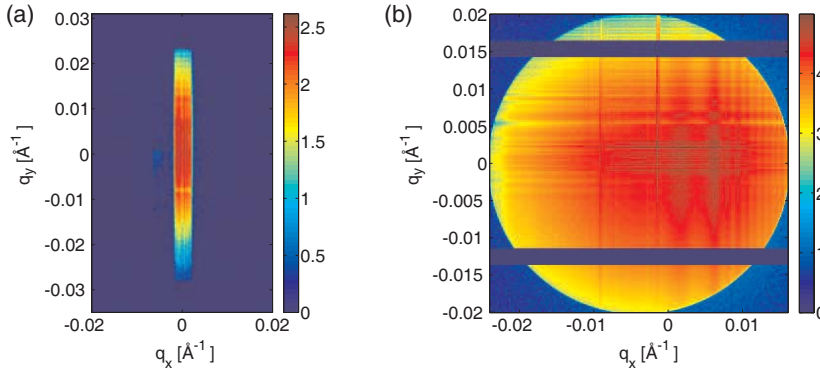


Figure 4.19: (a) Far-field pattern of the 35 nm C planar waveguide as a function of q_x and q_y (rotated by 90° , exposure time 0.1 s). (b) Far-field pattern of the 35 nm C two crossed waveguide as a function of q_x and q_y (exposure time 500 s). The image is altered by the presence of the optical in-line microscope (circular lens) accidentally remaining in the optical path during exposure and the flight tube (bars top and down) whose diameter was chosen to small. The intensity [cts] of the diffraction pattern is encoded logarithmically in the colormap.

The measured spot size of the KB in vertical direction was $D_{\text{vert}} = 382$ nm in the actual experimental configuration, as measured by translation of the waveguide beam through focal plane. The corresponding transmission of the waveguide is $T_{\text{exp}} = 0.003$. The simulated transmission is $T_{\text{sim}} = 0.574$ assuming plane wave illumination. The large discrepancy between T_{exp} and T_{sim} cannot be explained even by taking the angle of convergence of the KB in vertical direction (0.11° [94]) and the partial coherence of the synchrotron beam into account. The problem of low transmission values has to be addressed in the following experiments.

The alignment of the two crossed waveguide was difficult and we are not yet sure if we succeeded. The shape of the diffraction pattern shown in Fig. 4.19 (b) is similar to the far-field pattern presented in Fig. 4.17 (b) exhibiting the high divergence of the waveguide source. However the total flux exiting the two

crossed waveguide was rather low, i.e., we needed a particular long exposure time of 500 s to record the shown far-field pattern on the 2D detector.

In future experiments, we will address the problem of low two-dimensional waveguide beam intensity at the holographic endstation and further focus on the angular acceptance as well as on the transmission of two-component waveguides with different layer systems.

4.5 Conclusions

An extended study of planar waveguide with an optimized cladding design has been presented (section 4.1). The experiments show that short waveguide length combined with efficient blocking of radiative modes enable small beam sizes at the waveguide exit along with high transmission values of the spatially and coherently filtered synchrotron beam. The use of pre-focusing optics resulted in a quite high gain of flux density of the primary beams (section 4.2). Simulations taking the divergence and the coherence properties of the pre-focusing beams into account have to be developed to further understand the far-field properties of the waveguides. The experiment with the compact two-crossed waveguide demonstrated the formation of a quasi point-like source of sub-15 nm beam confinement in both lateral dimension (section 4.3). The effective near-field distribution was determined by reconstructing the waveguide exit wave-field from the measured far-field by using an error-reduction algorithm. A total flux of $6 \cdot 10^8$ ph/s exited the two-crossed waveguide making this waveguide optics suitable for high resolution x-ray imaging. Finally, the novel holography endstation dedicated to waveguide-based imaging and first results of waveguide characterization at the P10 beamline are presented (section 4.4).

5 Experiments II: Phase contrast imaging

This chapter describes lensless x-ray imaging of well-defined test pattern (section 5.1) and unstained biological cells (section 5.2) using the in-line holography geometry¹⁴. We carried out the experiments using two-crossed waveguide and planar waveguide as highly confining optical elements presented in chapter 4. Measured holograms are reconstructed in the effective parallel beam geometry. Two types of reconstruction algorithms are used. Holographic reconstruction allowing for fast and deterministic reconstructions on one hand, and iterative algorithms allowing for optimized phase recovery on the other hand. Iterative reconstructions take advantage of the fact, that the investigated samples essentially act as pure phase object in the hard x-ray energy range.

5.1 Imaging of test pattern

Waveguide-based x-ray imaging experiments on test pattern with well-defined spatial frequencies are performed. Special emphasis is put on the effect of non-transferred spatial frequencies in holographically and iteratively reconstructed holograms. Spatial resolution of phase reconstructions are determined. Resolution limits depending on the waveguide properties and additional constraints in the experimental setup are discussed.

5.1.1 Layout of the test pattern

The high resolution chart (NTT-AT, Japan; model # ATN/XRESO-50HC) consist of a 500 nm thick nanostructured tantalum layer on a Ru/SiC/SiN membrane fabricated using electron beam lithography. The thickness of the individual membrane layers are 20 nm (Ru), 200 nm (SiC) and 50 nm (SiN), respectively. The membrane is fixed on Si holder of size $10 \times 10 \times 1 \text{ mm}^3$ with a hole of $1 \times 1 \text{ mm}^3$ in the center where the nanostructured pattern area of size $300 \times 300 \mu\text{m}^2$ is placed.

Different structures are placed on the test pattern as shown in Fig. 5.1 (a). We used the Siemens star pattern, the grid pattern with $1 \mu\text{m}$ pitch and the 50 nm lines-and-spaces (LS) pattern for imaging applications. Scanning electron images (SEM: Leo Supra 135, Zeiss NTS) of the radial pattern with a minimum pattern size of 50 nm and the 50 nm LS pattern are shown in Fig. 5.1 (b), recorded with a magnification factor of 6 kx and 40 kx, respectively. Note that in contrast to the Siemens star design used for simulation (see chapter 1) the radial stripes diverging from the center are separated into rings of defined spatial period at the innermost radius.

¹⁴Contents of this chapter have been published in [47] and [11].

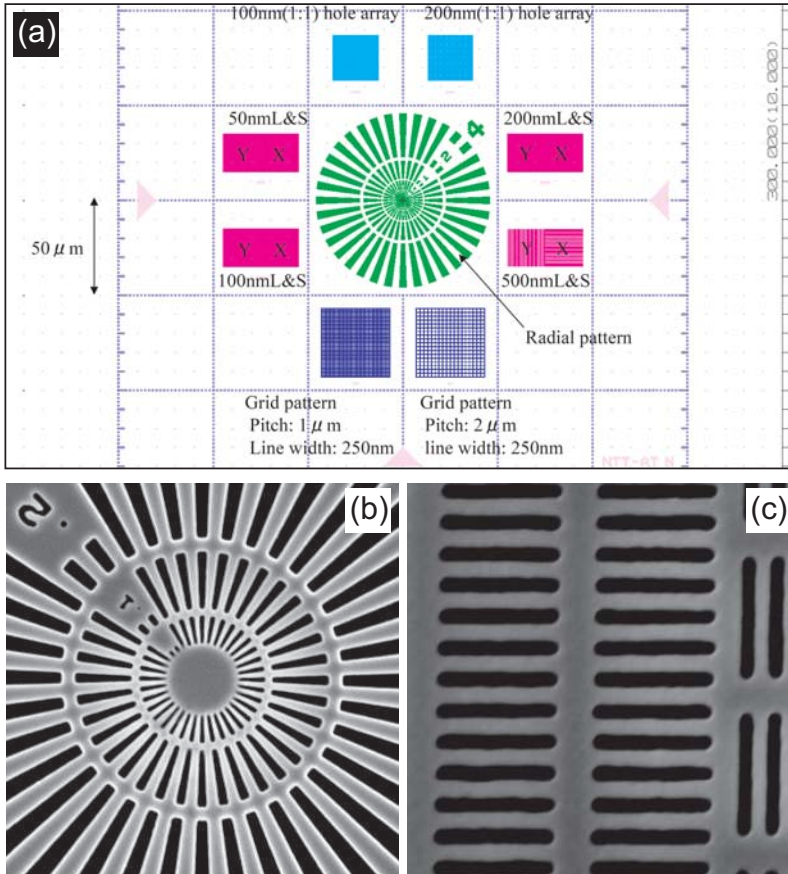


Figure 5.1: (a) Layout of the NTT-AT test pattern [96]. We used the Siemens star pattern (center), the grid pattern with $1\ \mu\text{m}$ pitch (bottom left) and the 50 nm lines-and-spaces (LS) pattern (left, on the top) for the waveguide-based imaging experiments. (b) Scanning electron image showing the central region of the Siemens star pattern. The radial stripes diverging from the center are separated into rings of defined spatial period at the innermost radius (50 nm line width at the beginning of the central (first) ring, 100 nm line width at the beginning of the second ring, 200 nm at the third ring). (c) Scanning electron image showing part of the 50 nm LS pattern. The LS pattern has a half-period of 50 nm as measured by the scanning electron microscope. SEM parameters: (b) accelerating voltage EHT = 10 kV, working distance WD = 4.5 mm, magnification mag = 6 kx; (c) EHT = 10 kV, WD = 4.5 mm, mag = 40 kx;

5.1.2 Holographic imaging: Siemens star

The imaging experiments were carried out using the setup and the experimental settings presented in section 4.3.1. The test pattern was placed on microstep translation stages (Micos GmbH, Eschbach, Germany) for translations of the sample in x , y and z direction and equipped with an additional piezo positioning stage (Princeton Instruments, Germany) for more precise translations in the yz -plane. The distance z_1 between the two crossed waveguides (placed in the focal plane of the KB) and the sample was determined optically with a microscope coaxial with the optical axis (Accel, Germany). The Maxipix detector was placed at a distance z_2 from the sample.

For holographic imaging of the Siemens star the sample was placed at a distance $z_1 = 4.48$ mm downstream from the waveguide and the in-line holograms were imaged at a distance $z_2 = 3.09$ m from the sample. The Siemens star was mapped by translation in the xy -plane as illustrated in Fig. 5.2 (a). Mapping allows to image an extended sample on a larger region, i.e. to increase the field of view. The defocus position of $z_1 = 4.48$ mm correspond to a beam size of $6.72 \mu\text{m}$ (intensity FWHM) at the sample.

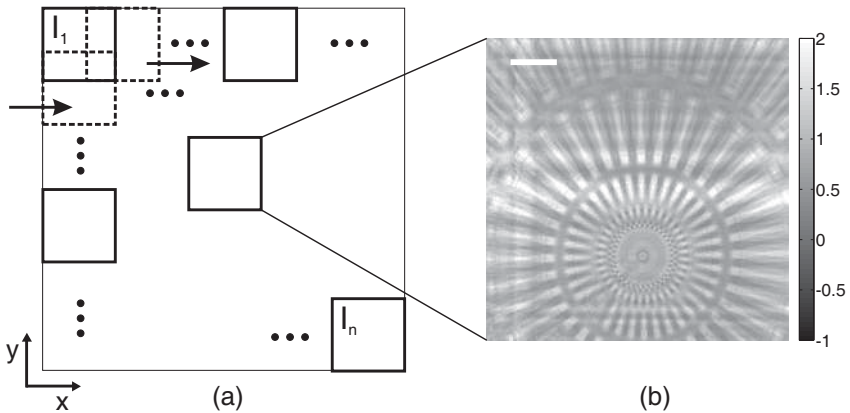


Figure 5.2: (a) Schematic illustrating the mapping of the Siemens star by translation in the xy -plane. A mesh of 15×15 scan points was recorded. (b) Measured single hologram of the Siemens star pattern corresponding to scan point 56 of the 225 total scan points and normalized by the mean far-field pattern of the waveguide beam. Scale bar indicate 2 mm (coordinate system in the detector plane). The normalized intensity is encoded in the colormap.

A mesh of 15×15 scan points was recorded with an exposure time of 2 s for each recording. After the mesh, the sample was removed from the optical path and 10 accumulations of the waveguide far-field pattern each of 2 s exposure time were recorded (without shifting the detector). Out of the 10 accumulations the mean intensity distribution I_m of the waveguide far-field pattern was calculated. A single hologram corresponding to the scan point 56 of the 225 total scan points recorded is shown as an example in Fig. 5.2 (b). The hologram is normalized by the mean waveguide far-field intensity I_m . The structure of the Siemens star can already be recognized, especially the low frequency features. The resemblance to the object gets more and more lost towards the center of the Siemens star (high frequency features). The normalized hologram exhibit some artifacts in horizontal direction (center region) and vertical direction (left region) due to fluctuations and long-term drift in the waveguide exit wave-field. These artifacts can be minimized by recording the waveguide far-field pattern after each scan point of the sample mesh and then normalizing each hologram by the respective (subsequently recorded) waveguide far-field pattern. Note that short time delays on the order of a second in between sample and empty exposures are enabled by the fast piezo sample stage and the short readout time of the detector.

At the photon energy $E = 17.5$ keV used in the experiment, the expected phase shift of the 500 nm thick Ta pattern is $\phi = 0.40$ rad, and the (intensity) transmission is $T = 0.93$. The expected phase shift and the absorption of the Ru/SiC/SiN membrane is comparably low (phase shift of $\phi = 0.06$ rad and absorption of $A = 8.3 \cdot 10^{-4}$). Phase shifts of individual parts (membrane and Ta structure) of the test pattern are summed up. Since the membrane is extended over the whole region of the pattern we expect only an additional offset in phase reconstruction of the sample. Transmission of individual parts of the test pattern are multiplicative. Since the transmission of the membrane is $T \approx 1$ we expect no effects of the membrane in reconstruction.

The total photon flux measured on the detector was $4.0 \cdot 10^7$ ph/s (field of view in the sample plane: 1.72×1.72 mm²) for the single hologram (scan point 56). The intensity is lower than the total photon flux of the perfectly aligned waveguide of $6.4 \cdot 10^8$ ph/s as measured by a diode. Besides the drift effect of the waveguide, the lower photon count is due to the limited field of view of the detector compared to waveguide divergence, i.e. not the full waveguide beam intensity is recorded. Note that the photon flux losses due to absorption by the test pattern can be neglected. The mean photon count per pixel is ca. 10^3 ph/s and lowest photon count per pixel is 40 ph/s indicating that high image resolution in reconstruction is in principle not adulterated by signal-to-noise ratio [19]. Noise limited resolution is assumed for intensities below $I(x, y) = 25$ photon counts (Rose criterion [97] for the signal-to-noise ratio in case of Poisson noise: $I(x, y) / \sqrt{I(x, y)} \geq 5$).

Fig. 5.3 shows the power spectrum of the hologram as a function of the resolution $d(q) = 1/\nu$ where $\nu = q/(2\pi)$ denotes the spatial frequencies present in the power spectrum. The power spectrum is calculated by radially integrated and averaged Fourier transform of the diffraction pattern windowed by a Hann window function to account for aliasing by use of the discrete Fourier transform (DFT), i.e. allowing for 'perfect' periodic extension at the image 'edges' for the DFT [98]. The highest frequency present (Nyquist rate, see appendix B) corresponding to $d = 160$ nm (cut-off in the power spectrum) is limited by the detector pixel size.

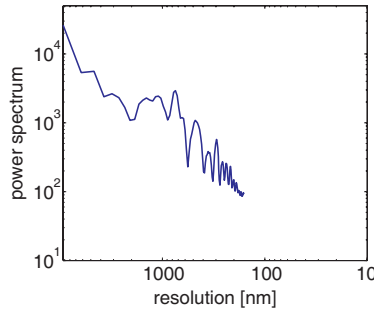


Figure 5.3: Power spectrum of the windowed diffraction pattern (scan point 56) as a function of the resolution $d(q) = 2\pi/q$. The minimal resolution is rather limited by the detector pixel size than by the signal-to-noise ratio.

5.1.3 Holographic reconstruction: Siemens star

For holographic reconstruction the projection geometry used here was mapped onto parallel beam propagation by a variable transformation based on the Fresnel scaling theorem introduced in section 1.4. Given the distance z_1 between source and sample and z_2 between sample and detector, parallel beam reconstruction by Fresnel backpropagation of the recorded intensity can be applied using the effective defocus (propagation) $z_{\text{eff}} = z_1 z_2 / (z_1 + z_2) = 4.47$ mm. At the same time the hologram is magnified corresponding to the geometrical projection by a factor of $M = (z_1 + z_2) / z_1 = 690$. The Siemens star is reconstructed by applying the free-space diffraction operator $\mathcal{D}_{-z_{\text{eff}}}$ on each measured hologram $I(x, y)$

$$\psi(x, y) = \mathcal{D}_{-z_{\text{eff}}} I(x, y). \quad (5.1)$$

For the experimental parameters relevant in this work, the hologram is dominated by the phase shift in the sample, rather than by absorption (amplitude).

We thus focus the attention on $\phi(x, y)$ of $\psi(x, y) = A(x, y) \exp [i\phi(x, y)]$. We stress, however, that the analysis presented here is valid in the general case, and can in fact be used on experimental data to determine the relative weight of the absorption and phase contrast.

Fig. 5.4 shows the image reconstruction after combining 15×15 scan points in real space and a line scan through the phase distribution of the reconstructed image near the center of the Siemens star. Each hologram was reconstructed from the intensity in the center of the far-field, corresponding to $|q_x|, |q_y| \leq 0.0035 \text{ \AA}^{-1}$ (roughly 1/10 of the region covered by the detector). The raw images were regridded by a factor of 2 for the image reconstruction and by a factor of 16 in the linescan¹⁵. The image resolution was determined from a fit of phase step to an error function using

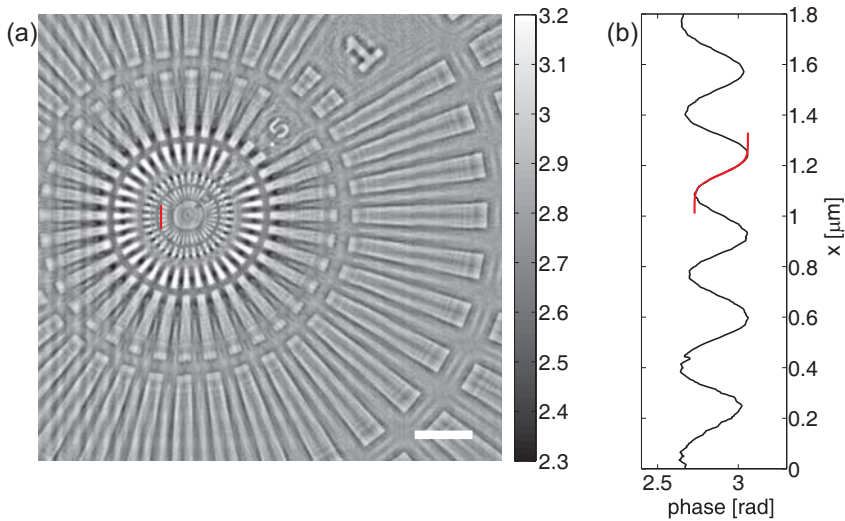


Figure 5.4: (a) Holographic reconstruction of the Siemens star test pattern after combination of 15×15 scan points. Scale bar and colorbar indicate $4 \mu\text{m}$ and phase in [rad], respectively. (b) Line scan through the phase distribution indicated by the vertical red line in subfigure (a) along with a fit of a Gaussian error function to a single phase step yielding a width (FWHM) of 87 nm (image resolution).

¹⁵Regridding is performed using the cubic spline interpolation method (matlab routine *interp2.m*) [99].

$$f(x) = A \operatorname{erf} \left(\frac{x - x_0}{\sqrt{2}\sigma} \right) + B, \quad (5.2)$$

where the error function is given by

$$\operatorname{erf} = \frac{2}{\sqrt{\pi}} \int_0^x \exp(-t^2) dt. \quad (5.3)$$

The fit yields a width (FWHM) of 87 nm (FWHM = $2\sqrt{2\ln 2}\sigma$). Note that the magnification $M = 690$ for the given defocus corresponds to an image pixel size of 80 nm (before regridding).

The overall structure of the test pattern is recovered up to very fine details in the center region. However, the highest obtained resolution of 87 nm is significantly above the reconstructed near-field width of the waveguide beam of sub-15 nm. In fact, the resolution is rather limited by the low magnification factor M (high defocus z_1). Due to steric constraints in the setup, z_1 smaller than 4.47 mm and thus possibly higher resolution imaging could not be tested. In section 5.1.6 we discuss the resolution limit for the same experimental settings except the values of z_1 and z_2 .

The retrieved phase values are only in coarse agreement with the expected phase shift of 0.4 rad between the void areas (high phase values) and the Ta structure (lower, retarded phase values). Further, holographic reconstruction shows artifacts (in particular twin-image artifacts, noise effects are successfully reduced by scanning procedure) and non-reconstructed spatial frequencies which are due to the non-uniform phase contrast transfer function (see below). Artifacts and poor phase recovery can partly be overcome using iterative reconstruction algorithms as presented in section 5.1.4.

Fig. 5.5 (a) shows the two-dimensional representation of the phase contrast transfer function $\text{PCTF} = \sin \chi$ (with $\chi = (\lambda z / 4\pi)(k_x^2 + k_y^2)$, see also section 1.3). We used the same parameters λ , k_x and k_y as for reconstruction of the experimental data. The white dotted circles indicate the first two zeros of the PCTF. Fig. 5.5 (b) shows the Fourier transform of the measured hologram indicating the spatial frequencies of the object which are not transferred. Although the test pattern is not a pure phase object ($T = 0.93$ at $E = 17.5$ keV) the non-transferred spatial frequencies correspond in good approximation to the zeros of the PCTF (the white dotted circles in subfigure (b) have the same radii as the circles shown in subfigure (a)). Minima related to zeros of the amplitude contrast transfer function $\text{ACTF} = \cos \chi$ are not observed. Fig. 5.5 (c) shows the holographically reconstructed Siemens star. The non-reconstructed spatial frequencies of the Siemens star, indicated by a red dotted circle, again reflects the effect related to the CTF.

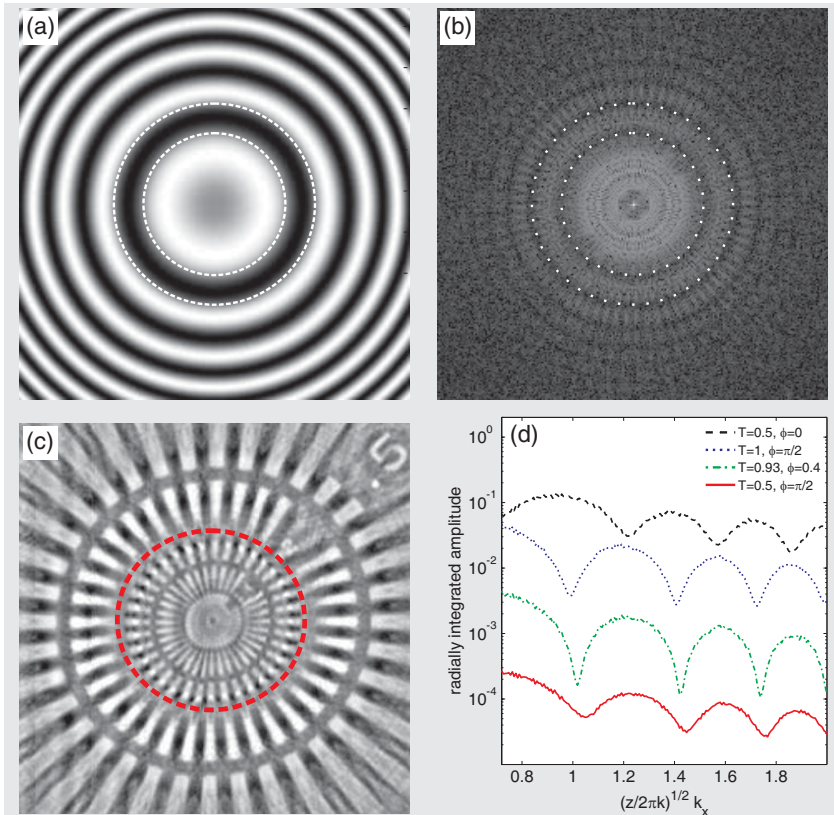


Figure 5.5: (a) Phase contrast transfer function (PCTF), calculated for the parameters corresponding to the experimental settings. The white dotted circles indicate the first two zeros of the PCTF. (b) Fourier transform of the measured Siemens star hologram, along with white dotted circles corresponding to the zeros of the PCTF in subfigure (a). (c) Holographic reconstruction of the Siemens star, along with red dotted circle indicating the region of lack of spatial information due to the zero of the PCTF. (d) Fourier transform of the propagated Siemens star (simulation), radially integrated, for a pure amplitude object ($T = 0.5$), a pure phase object ($\phi = \pi/2$), an object with $T = 0.93$ and $\phi = 0.4$ and an object with $T = 0.5$ and $\phi = \pi/2$. The curves are shifted for clarity. The minima of the curves corresponding to objects with $T < 1$, $\phi > 0$ are slightly shifted compared to the pure phase object curve.

To quantify the effect of the CTF on the reconstructed image we have determined the radius $r = 3.3 \pm 0.2 \text{ } \mu\text{m}$ corresponding to the non-reconstructed spatial frequency. Using the relation $k_x = 2\pi/r$ we obtain $\sin \chi = (1.7 \pm 0.1) \cdot 10^{-7}$ (one-dimensional PCTF). Thus, the non-reconstructed spatial frequency is in excellent agreement with the zero of the PCTF ($\sin \chi = 0$).

To further investigate the dependance of transmission and phase shift properties of an object on non-transferred spatial frequencies we have performed Siemens star simulations. Fig. 5.5 (d) shows radially integrated Fourier transform (amplitude) of simulated holograms (propagated Siemens star) as a function of the normalized Fourier component $\sqrt{z/2\pi k} k_x$. The minima of a pure amplitude object and a pure phase object correspond to the zeros of $|\text{ACTF}|$ and $|\text{PCTF}|$, respectively. The curve corresponding to the object simulated for $T = 0.93$ and $\phi = 0.4 \text{ rad}$ is slightly shifted compared to the pure phase object curve. Interestingly, an object of comparably high absorption $T = 0.5$ and of high phase shift $\phi = \pi/2 \text{ rad}$ shows minima close to the zeros of the PCTF. Thus, the phase shifting property of an object is dominant compared to its absorption property in terms of non-transferred spatial frequencies.

5.1.4 Iterative reconstruction: Siemens star

Next, we consider a full-field hologram of the Siemens star taken at a distance $z_1 = 7.48 \text{ mm}$ and normalized by the waveguide far-field pattern as shown in Fig. 5.6 (a). The total photon flux measured on the detector was $7.6 \cdot 10^7 \text{ ph/s}$. Note that, in contrast to the hologram shown in Fig. 5.2 (b), artifacts due to the waveguide exit beam fluctuations are not observed as the waveguide far-field pattern was subsequently recorded after imaging the test pattern.

The phase reconstruction using the holographic reconstruction is shown in Fig. 5.6 (b). The iterative reconstruction of the test pattern is carried out using the GS algorithm

$$\psi(x, y) = \lim_{n \rightarrow \infty} (\mathcal{P}_1 \mathcal{D}_{-z_{\text{eff}}} \mathcal{P}_2 \mathcal{D}_{z_{\text{eff}}})^{N_{\text{it}}} \psi_{N_{\text{it}}=0}(x, y). \quad (5.4)$$

The theoretical amplitude transmission of the Ta structure is $T = 0.96$ which is close to one. Approximating the overall transmission to $T = 1$, the real-space constraint is expressed by

$$\mathcal{P}_1 |\psi(x, y)| = 1. \quad (5.5)$$

To prevent possible overfitting of the noise in the diffraction data, the stop criterion presented in [11] is introduced in the algorithm. The algorithm stops when the error χ^2 is below $2/\langle I_0 \rangle$ where $\langle I_0 \rangle$ is the mean photon count per pixel of the empty beam intensity measured on the detector.

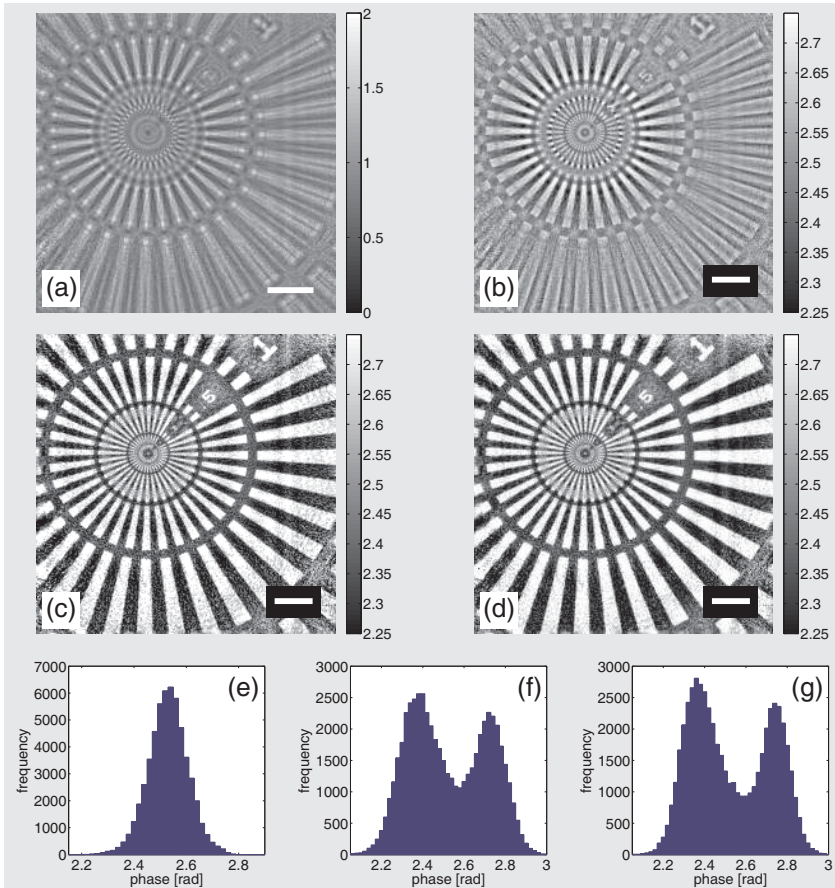


Figure 5.6: (a) Normalized Siemens star diffraction pattern. The scale bar indicate 3 mm. (b)-(d) Reconstructed phase of the normalized hologram shown in subfigure (a): (b) Holographic reconstruction, (c) GS reconstruction, (d) GS-Gaussian GS reconstruction. Scale bar and colorbar indicate $4 \mu\text{m}$ and phase [rad], respectively. (e)-(g) Histograms corresponding to the reconstructions (b)-(d), respectively, exhibiting the improved phase recovery by use of the iterative algorithms. The distance between the maxima of the histograms of (f) 0.36 rad and (e) 0.38 rad are in approximate agreement with the expected phase shift of 0.4 rad.

The first guess in the sample plane $\psi_{N_{\text{it}}=0}(x, y)$ is given by the holographic reconstruction of the object wave. The phase reconstruction of the Siemens star after $N_{\text{it}} = 33$ iteration steps is shown in Fig. 5.6 (c). Compared to the holographic reconstruction, the expected phase shifts are significantly better recovered. The histograms of the holographic and GS reconstructed phase distribution shown in Fig. 5.6 (e) and (f), respectively, exhibit this effect.

To further optimize the phase recovery we used an additional reconstruction tool proposed by Marchesini et al. [100] which consists of using a blurred version of the current estimate of the object under reconstruction. The blurring acts to smooth out noise and provides a form of regularization. The blurring was carried out by convolving the reconstructed wave-field with a Gaussian of width σ at each iteration step. The width σ is set to 1 pixel (full width at half maximum of 2.3548σ). The projection operator acts on the amplitude of the convolved estimate of the object

$$\mathcal{P}'_1|\text{conv}(\psi(x, y), \phi_{\text{Gauss}})| = 1. \quad (5.6)$$

Here, conv is the convolution and ϕ_{Gauss} the Gaussian of width σ . We denote the algorithm GS-Gaussian. Compared to the holographic reconstruction and the GS reconstruction, applying the GS-Gaussian algorithm reduces the spatial resolution of the reconstructed object due to the blurring. The resolution can be recovered by applying the GS algorithm in a second reconstruction step. The phase reconstruction of the Siemens star after application of $N_{\text{it}} = 50$ iteration steps using the GS-Gaussian algorithm and successive application of $N_{\text{it}} = 14$ iteration steps using the GS algorithm is shown in Fig. 5.6 (d). The histogram of the phase distribution shown in Fig. 5.6 (f) demonstrate the optimized phase shift recovery compared to the GS reconstruction. The maxima of the histogram in subfigure (f) yield a relative phase shift of 0.38 rad compared to the relative phase shift of 0.36 rad as obtained from the histogram in subfigure (e). The reconstructed phase shift is in approximate agreement with the expected (theoretical) phase shift of 0.4 rad between the Ta structure and the void areas.

In a next step, we have used the known informations on the object for the reconstruction, for instance the transmission to be minimal $T = 0.96$ (Ta region of the object) and maximal $T = 1$ (else). Setting this threshold on the amplitude of the object wave in the sample plane, the error-reduction algorithm yields

$$\psi(x, y) = \lim_{n \rightarrow \infty} (\mathcal{P}'_1 \mathcal{D}_{-z_{\text{eff}}} \mathcal{P}_2 \mathcal{D}_{z_{\text{eff}}})^{N_{\text{it}}} \psi_{N_{\text{it}}=0}(x, y), \quad (5.7)$$

with the real-space constraint given by

$$\mathcal{P}'_1|\psi(x, y)| = \begin{cases} 1 & \text{if } |\psi(x, y)| > 1, \\ 0.96 & \text{if } |\psi(x, y)| < 0.96, \\ |\psi(x, y)| & \text{else.} \end{cases} \quad (5.8)$$

We denote the algorithm with the specific real-space constraint ER-min-max. The first guess in the sample plane is given by the holographic reconstruction. The phase reconstruction of the Siemens star after $N_{it} = 22$ iteration steps (stop criterion) is shown in Fig. 5.7 (a). The run of the error curve presented in Fig. 5.7 (b) illustrates the rapid convergence of the algorithm. Compared to the holographic reconstruction shown in Fig. 5.6 (b), the expected phase shifts are noticeably better recovered. The histogram of the ER-min-max reconstructed phase distribution shown in Fig. 5.7 (c) illustrates this effect. However, compared to the reconstruction by use of the GS and the GS-Gaussian algorithm the relative phase shifts are suboptimal recovered. The maxima of the histogram indicate a relative phase shift of 0.28 rad which is only in coarse agreement with the expected phase shift of 0.4 rad.

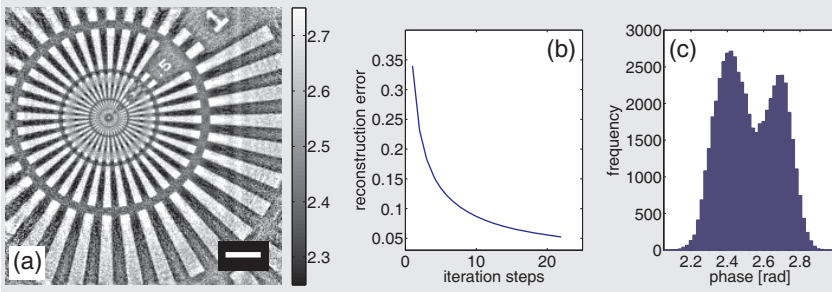


Figure 5.7: (a) Reconstructed phase of the normalized hologram using the ER-min-max algorithm. (b) Reconstruction error of the ER-min-max algorithm. The reconstruction stops after $N_{it} = 22$ iteration steps. (c) Histogram corresponding to the reconstruction in (a).

Fig. 5.8 (a) and (b) show details of the holographic reconstruction and the GS reconstruction, respectively. The red dotted semi-circle indicate the non-reconstructed spatial frequencies in the holographic reconstruction. In the GS reconstruction the non-transferred spatial frequencies due to the zeros in the PCTF are relatively well recovered. We assume that the constraint set on $|\psi(x, y)|$ enables to partly fill out the missing information.

5.1.5 Holographic imaging and reconstruction: Grid pattern

The grid pattern with $1 \mu\text{m}$ pitch is a less sophisticated structure than the Siemens star which should facilitate reconstruction. Fig. 5.9 (a) shows the normalized hologram of the grid pattern situated at a distance $z_1 = 4.48 \text{ mm}$ of the

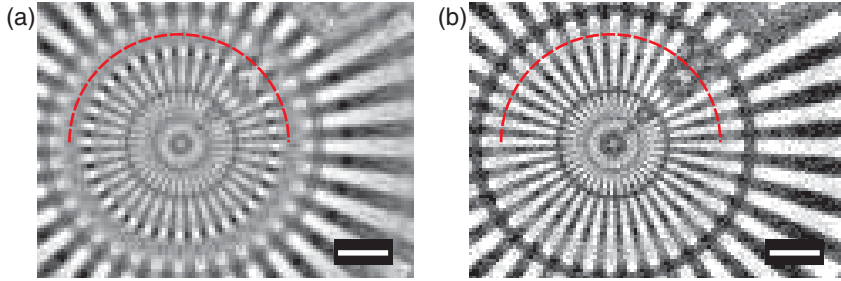


Figure 5.8: (a) Holographic reconstruction, along with a red dotted semi-circle indicating the non-reconstructed spatial frequencies. (b) Phase reconstruction using the GS algorithm. The non-transferred spatial frequencies are well recovered. The error bar indicates $2\ \mu\text{m}$.

crossed waveguides during the exposure and measured at a distance $z_2 = 3.09\ \text{m}$. The total photon flux measured on the detector was $1.6 \cdot 10^7\ \text{ph/s}$. Some enhanced noise effects are observed at the outer region of the hologram due to the lower intensity of waveguide far-field tails. These artifacts are visible on the holographic reconstruction shown in Fig. 5.9 (b), too. Overall the structure of the grid pattern is well recovered. A detail of the holographic reconstruction taken close to the center of the image is shown in Fig. 5.9 (c). For iterative reconstruction we have used the GS-Gaussian method presented in the previous section. Fig. 5.9 (d) shows the phase reconstruction after applying $N_{\text{it}} = 5$ iteration steps of the GS-Gaussian algorithm starting with the holographic reconstruction as a first guess, followed by $N_{\text{it}} = 2$ iterations using the GS algorithm. The iterative reconstruction yields an improved phase contrast compared to the holographic reconstruction. To illustrate this effect, the histograms of the holographic and the GS-Gaussian GS reconstruction are shown in subfigure (e) and (f), respectively. The relative phase shift between the Ta structure and the void areas are $0.26\ \text{rad}$ and $0.34\ \text{rad}$ as determined from the maxima in the histograms of subfigure (e) and (f), respectively. Hence, the reconstruction algorithms only enable a semi-quantitatively reconstruction of the object in terms of phase recovery¹⁶. In particular, the iterative reconstruction of the grid pattern yields a less efficient phase retrieval compared to the iterative reconstruction of the Siemens star. We assume that the iterative reconstruction is influenced by the relatively strong noise in the diffraction pattern.

¹⁶Note that the use of the GS and the ER-min-max algorithm did not improve reconstruction quality compared to the result of the GS-Gaussian method.

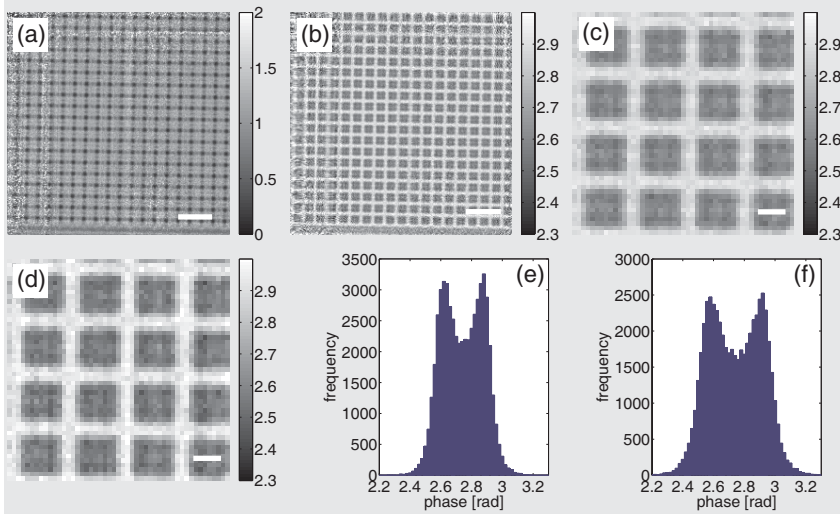


Figure 5.9: (a) Normalized hologram of the grid pattern. Scale bar indicate 2 mm. (b) Holographic reconstruction of the measured hologram. Scale bar indicate $3 \mu\text{m}$, the phase in [rad] is encoded according to the colormap. (c) Detail of the phase reconstruction shown in subfigure (b), the scale bar indicate 500 nm. (d) Phase reconstruction using the GS-Gaussian algorithm shows improved phase contrast compared to holographic reconstruction. Likewise, the peaks of the histogram shown in (f) of iterative reconstruction are more distant than in case of the histogram shown in (e) of holographic reconstruction.

5.1.6 Resolution limit

The spatial resolution of reconstructed holographic images obtained with the present setup is influenced by several factors, which limit the maximum accessible resolution for a given sample on different levels. On the most fundamental level the resolution is limited by the highest angle with respect to the optical axis, at which diffracted photons can be collected, i.e., the numerical aperture of the diffracted light cone. Depending on the total fluence incident on the sample, the sample scattering strength and the diameter of the waveguide exit wave the diffracted light cone can be larger or smaller than the waveguide exit cone.

On a less fundamental level, the resolution can be limited even further by the geometry of the experiment, i.e., the numerical aperture of the detector, and the geometric magnification factor. Due to steric constraints in the position-

ing stages, higher magnifications M (smaller z_1) as well as higher numerical apertures of the detector and thus a possibly higher resolution could not be tested. In order to estimate the resolution range that can be achieved with the present setup, i.e., leaving the detector area and pixel size, the sample scattering strength and the photon wavelength constant, we have simulated and reconstructed holograms with these four parameters identical to those in the experiment¹⁷ [47] (implementation carried out by Klaus Giewekemeyer). The waveguide exit field was modeled by a Gaussian beam with a waist full width at half maximum (FWHM) of 10 nm. The simulation of the hologram and the holographic reconstruction was performed in the parallel beam geometry.

In the simulated experiment, the geometry was optimized to a high spatial resolution, i.e. a pattern consisting of lines and spaces with a half period of 13.5 nm was placed 74.7 μm downstream of the waveguide exit plane. The detector received nearly the full waveguide exit cone at a distance of 1.37 m downstream of the waveguide exit plane and accumulated a total number of $6.4 \cdot 10^{12}$ photons, which could have been collected in about $10^4 \text{ s} \approx 2.8 \text{ h}$ in the real experiment, during which a total number of $6.4 \cdot 10^8$ photons were exiting the waveguide per second (see above). The resulting simulated average fluence on the sample was thus $1.2 \cdot 10^{13} \text{ ph}/\mu\text{m}^2$ with a geometrical magnification factor of $M = 18394$. The normalized hologram resulting from this simulation is presented in Fig. 5.10 (a) with the corresponding holographic reconstruction shown in Fig. 5.10 (b), indicating that line pairs with a half period of 13.5 nm are clearly resolved, with minor artifacts due to the direct holographic inversion of the data, which can be further improved by iterative methods. Fig. 5.10 (c) shows a holographic reconstruction from a simulated dataset obtained with the same set of parameters as before, except a total photon number of $6.4 \cdot 10^8$, corresponding to the photon count accumulated in one second on the detector area in the real experiment. Even here the line pairs are still visible, indicating a high robustness of the holographic reconstruction with respect to strong noise.

The waveguide-based setup takes advantage of the high spatial coherence due to the small diameter of the waveguide exit wave-field, i.e. the high transverse coherence of the waveguide beam. The simulation presented in Fig. 5.10 assumes full longitudinal coherence. However, the longitudinal coherence of the experimental setup is limited by the spectral bandpass $\Delta\lambda/\lambda \approx 0.016$ of the pre-focused beam.

¹⁷A minor difference with respect to one of the four parameters was the following: The detector area used for the reconstruction shown in Fig. 5.4 was 256×241 pixels, for the simulation we have used a square area of 248×248 pixels with the same pixel size as in the experiment.

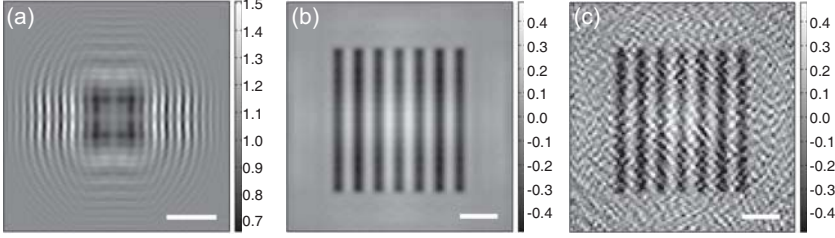


Figure 5.10: (a) Simulated normalized hologram of a lines-and-spaces (LS) pattern with the same contrast as the Ta test pattern and a total photon count on the detector 10^4 times higher than collected in the experiment per one second. Scale bar and colorbar indicate 3 mm and normalized intensity, respectively. (b) Holographic reconstruction corresponding to the hologram shown in subfigure (a). The LS pattern has a half-period of 13.5 nm. Scale bar and colorbar indicate 50 nm and phase in [rad], respectively. (c) Holographic reconstruction corresponding to the hologram shown in subfigure (a), however now simulated with a total number of photons 10^4 times lower. Same scale bar and colorbar indication as for subfigure (b).

In section 1.3 we introduced the phase and amplitude contrast transfer functions (CTFs) given by

$$\begin{aligned} \text{PCTF} &= \sin \chi \\ \text{ACTF} &= \cos \chi, \end{aligned} \quad (5.9)$$

with $\chi = (\lambda z_{\text{eff}}/4\pi)(k_x^2 + k_y^2)$. According to Eq. (5.9), the two ends of a wavelength interval $\Delta\lambda$ will fall onto a maximum and a minimum of the contrast transfer function, respectively, if $\Delta\lambda = 4\pi^2 / [z_{\text{eff}}(k_x^2 + k_y^2)]$. Therefore, the bandpass must be sufficiently small [29]

$$\frac{\Delta\lambda}{\lambda} \leq \frac{4\pi^2}{\lambda z_{\text{eff}}(k_x^2 + k_y^2)}, \quad (5.10)$$

to avoid a smearing of the intensity fringes in the hologram. In other words, the spatial resolution in waveguide-based imaging is not affected as long as $(\Delta\lambda/\lambda) = 4\pi^2/(\lambda z_{\text{eff}} k_x^2)$, considering the problem in one dimension here for clarity. Given a pixel size of Δx the largest possible (full-period) spatial frequency $\nu_x = k_x/2\pi$ that can be resolved (Nyquist rate) is given as $1/(2\Delta x)$, so that the maximum allowable bandpass becomes [11]

$$\frac{\Delta\lambda}{\lambda} \leq \frac{4(\Delta x)^2}{\lambda z_{\text{eff}}}. \quad (5.11)$$

With $4(\Delta x)^2/(\lambda z_{\text{eff}}) \approx 0.007$ in case of the simulated experiment, it follows that high resolution imaging using the presented experimental setup is limited by partial longitudinal coherence. This is no longer the case if monochromatic radiation, e.g. by a Si(111) monochromator is used, as in the next subsection.

5.1.7 Holographic imaging and reconstruction: 50 nm lines-and-spaces

The imaging experiment on the 50 nm LS pattern is carried out at the holography endstation of the P10 beamline (see section 4.4.1 for the experimental setup). The sample is placed on a bottom up mounted stage enabling short distances between sample and waveguide placed on an upside down mounted stage. The sample stage is equipped with an air-bearing rotation (Micos) for ultra-high precision turns needed for waveguide-based nano-tomography in future experiments. On top of the rotation, a group of xyz piezos (Physik Instrumente) is used for aligning the sample in the axis of rotation. Additional xyz stages (Micos) below the rotation are used for aligning the rotation axis in the x-ray beam and for distance variation between the waveguide and the sample. In contrast to the waveguide far-field measurements shown in section 4.4.1 we have used a CCD camera (PI-LCX:1300, 1340×1300 pixels, Princeton Instruments) with smaller pixel size of $20 \times 20 \mu\text{m}^2$ to measure the holograms.

The 50 nm LS pattern is structured only in one direction. As the intensity exiting the planar waveguide was significantly higher than of the crossed waveguide, imaging was performed using the planar waveguide taking advantage of the small source size in the direction perpendicular to the sample structure.

The 50 nm LS pattern was imaged at a distance $z_1 = 1.59$ mm downstream from the waveguide and the in-line hologram was recorded at a distance $z_2 = 5.15$ m. The shorter distance between waveguide and sample resulted in a higher magnification factor $M = 3239$ and shorter effective distance $z_{\text{eff}} = 1.59$ mm compared to the ID22-NI experiment. Taking further advantage of the smaller pixel size in the detection plane the effective pixel size in the object plane was only 6.2 nm.

Fig. 5.11 (a) shows the measured hologram normalized by the waveguide far-field. The small features correspond to the lines-and-spaces pattern. Fig. 5.11 (b) shows the holographic reconstruction of the hologram region indicated by the white dotted lines in subfigure (a). To further characterize the reconstruction we have performed a line scan integration over the horizontal direction. The integrated line scan is shown in Fig. 5.11 (c). The mean distance between minima and maxima of the structure yields $d = 53$ nm whereas a half-period of 50 nm was determined by electron microscopy. This discrepancy can be attributed to a

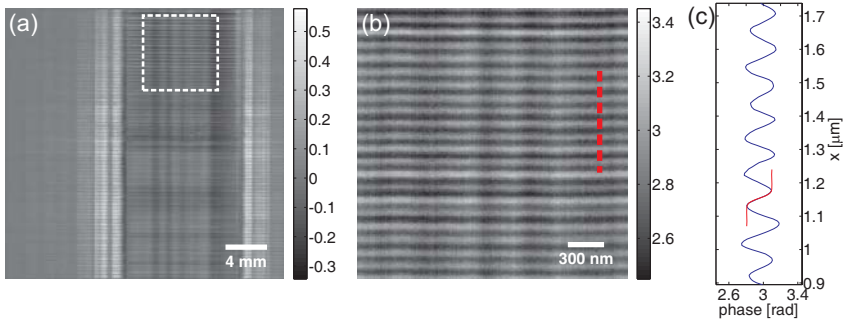


Figure 5.11: (a) Normalized hologram of the 50 nm lines-and-spaces test pattern, the intensity is encoded in the colormap. (b) Holographic reconstruction from the subregion indicated by the white dotted lines of the hologram in subfigure (a). Colorbar indicate phase in [rad]. (c) Line scan integrated over the horizontal direction corresponding to the red dotted bar (in vertical direction) of the holographic reconstruction shown in subfigure (b).

deviation of the actual from the nominal waveguide-to-sample distance, which should therefore be calculated independently.

5.2 Biological imaging

Biological samples like cells are mainly composed of low density elements. Depending on the nature of the cells the diameter lies usually in between 1 – 30 μm . Thus, expected amplitude and phase shifts of x-rays passing through biological sample are significantly lower compared to thick test pattern composed of the high electron density material Ta presented in the previous section 5.1. On one hand the reduced scattering strength of cells necessitates longer exposure times for high resolution imaging which further raise the problem of radiation damage to the cell. On the other hand the essentially pure phase object character of the cell allows the use of iterative algorithms with strong support constraint for object reconstruction.

5.2.1 Dictyostelium discoideum cell imaging

Waveguide-based imaging on biological cells is presented. The experiment is performed on the eukaryotic amoeba dictyostelium discoideum prepared by Klaus Giewekemeyer. The cells of wild-type strain AX2-214 are adhered on a thin polyimide film (Mitegen, USA) before rapid freezing in liquid ethane to

prevent crystallization of the phosphate buffer solution. The cells are then freeze-dried using a commercial freeze-drier (Christ, Germany). Further details of the preparation process are described in [101].

The experiment at the beamline ID22 was carried out using the setup and the experimental settings presented in section 4.3.1 as well as the sample stage presented in section 5.1.2. The unstained cells were placed at a distance $z_1 = 8.83$ mm from the two-crossed waveguide and the holograms were measured at a distance $z_2 = 3.09$ m from the sample resulting in a geometrical magnification factor of $M = 351$ taking into account the point-source character of the waveguide. Describing the imaging experiment in the parallel beam geometry the effective distance sample-to-detector is given by $z_{\text{eff}} = 8.83$ mm. To eliminate the effect of fluctuations and long-term drift in the waveguide exit field each hologram was recorded at an exposure time of 0.2 s followed each by subsequent measurement of the waveguide intensity with equal exposure time. Fig. 5.12 (a) shows the normalized intensity distribution calculated out of 710 measurements of the holographic intensity diffracted from the sample and the waveguide far-field intensity corresponding to a total illumination time of 142 s.

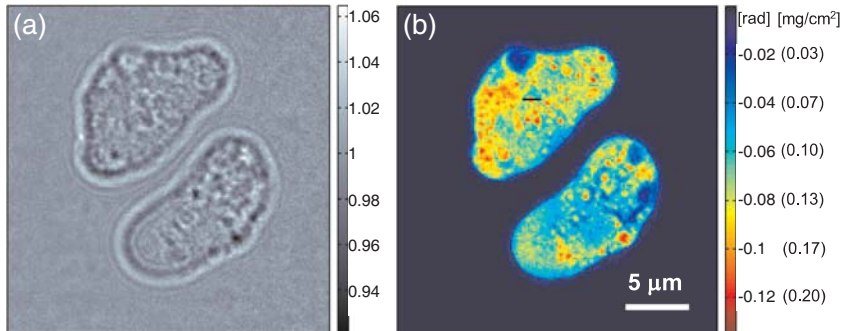


Figure 5.12: (a) Holographic intensity diffracted at unstained freeze-dried cells, normalized by the waveguide far-field intensity. The intensity is encoded in the colormap. (b) Reconstructed phase distribution obtained by using a modified HIO algorithm. The colorbar is scaled in [rad] and in [mg/cm²], indicating the projected effective mass density of the cells.

The total fluence applied on the sample was $4.9 \cdot 10^6$ ph/μm² (taking into account the total exposure time of 71 s applied on the sample) corresponding to a dose of about 10^3 Gy [11]. The expected phase and amplitude shifts of an unstained 3 μm thick biological object with a protein volume content of 50% are $\phi = 0.13$ rad and $A = 8.7 \cdot 10^{-5}$ at a photon energy of $E = 17.5$ keV.

The cells were reconstructed using a modified HIO algorithm where the support constraint is applied on the phase of the updated iterate of the object function in the object plane. The algorithm was developed and implemented by Klaus Giewekemeyer. The support of the sample is determined from the holographic reconstruction. Further details on the reconstruction methods are given in [11]. Fig. 5.12 (b) shows the phase reconstruction of the cells. The maximum phase shift of about 0.13 rad due to freeze-dried cells is in agreement with the expected phase shift. As the cells essentially act as pure phase objects the reconstructed phase distribution can be rescaled to a projected electron density map. Using Eq. (1.26) $\delta = 2\pi\rho_e r_e / k^2$ and Eq. (1.35) $\phi(x, y) = -k\delta_z(x, y)$, where $\delta_z(x, y)$ is the projection of $\delta(x, y, z)$ into the direction of the beam after traveling a distance $\Delta = t$, the projected electron density is related to the phase shift at a pixel (x, y) via $\rho_e(x, y) = -\phi(x, y)k / (2\pi r_e)$. Further the effective area mass density $\tilde{\rho}_m$ is given by $\tilde{\rho}_m = 2u\rho_e$ where u is the atomic mass unit. For low electron density elements of biological materials the absolute mass density indicated by the additional colorbar scaling in Fig. 5.12 (b) can be approximated by $\rho_m = A(x, y) / 2Z(x, y) \cdot \tilde{\rho}_m \approx \tilde{\rho}_m$ with $A(x, y)$ and $Z(x, y)$ denoting the mass number and the atomic number, respectively. Thus, the waveguide-based imaging experiment enabled quantitative imaging of biological sample which allowed for structural investigation of characteristic cell features [11].

5.3 Conclusions

Waveguide-based imaging on well-defined test pattern and biological samples was demonstrated. The imaging setup takes advantage of the spatial and coherent filtering of the pre-focused synchrotron beam by use of two-component cladding waveguides. The high photon flux exiting the waveguide optics and the high divergence of the waveguide beam resulted in an efficient illumination of the samples. A photon flux on the order of $10^7 - 10^8$ ph/s impinged onto the samples. From measured holograms, the samples are reconstructed using holographic and iterative methods. Holographic reconstruction proved to be a fast and robust method to retrieve the phase information. Optimized phase recovery is obtained by use of iterative algorithms. Image artifacts related to the twin-image problem and the effect of non-transferred spatial frequencies are significantly reduced in iteratively reconstructed objects. Finally, x-ray propagation microscopy on biological cells using waveguides as a quasi-point source was demonstrated.

6 Summary

The aim of this work was 1.) to design and fabricate optimized x-ray waveguides, 2.) to investigate their optical properties, and 3.) to demonstrate their use in lensless imaging in combination with suitable phase retrieval algorithms.

In chapter 2 the theoretical background for propagation of x-ray fields in free space is described based on the scalar wave theory. We address the projection approximation and the corresponding optical transmission function, the contrast transfer function, the Fresnel scaling theorem, as well as object reconstruction from the measured diffraction pattern. To this end, holographic and iterative reconstruction methods, namely the Gerchberg-Saxton algorithm, the error-reduction algorithm and the hybrid input-output algorithm, are compared based on numerical simulations, in particular with regard to phase contrast samples.

Image formation and reconstruction sensitively depend on the parameters of the illumination function, such as extension, coherence, and curvature. In chapter 3 the optimization of waveguide optics for sample illumination is addressed. The mode structure inside planar waveguide is computed based on analytical and numerical calculations. To solve the problem of low transmission in particular for the desired small guiding core cross section, an optimized cladding design is presented. Simulation shows that the transmission of a waveguide is enhanced by more than factor of 6 by choosing an appropriate interlayer (inner cladding) compared to a conventional waveguide. Importantly, the two-component cladding yields an optimized transmission and mode structure for a broad range of (hard x-ray) photon energies. Appropriate layer sequences are worked out and compared using simulations. In particular, the beam diameter of the waveguide exit field is determined as a function of the guiding layer thickness. Based on an analogy to quantum-mechanical confinement of wave functions [60], the limit of smallest beam confinement is studied and compared to numerical results computed for the novel two-component waveguide design.

In chapter 4 the fabrication of waveguides with a Ge/Mo/C/Mo/Ge optical layer sequence optimized for the hard x-ray range is presented. Magnetron sputtering allows the deposition of layer sequences with well-defined thickness and low interface roughness. To efficiently block primary x-ray beams not impinging onto the optical layers, two techniques based on a bonding process by use of an InSn alloy as well as electroless nickel plating are developed and ensure proper capping and sealing of the optical films. By use of a focused ion beam, the smeared entrance and exit sides of the waveguide slices can be polished and cleaned. Finally, two-dimensionally confining compact waveguide systems are obtained by gluing two planar waveguides in a crossed geometry.

An extended study of planar two-component waveguides [20] as a function of the guiding layer thickness, the waveguide length and the applied photon energy has been carried out using an unfocused bending magnet beam, as presented in chapter 5. The developed beam blocking materials prove suitable also at high photon energies and short waveguide lengths. The angular acceptance and transmission of the waveguides are in approximate agreement with simulations. The experiments confirm that even for waveguides with 9 nm guiding layer thickness high transmission above 20% can be achieved. The divergence in terms of full width at half maximum of the 9 nm C waveguide is not much larger than for 18 nm C guiding layer thickness. However, more pronounced tails of the beam are observed, which may be employed to increase the effective numerical aperture and thus resolution in waveguide-based x-ray imaging.

Significantly higher photon flux density exiting the waveguide is obtained by using a pre-focused undulator beam. Experiments using a compact two-crossed x-ray waveguide with a cross section of $35 \times 35 \text{ nm}^2$ exhibited a photon flux of $10^8 - 10^9 \text{ ph/s}$ [47]. Two-component waveguides supporting at least 2 modes allow for considerably smaller source dimension than the cross-section of the guiding core due to the mode beating effect. The reconstruction of the measured far-field using an iterative reconstruction method demonstrates an effective source size of sub-15 nm in both lateral dimensions in agreement with the simulation.

The high divergence of the optimized planar and crossed waveguide system is used for imaging in the holographic regime (chapter 6). Imaging of a well-defined test pattern demonstrates a resolution down to 50 nm, whereas simulation has predicted a possible resolution of sub-15 nm. Object reconstruction by use of iterative algorithms reveals improved phase recovery compared to holographic reconstruction. Image artifacts related to the effect of non-transferred spatial frequencies and the twin-image problem are significantly reduced. Depending on the total photon flux impinging onto the sample, the iteratively reconstructed phase shifts are in good agreement with the expected theoretical values for the binary valued test pattern. Thin biological samples act as pure phase object in the hard x-ray range. As has been shown by imaging of isolated cells, a hybrid input-output algorithm with a modified phase constraint can be used to quantitatively reconstruct the object [11]. In particular, the reconstructed phase distribution can be attributed to an effective electron density map.

In summary, imaging with optimized waveguides enables high spatial resolution in the hard x-ray range. Current limitations in coherence and source size have been overcome using two-component cladding waveguides. Due to the high divergence of the waveguide beam and the uniform illumination of the sample,

current detector technology is fully exploited. The efficiency of the waveguides especially in the energy range above 15 keV enables imaging of material science and biological specimens as pure phase objects. This in turn allows the use of deterministic and fast converging algorithms for object reconstruction. Along with the high photon flux provided by the pre-focused waveguide system it opens a path for high resolution tomography on biological samples. Neither Fresnel zone plate nor compound refractive lenses has reached two-dimensional beam confinement down to 20 nm and below, in the hard x-ray range (at least not according to published work). Furthermore, the high coherence of the waveguide beam, decoupled from the source, presents a decisive advantage. In the future, the potential of waveguide optics can be exploited at the holography endstation of the P10 beamline [85], Petra III (Hamburg) dedicated inter alia to waveguide-based imaging. In particular, the advantage of efficient Kirkpatrick-Baez mirror pre-focusing and of the dedicated instrumentation can be exploited for more challenging imaging experiments. The European free-electron laser currently under construction will provide pulses with a duration of smaller than 100 fs, containing $10^{12} - 10^{13}$ transversely coherent photons at wavelength down to 0.1 nm [102]. Here, the use of waveguide optics could possibly help to define the illumination wavefronts in a single pulse imaging experiment, which otherwise would suffer from the statistical fluctuations inherent in the so-called self-amplified stimulated emission (SASE) principle.

A Fourier analysis

This appendix summarizes fundamentals of the Fourier analysis relevant for this work. We only state the theorems and refer the reader to standard textbooks [22, 26] for more detail and proof.

A.1 Fourier transform

The two-dimensional Fourier transform of a function $f(x, y)$ with respect to x and y is defined by [23]

$$\begin{aligned}\tilde{f}(k_x, k_y) &\equiv \mathcal{F}[f(x, y)] \\ &= \frac{1}{2\pi} \iint_{-\infty}^{\infty} f(x, y) \exp[-i(k_x x + k_y y)] dx dy,\end{aligned}\tag{A.1}$$

with k_x and k_y being the Fourier variables which are respectively conjugate to x and y .

A.2 Convolution theorem

The Fourier transform of the convolution

$$f(x, y) * g(x, y) \equiv \iint_{-\infty}^{\infty} f(x', y') g(x - x', y - y') dx' dy' \tag{A.2}$$

of two functions $f(x, y)$ and $g(x, y)$ is given by the product of their individual Fourier transforms:

$$\mathcal{F}[f(x, y) * g(x, y)] = 2\pi \{\mathcal{F}[f(x, y)]\} \times \{\mathcal{F}[g(x, y)]\}.\tag{A.3}$$

A.3 Fourier derivative theorem

The Fourier derivative theorem states that the operators $\partial/\partial x$ and $\partial/\partial y$ in real space correspond to a multiplication with ik_x and ik_y , respectively, in Fourier space:

$$\mathcal{F}\left[\frac{\partial^m}{\partial x^m} \frac{\partial^n}{\partial y^n} f(x, y)\right] = (ik_x)^m (ik_y)^n \mathcal{F}[f(x, y)].\tag{A.4}$$

A.4 Friedel's law

Friedel's law is a property of Fourier transforms of real functions [24]. Given a real function $f(x)$, its Fourier transform has the following properties:

$$\tilde{f}(k_x) = \tilde{f}^*(-k_x),\tag{A.5}$$

where \tilde{f}^* is the complex conjugate of \tilde{f} . The squared amplitude $|\tilde{f}|^2$ is centrosymmetric:

$$|\tilde{f}(k_x)|^2 = |\tilde{f}(-k_x)|^2. \quad (\text{A.6})$$

B Image processing

B.1 Discrete Fourier transform

The use of computers generally imply a discretization of data. Hence, imaging-related data processing relies on the discrete Fourier transform which is in the one-dimensional case of an N long vector f_m expressed by:

$$\tilde{f}_n = \mathcal{F}f = \frac{1}{\sqrt{N}} \sum_{m=0}^{N-1} f_m \exp[2\pi i n m / N]. \quad (\text{B.1})$$

By assuming $f(x)$ continuous and periodic and by choosing an appropriately narrow grid spacing Δx to sample the function, the following approximation can be made

$$f_m = f(m\Delta x). \quad (\text{B.2})$$

Accordingly, the Fourier transform is also sampled on a narrow grid spacing Δq

$$\tilde{f}_n = \tilde{f}(n\Delta q). \quad (\text{B.3})$$

The grid spacings in the discrete form of the Fourier transform are related to the length N of the vectors f_m and \tilde{f}_n , respectively, by

$$\Delta x \Delta q = \frac{2\pi}{N}. \quad (\text{B.4})$$

The numerical implementation of the discrete Fourier transform is optimized by using the fast Fourier transform (FFT), whose computing time scales as $N \log(N)$ instead of N^2 [103].

B.2 Grid spacing conversion

In section 1.1.4 we have shown that the Fraunhofer diffraction pattern $\psi_z(x', y')$ measured at a distance z in the detection plane is related to the object wave $\psi_0(x, y)$ in the object plane by

$$\psi_z(x', y') = h_z(x', y') \tilde{\psi}_0(q_x = \frac{k}{z} x', q_y = \frac{k}{z} y'), \quad (\text{B.5})$$

using slightly changed notations here. In the following we consider only the x-coordinate pointing out that the same approach is valid for the y- coordinate too. Assuming the diffraction pattern measured on a detector with pixel size $\Delta x'$ Eq. (B.5) shows that the grid spacing in Fourier space is given by

$$\Delta q_x = \frac{k}{z} \Delta x'. \quad (\text{B.6})$$

According to Eq. (B.4) Δq_x is related to the pixel size Δx in the object plane by $\Delta q_x = 2\pi/(\Delta x N_x)$. Inserting this expression in Eq. (B.6) and rearranging the parameters yields

$$\Delta x' = \frac{\lambda z}{\Delta x N_x}. \quad (\text{B.7})$$

Hence, the pixel size in the detection plane depends on the wavelength λ as well as on the propagation distance z . Note that the propagation by use of the free-space propagator or the Fresnel diffraction operator (see section 1.1.2 and 1.1.3, respectively) does not change the pixel size since both, the forward and backward Fourier transform, are applied. However, imaging using a divergent illumination function as it is the case in waveguide-based imaging results in a magnified image of the object in the detection plane (see section 1.4). Applying parallel beam reconstruction by Fresnel backpropagation the pixel size Δx in the object plane is related to the pixel size $\Delta x'$ in the detection plane through the magnification factor M

$$\Delta x = \frac{\Delta x'}{M} = \frac{z_1 \Delta x'}{z_1 + z_2}, \quad (\text{B.8})$$

where z_1 denotes the distance focal plane - object plane and z_2 the distance object plane - detection plane.

B.3 Sampling theorem

The sampling theorem was published by Shannon in the context of signal processing [38]. The theorem states that an continuous and band-limited function $\tilde{f}(q)$ with a range of frequencies from 0 to q_N has to be sampled at a frequency higher than $2q_N$ to reconstruct exactly $f(x)$. Here, the so-called Nyquist frequency $q_N = N\Delta q/2 = \pi/\Delta x$ is the highest frequency present in the discrete Fourier transformation for a given sampling interval Δx . The function $f(x)$ is band-limited if

$$\tilde{f}(q) = 0 \quad \text{for } |q| > B. \quad (\text{B.9})$$

Further, $f(x)$ is called oversampled according to the Shannon theorem if the condition $B < q_N$ is satisfied. On the other hand, a sampling interval larger than $1/(2\Delta x)$ leads to aliasing whereby frequencies higher than q_N appear as lower frequencies in $f(x)$.

B.4 Oversampling

In case of a diffraction pattern measured on a grid $N_x \times N_y$, the term band-limitation can be replaced by the term support [104]. The support \mathcal{S} has a maximum extent along each axis s_x and s_y where the function is non-zero. In analogy to Eq. (B.9), the support constraint is given by $|q_x| > N_x\pi/s_x$ and $|q_y| > N_y\pi/s_y$, respectively, leading to the sampling condition

$$\Delta q_x \leq \frac{2\pi}{s_x}, \quad \Delta q_y \leq \frac{2\pi}{s_y}. \quad (\text{B.10})$$

Since the diffraction pattern is only the intensity of the signal and phases are not known, the sampling theorem has to be applied to the autocorrelation in case of far-field diffraction pattern. In fact, the number of parameters we can obtain from the intensity is equal to the number of independent parameters from the autocorrelation. The autocorrelation is the Fourier transform of the intensity. The extension of the autocorrelation support is $a_x = 2s_x$ and $a_y = 2s_y$, respectively. Hence, aliasing in the autocorrelation is avoided if

$$\Delta q_x \leq \frac{\pi}{s_x}, \quad \Delta q_y \leq \frac{\pi}{s_y}. \quad (\text{B.11})$$

Accordingly, the diffraction pattern is oversampled in the sense of Shannon if Eq. (B.11) is satisfied. Equally, if the object is extended on an area $A_{\mathcal{S}}$ (support of the object function) and the computational field of view (FOV) is given by an area A_{FOV} , the Shannon oversampling criterion is fulfilled for

$$\sigma = \frac{A_{\text{FOV}}}{A_{\mathcal{S}}} \geq 4, \quad (\text{B.12})$$

where σ is the oversampling ratio. For demonstration of the oversampling criterion, the autocorrelation of Siemens star object for different oversampling ratio are shown in Fig. B.1.

A different approach to oversampling is derived from a lack of information in the detection plane [104]. Assuming a complex-valued object function, $2N_{\mathcal{S}}$ independent real variables are needed to be retrieved from the diffraction pattern: $N_{\mathcal{S}}$ variables related to amplitude information and $N_{\mathcal{S}}$ variables related to phase information. Now, if the object occupies the whole computational field of view of A_{FOV} the number of knowns in Fourier space is only $N_{\mathcal{S}}$ since the phase is missing. Accordingly, the oversampling condition can be expressed by [105]

$$\sigma = \frac{A_{\text{FOV}}}{N_{\mathcal{S}}}, \quad (\text{B.13})$$

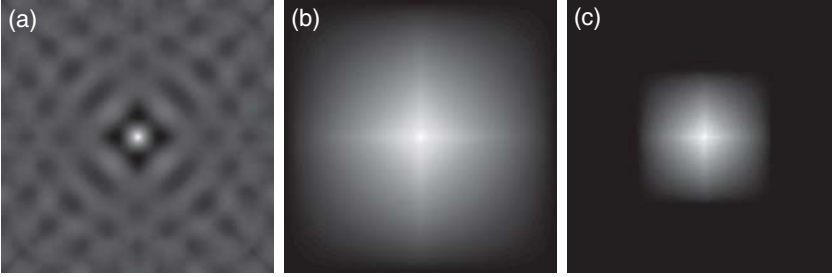


Figure B.1: Autocorrelation of the far-field intensity of the simulated Siemens star test object ($T = 0.93$, $\phi = 0.4$ rad) presented in section 1.5.3 for different oversampling ratio σ . The field of view is $A_{FOV} = 512^2$ pixels for all images. (a) $\sigma = 1$ ($A_S = 512^2$ pixels): the autocorrelation support is larger than A_{FOV} , i.e. the far-field pattern is not oversampled. (b) $\sigma = 4$ ($A_S = 256^2$ pixels): the oversampling criterion is fulfilled, i.e. the far-field pattern is oversampled. (c) $\sigma = 16$ ($A_S = 128^2$ pixels): again, the oversampling criterion is fulfilled. Note, however, that the increased oversampling ratio does not provide additional information for eventual reconstruction compared to the case $\sigma = 4$.

with $\sigma \geq 2$ being a necessary condition for a unique reconstruction.

The oversampling aspect is closely related to the problem of constraint sufficiencies in iterative methods [106]. As mentioned above, applying the sampling theorem to the diffraction pattern, the number of parameters we can obtain from the intensity is equal to the number of independent parameters from the autocorrelation. Regarding the fact that the measured intensity is a real function, Friedel's law is satisfied and according to Eq. (A.6) $\mathcal{F}^{-1}[|\mathcal{F}\psi(x, y)|^2] = \mathcal{F}^{-1}[|\mathcal{F}\psi(-x, -y)|^2]$, reducing the number of independent parameters to one half. Thus, the constraint ratio can be written as [106]

$$\Omega = \frac{1}{2} \frac{A_{auto}}{A_S}, \quad (\text{B.14})$$

where A_{auto} denotes the area of the autocorrelation support. Since the autocorrelation support is twice as large as the diffraction pattern in each spatial dimension, the constraint ratio condition $\Omega \geq 1$ is analogue to the oversampling condition $\sigma \geq 2$.

Obviously, the oversampling condition $\sigma \geq 2$ for two-dimensional diffraction pattern relaxes the Shannon oversampling criterion. To further investigate the effect of relaxed oversampling criteria, we simulated the Siemens star test object for $2 \leq \sigma < 4$. The field of view is $A_{FOV} = 512^2$ pixels and the object function extension is chosen to $A_S = 350^2$ pixels in the simulation resulting in

$\sigma = 2.1$. First, we consider a complex-valued object function with $T = 0.93$ and $\phi = 0.4$ rad.

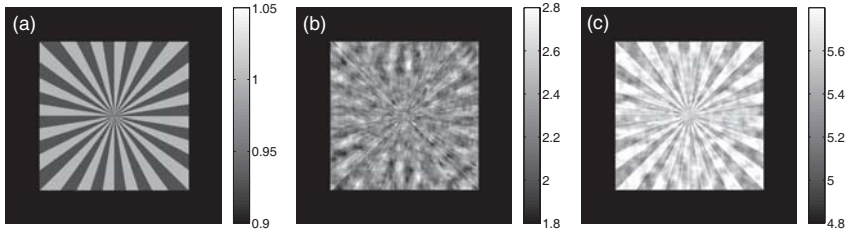


Figure B.2: (a) Amplitude of a Siemens star test object given a oversampling condition $\sigma = 2.1$. (b) Phase reconstruction from the far-field intensity of the complex-valued Siemens star object function shown in subfigure (a) after application of $N_{it} = 20000$ iteration steps using the HIO algorithm. Phase recovery is limited. (c) Phase reconstruction from the far-field intensity now of a pure phase Siemens star object after application of $N_{it} = 10000$ iteration steps using the HIO algorithm. Improved phase recovery compared to (b) but still significantly reduced reconstruction convergence compared to Shannon oversampled reconstruction.

Fig. B.2 (a) shows the amplitude of the Siemens star object. The phase reconstruction after $N_{it} = 20000$ iteration steps of the HIO algorithm is presented in Fig. B.2 (b). The edge structures delimiting the void areas and phase shifting areas of the Siemens star can be recognized from the reconstruction. However, the global phase recovery of the object is random. Note that after approximately $N_{it} = 150$ iteration steps the edge structures of the Siemens star are recovered. Further iteration steps do not significantly improve the phase recovery. Fig. B.2 (c) shows the phase reconstruction of a pure phase Siemens star object ($T = 1$, $\phi = 0.4$ rad) after $N_{it} = 10000$ iteration steps. Here, the phase recovery is significantly improved compared to the previously mentioned reconstruction. However, compared to the Shannon oversampled Siemens star presented in section 1.5.3 phase recovery is still poor. Note that in view of comparableness we did not apply the additional real-space constraint of the amplitude to be one (GS real-space constraint) in the HIO algorithm. In summary, the oversampling criterion $\sigma \geq 2$ indicates only a necessary condition for reconstruction of far-field pattern but does not ensure reconstruction to a global minimum solution [42].

B.5 Oversampling of Fresnel pattern

As presented in section 1.1.3, propagation of Fresnel pattern involves the use of the forward and inverse Fourier transformation. Hence, the autocorrelation of the object function does not provide information on oversampling criterion of the diffraction pattern. Further, propagation by application of the Fresnel diffraction operator \mathcal{D}_z^F

$$\psi_z(x, y) = \mathcal{D}_z^F \psi_0(x, y) \quad (\text{B.15})$$

$$= \exp(ikz) \mathcal{F}^{-1} \exp\left[\frac{iz(k_x^2 + k_y^2)}{2k}\right] \mathcal{F} \psi_0(x, y) \quad (\text{B.16})$$

includes the use of the Fresnel propagator given by

$$H(k_x, k_y) = \exp(ikz) \exp\left[\frac{iz(k_x^2 + k_y^2)}{2k}\right] \quad (\text{B.17})$$

in Fourier space. Eq. (B.16) yields an adequate analysis of the Fresnel pattern if the Shannon sampling condition is fulfilled [107]. Difficulties appear if the frequencies of the quadratic phase factor are higher than those of the object, i.e. if these higher frequencies of the propagator kernel are not sufficiently sampled [108]. As discussed in [40], extracting the phase function of Eq. (B.17) in case of backpropagation leads to

$$\phi_H(v_x, v_y) = -\pi\lambda z(v_x^2 + v_y^2), \quad (\text{B.18})$$

with $v_x = k_x/(2\pi)$, $v_y = k_y/(2\pi)$ and $k = 2\pi/\lambda$. In the following, we consider only one dimension since the sampling criterion for the two orthogonal variables can be analyzed individually. Assuming a uniform grid spacing Δv_x in Fourier space, the condition for the unaliased representation of the phase can be expressed by [40]

$$\Delta v_x \left| \frac{\partial \phi_H(v_x, v_y)}{\partial v_x} \right|_{\max} \leq \pi. \quad (\text{B.19})$$

Note that, since the phase appears as a complex exponential term it is also encoded in a modulo 2π format. Eq. (B.19) exhibits the maximum phase shift must be less or equal π between two adjacent grid samplings. The derivative is calculated to

$$\frac{\partial \phi_H(v_x, v_y)}{\partial v_x} = -2\pi\lambda z v_x. \quad (\text{B.20})$$

For fixed experimental conditions, λ and z are constants and the derivative term reaches a maximum for $v_x = v_{x_{\max}}$. Setting the slope maximum in Eq. (B.19) and rearranging parameters leads to

$$\Delta v_x \geq \frac{1}{2\lambda z |v_{x_{\max}}|}. \quad (\text{B.21})$$

Assuming that the computational field of view has an extent of $L_x = \Delta x N_x$ the grid spacing in Fourier space yields $\Delta v_x = 1/L_x$. The highest spatial frequency is given by the Nyquist rate $v_{x_{\max}} = 1/(2\Delta x)$. Using $\Delta v_x = 1/L_x$ and $v_{x_{\max}} = 1/(2\Delta x)$ and solving Eq. (B.21) for Δx leads to the real-space criterion for the oversampled H function:

$$\Delta x \geq \frac{\lambda z}{L_x}. \quad (\text{B.22})$$

Hence, aliasing in the Fresnel propagator is avoided if the condition given by Eq. (B.22) is fulfilled.

B.6 Uniqueness of reconstruction

Elser and Millane stated [106], that the degree of nonuniqueness in a reconstruction is very limited in case of a constraint ratio $\Omega > 1$ for space dimensions $d \geq 2$. A Shannon oversampled diffraction pattern has a constraint ratio $\Omega \geq 2$ in case of a convex and centrosymmetric support. Moreover, it was shown that for almost all finite-extent discrete diffraction patterns reconstruction of the complex-valued object is unique even in the presence of noise [109, 110]. The proof relies on the fact that complex functions in more than one dimension can usually not be factorized [111]. However, a two-dimensional complex-valued object can be reduced to a factorizable one-dimensional function in case of symmetries such as radial symmetry [112]. Thus, a Siemens star without an additional symmetry breaking object property cannot be uniquely reconstructed. The HIO algorithm enabled the successful reconstruction of the Shannon oversampled Siemensstar as shown in Fig. 1.7. Reconstruction of the same object using the ER algorithm failed as the algorithm stagnated in a non-unique solution. Apart from the considerations presented above, a further aspect of nonuniqueness has to be taken into account as discussed in [39]. The object $\psi(x, y)$ and its twin $\psi^*(-x, -y)$, the complex conjugated object rotated by 180° , have the same Fourier modulus. Furthermore, both objects have the same support since their support is symmetric with respect to the 180° -rotation. Starting from a random initial guess there is an equal probability that the algorithm will reconstruct one of the two objects. As the real-space and Fourier-space constraints in the

iterative algorithm do not distinguish between both object, characteristics of the two images can be reconstructed coevally. If the twin image can not be eliminated during reconstruction, i.e. convergence to one solution can not be achieved, the ER algorithm is trapped in a local minimum [39]. This problem particularly arises if the non-unique solution is close to the global minimum, i.e. the error in the reciprocal space is small.

Note that the ambiguities of $\psi(x, y)$, $\psi(x - x_0, y - y_0)$, $\psi(x, y)e^{i\varphi}$ and $\psi^*(-x, -y)$ having all the same Fourier modulus is usually not referred to the uniqueness problem but rather to the local minima problem. The same holds for objects that belong to the class of homometric structures, i.e object functions $h(x, y)$ that may be described by two isolated object distributions $f(x, y)$ and $g(x, y)$ through the convolution theorem [113]. Then for $g(x, y) \neq g^*(-x, -y)$, the diffraction pattern of $h(x, y) = f(x, y) * g(x, y)$ and $h'(x, y) = f(x, y) * g^*(-x, -y)$ cannot be distinguished using oversampling methods.

The iterative phase retrieval methods presented in section 1.5.2 are independent of the nature of the illumination function. Nugent et al. proposed an algorithm in which at each iteration step in the object plane the wavefront curvature used to obtain the diffraction pattern is replaced by the curvature corresponding to the next set of diffraction data [114]. In fact, by introducing the phase perturbation the uncertainties in the phase due to symmetries within the discontinuity structure are supposed to be overcome and therefore, reconstruction is unique. In order to use the curvature data as the only real-space constraint, the diffraction data has to be recorded for varying object-to-focal plane distances. Williams et al. used the retrieved wavefront information combined with the support constraint of the object for a unique reconstruction of a Fresnel diffraction pattern and called this method **Fresnel coherent diffractive imaging (FCDI)** [7]. Due to the need of a support constraint, only isolated objects can be reconstructed using FCDI. Hoppe et al. proposed the **ptychography** algorithm [115] which allows for reconstruction of extended objects. This method was first demonstrated experimentally in scanning electron microscopy [116] and further on applied to coherent diffractive x-ray imaging [117, 118, 119]. Ptychography relies on measuring different diffraction pattern in a scanning procedure. A necessary condition for efficient reconstruction is fulfilled if the different illuminated areas overlap. Similar to FCDI uniqueness is obtained by reconstructing the illumination function which on the other hand is obtained at the same time as the reconstruction of the optical transmission function. FCDI and ptychography can both be applied in waveguide-based imaging, the latter has been demonstrated experimentally [120].

B.7 Source code in MATLAB

Phase retrieval simulations

HIO_FFT.m

```

1 %% reconstruction of a simulated Siemens star object from the measured intensity in the far-field using the HIO algorithm
2 clear all;
3 close all;
4 addpath('/home/skrueger/PHD/Diss_vs3/matlab_tools/tools/');
5
6 %% parameters
7 % energy [keV]
8 E = 17.5;
9 % wavelength [m]
10 lambda = 12.398/E*1E-10;
11 % wave-number [1/m]
12 k = 2*pi/lambda;
13 % thickness sample [m]
14 t = 500e-9;
15 % Ta index of refraction (source: CXRD)
16 delta = 9.0368e-6;
17 beta = 8.1756e-7;
18
19 %% create object
20 % size of the field of view
21 Nim = 512;
22 % size of the object
23 Ns = 256;
24 % real part of the object
25 ima = zeros(Nim,Nim);
26 imas = star(Ns,20,Ns);
27 imas = exp(-k*beta*t.*imas);
28 ima((Nim/2-Ns/2+1):(Nim/2+Ns/2),(Nim/2-Ns/2+1):(Nim/2+Ns/2)) = imas;
29 % imaginary part of the object
30 imp = zeros(Nim,Nim);
31 imps = star(Ns,20,Ns);
32 imp((Nim/2-Ns/2+1):(Nim/2+Ns/2),(Nim/2-Ns/2+1):(Nim/2+Ns/2)) = imps;
33 imp = exp(-1i*k*delta*t.*imp);
34 % object
35 im = ima.*imp;
36
37 %% intensity in the detection plane
38 I = (abs(fftshift(fft2(im)))).^2;
39
40 %% autocorrelation
41 Auto = fftshift(iff2(I));
42
43 %% support
44 supp = zeros(size(im));
45 supp((Nim/2-Ns/2):(Nim/2+Ns/2-1),(Nim/2-Ns/2):(Nim/2+Ns/2-1)) = 1;
46
47 %% initial guess
48 clear x; clear err;
49 x = 0.5*rand(size(I)).*exp(0.05*1i.*rand(size(I)));
50
51 %% HIO algorithm
52 % beta parameter
53 beta = 1;
54 % initial guess in the object plane
55 in = x;
56 figure;
57 for l = 1:1:1000
58     n=n+1;
59     X = fft2(in);
60     % fourier-space constraint
61     out = ifft2(fftshift(sqrt(I)).*X./abs(X + eps));
62     % real-space constraint
63     in = supp.*out + (1-supp).*(in-beta*out);
64     % reconstruction error
65     err(l) = sum(sum(abs(1-(abs(fftshift(fft2(in.*supp)))).^2)))) ./ sum(sum(I));
66     subplot(2,2,1); imagesc(abs(im)); colormap gray; axis equal tight; colorbar; title('original image: amplitude'); caxis
67     ([0.9 1.05]); drawnow;
68     subplot(2,2,2); imagesc(abs(in)); colormap gray; axis equal tight; colorbar; title('reconstructed amplitude'); caxis
69     ([0.9 1.05]); drawnow;
70     subplot(2,2,3); imagesc(mod(angle(in),2*pi)); colormap gray; axis equal tight; colorbar; title('reconstructed phase');
71     drawnow;
72     subplot(2,2,4); plot(err); title(['iteration' num2str(l)]); drawnow;
73 end

```

star.m

```

1 %% create star
2 % Author: Martin Tolkiehn
3
4 function [s]=star( r, a, N )
5 s=linspace(-N/2, N/2-1, N);
6 s= repmat(s,N,1);
7 s=s+i*s';
8
9 s=(abs(s)<r).*(sin(a*angle(s))>0);

```

holo_recon.m

```

1 %% holographic reconstruction of a simulated Siemens star object from the measured intensity in the Fresnel near-field
2
3 %% for parameters and create object see HIO_FFT.m
4
5 %% propagation to the detection plane using the free-space propagator
6 N = numel(im);
7 N = numel(im);
8 % number of pixels
9 [Ny,Nx] = size(im);
10 % propagation distance in the effective geometry
11 z_eff = 4.48e-3;
12 % magnification factor
13 M = 690.7321;
14 % magnified pixel size in sample plane
15 dx_det = 55e-6;
16 dy_det = 55e-6;
17 % pixel size in sample plane
18 dx = dx_det/M;
19 dy = dx_det/M;
20 % coordinate system in sample plane
21 [X,Y] = meshgrid(dx*((1:1:Nx)-floor(Nx/2)-1),dy*((1:1:Ny)-floor(Ny/2)-1));
22 % magnified coordinate system in detector plane
23 [X_det,Y_det] = meshgrid(dx_det*((1:1:Nx)-floor(Nx/2)-1),dy_det*((1:1:Ny)-floor(Ny/2)-1));
24 % grid conversion in q-space
25 dqx = 2*pi/(Nx*dx);
26 dqy = 2*pi/(Ny*dy);
27 % coordinate system in q-space
28 [Qx,Qy] = meshgrid(dqx*((1:1:Nx)-floor(Nx/2)-1),dqy*((1:1:Ny)-floor(Ny/2)-1));
29
30 % for the free-space propagator
31 kappa = sqrt(k^2-(Qx.^2+Qy.^2));
32 % propagated object
33 Im = fftshift(iff2(fft2(iff2shift(im)).*fftshift(exp(1i*kappa*z_eff))));
34 % intensity in the detector plane
35 I = (abs(Im)).^2;
36
37 %% holographic reconstruction
38 in = fft2(iff2(I).*fftshift(exp(-1i*kappa*z_eff)));
39 % plot
40 figure;
41 imagesc(mod(angle(in),2*pi)); colormap gray; axis equal tight; colorbar; title('reconstructed phase');

```

GS_Fresnel.m

```

1 %% reconstruction of a simulated Siemens star object from the measured intensity in the Fresnel near-field using the GS
2 algorithm
3
4 %% for parameters, create object and propagation tools see above
5
6 %% GS algorithm
7 close all
8 clear x; clear err in;
9 % first guess
10 psi_ampl = rand(size(I));
11 in = psi_ampl.*I.*rand(size(I));
12 % beta parameter
13 beta = 1;
14 figure;
15 n = 0;
16 for l = 1:2000
17     n=n+1;
18     In = fftshift(iff2(fft2(iff2shift(in)).*fftshift(exp(1i*kappa*z_eff))));

```

```

18 % fourier-space constraint
19 In = sqrt(I).*(In./abs(In));
20 in = fftshift(fft2(fft2(fftshift(In)).*fftshift(exp(-1i*kappa*z_eff))));
21 % real-space constraint
22 psi_ampl = ones(size(in));
23 in = psi_ampl.*(in./abs(in));
24 % reconstruction error
25 err(1) = sum(sum(abs(sqrt(I)-(abs(fftshift(fft2(fft2(fftshift(in)).*fftshift(exp(1i*kappa*z_eff))))))).^2) ./ sum(
    sum(I));
26 if (n==100)
27 subplot(2,2,1); imagesc(angle(im)); colormap gray; axis equal tight; colorbar; title('original image: phase'); drawnow;
28 subplot(2,2,2); imagesc(abs(in)); colormap gray; axis equal tight; colorbar; title('reconstructed amplitude'); drawnow;
29 subplot(2,2,3); imagesc(angle(in)); colormap gray; axis equal tight; colorbar; title('reconstructed phase'); caxis
    ([1.3 1.8]); drawnow;
30 subplot(2,2,4); plot(err); title(['iteration' num2str(1)]); drawnow;
31 n = 0;
32 end
33 end

```

ER-GS_Fresnel.m

```

1 %% reconstruction of a simulated Siemens star object from the measured intensity in the Fresnel near-field using the ER-GS
  algorithm
2
3 %% for parameters, create object and propagation tools see above
4
5 %% support
6 supp = zeros(size(im));
7 supp((Nim/2-Ns/2):(Nim/2+Ns/2-1),(Nim/2-Ns/2):(Nim/2+Ns/2-1)) = 1;
8
9 %% ER-GS algorithm
10 close all
11 clear x; clear err in;
12 % first guess
13 psi_ampl = rand(size(I));
14 in = psi_ampl.*1i*rand(size(I));
15 % beta parameter
16 beta = 1;
17 figure;
18 n = 0;
19 for l = 1:2000
20     n=n+1;
21     In = fftshift(fft2(fft2(fft2(fftshift(in)).*fftshift(exp(1i*kappa*z_eff))));
22     % fourier-space constraint
23     In = sqrt(I).*(In./abs(In));
24     in = fftshift(fft2(fft2(fftshift(In)).*fftshift(exp(-1i*kappa*z_eff))));
25     % real-space constraint
26     in = supp.*(in./abs(in));
27     % reconstruction error
28     err(1) = sum(sum(abs(sqrt(I)-(abs(fftshift(fft2(fft2(fftshift(in)).*fftshift(exp(1i*kappa*z_eff))))))).^2) ./ sum(
        sum(I));
29     if (n==100)
30 subplot(2,2,1); imagesc(angle(im)); colormap gray; axis equal tight; colorbar; title('original image: phase'); drawnow;
31 subplot(2,2,2); imagesc(abs(in)); colormap gray; axis equal tight; colorbar; title('reconstructed amplitude'); drawnow;
32 subplot(2,2,3); imagesc(angle(in)); colormap gray; axis equal tight; colorbar; title('reconstructed phase'); caxis
        ([1.3 1.8]); drawnow;
33 subplot(2,2,4); plot(err); title(['iteration' num2str(1)]); drawnow;
34     n = 0;
35     end
36 end

```

HIO_Fresnel.m

```

1 %% reconstruction of a simulated Siemens star object from the measured intensity in the Fresnel near-field using the ER-GS
  algorithm
2
3 %% for parameters, create object and propagation tools see above
4
5 %% support
6 supp = zeros(size(im));
7 supp((Nim/2-Ns/2):(Nim/2+Ns/2-1),(Nim/2-Ns/2):(Nim/2+Ns/2-1)) = 1;
8

```

```

9 %% HIO algorithm
10 close all
11 clear x; clear err in;
12 % first guess
13 psi_ampl = rand(size(I));
14 in = psi_ampl.*1i*rand(size(I));
15 % beta parameter
16 beta = 1;
17 figure;
18 n = 0;
19 for l = 1:2000
20     n=n+1;
21     In = fftshift(fft2(fft2(fftshift(in)).*fftshift(exp(1i*kappa*z_eff))));
22     % fourier-space constraint
23     In = sqrt(I).*(In./abs(In));
24     out = fftshift(fft2(fft2(fftshift(In)).*fftshift(exp(-1i*kappa*z_eff))));
25     % real-space constraint
26     in = supp.*out + (1-supp).*(in-beta*out);
27     % reconstruction error
28     err(l) = sum(sum(abs(sqrt(I)-(abs(fftshift(fft2(fft2(fftshift(supp.*in)).*fftshift(exp(1i*kappa*z_eff)))))).^2)
29         ./ sum(sum(I))));
30     if (n==100)
31         subplot(2,2,1); imagesc(angle(in)); colormap gray; axis equal tight; colorbar; title('original image: phase'); drawnow;
32         subplot(2,2,2); imagesc(abs(in)); colormap gray; axis equal tight; colorbar; title('reconstructed amplitude'); drawnow;
33         subplot(2,2,3); imagesc(angle(in)); colormap gray; axis equal tight; colorbar; title('reconstructed phase'); drawnow;
34         subplot(2,2,4); plot(err); title(['iteration' num2str(l)]); drawnow;
35         n = 0;
36     end
end

```

Iterative reconstruction of the waveguide near-field

WG_ER.m

```

1 %% Reconstruction of the waveguide near-field from the measured far-field using the ER algorithm
2 clear all;
3 close all;
4 % Parameter declaration
5 data_dir = '/home/AG_Salditt/Messzeiten/2009/ID22_SC2732/Auswertung/SPK/linux/IC35nm NTT_ff_zucker/';
6 filename = 'ff_combined_clean.mat';
7 load([data_dir filename]);
8 % cleaned far-field
9 I_exp = ccd_m(:,4:end);
10 % enlarge grid
11 m = 19;
12 Dummy = zeros(size(I_exp));
13 dummy = repmat(Dummy,m,m);
14 dummy((m-1)/2*size(I_exp,1)+1:(m-1)/2*size(I_exp,1), (m-1)/2*size(I_exp,2)+1:(m-1)/2*size(I_exp,2)) = I_exp;
15 I_exp = dummy;
16 % center far-field
17 cy = 6100;
18 cx = 7170;
19 % number of pixels
20 Nx = 4000;
21 Ny = 4000;
22 I_exp_cen = I_exp(cy-Ny/2:cy+Ny/2-1, cx-Nx/2:cx+Nx/2-1);
23
24 %% parameters and coordinate systems
25 % energy in [keV]
26 E = 17.5;
27 % wavelength in [m]
28 lambda = 12.398/E*1E-10;
29 k = 2*pi/lambda;
30 % propagation distance
31 z12 = 3.09;
32 % pixel size detection plane
33 d2x = 55*1E-6;
34 d2y = 55*1E-6;
35 [X_2,Y_2] = meshgrid(d2x*((1:Nx)-floor(Nx/2)-1),d2y*((1:Ny)-floor(Ny/2)-1));
36 % pixel width in WG plane
37 d1x = lambda*z12/(d2x*Nx);
38 d1y = lambda*z12/(d2y*Ny);
39 [X_1,Y_1] = meshgrid(d1x*((1:Nx)-floor(Nx/2)-1),d1y*((1:Ny)-floor(Ny/2)-1));
40 % coordinate system in Fourier space

```

```

41 dq2x = 2*pi/(Nx*dix);
42 P.dq2x = dq2x;
43 dq2y = 2*pi/(Ny*diy);
44 P.dq2y = dq2y;
45 [Q2_x,Q2_y] = meshgrid(dq2x*((1:Nx)-floor(Nx/2)-1),dq2y*((1:Ny)-floor(Ny/2)-1));
46
47 %% autocorrelation
48 auto = fftshift(fft2(fftshift(I_exp_cen)))/sqrt(numel(I_exp_cen));
49
50 %% support
51 supp = max(rectang_erf(X_1,Y_1,0,0,150e-9,150e-9,0,10e-9),0);
52
53 %% initial guess: Gaussian
54 % initial guess FWHM values of WG beam at exit surface
55 FWHM_x = 35e-9;
56 sigma_x = FWHM_x/(2*sqrt(2*log(2)));
57 FWHM_y = 35e-9;
58 sigma_y = FWHM_y/(2*sqrt(2*log(2)));
59 psi_start = 1/sqrt(4*pi^2*(sigma_x^2*sigma_y^2))*exp(-X_1.^2/(2*sigma_x^2) - Y_1.^2/(2*sigma_y^2));
60
61 %% ER reconstruction
62 clear err in;
63 in = psi_start;
64 figure
65 for l=1:1:3
66     in = fft2(in);
67     % fourier-space constraint
68     In = sqrt(fftshift(I_exp_cen)).*in./abs(In + eps);
69     in = ifft2(In);
70     % real-space constraint
71     in = supp.*in;
72     % reconstruction error
73     err(l) = sum(sum(abs((I_exp_cen)-(abs(fftshift(fft2(in.*supp))).^2)))) ./ sum(sum(I_exp_cen));
74     subplot(2,2,2); plot(err);title(num2str(l)); drawnow;
75     subplot(2,2,1); imagesc(abs(in)); axis equal; colormap gray; axis tight;title('reconstructed amplitude');drawnow;
76     subplot(2,2,3); imagesc(angle(in)); axis equal; axis tight;title('reconstructed phase'); drawnow;
77     subplot(2,2,4); imagesc(supp); axis equal; axis tight;title('support'); drawnow;
78 end

```

Holographic reconstruction of measured holograms

holo_recon_scan.m

```

1 %% holographic reconstruction of the measured Siemens star holograms (mesh scan)
2 %% each hologram is reconstructed individually and the reconstructions are then stitched together
3 clear all;
4 close all
5 % import all cleaned ccd images of the mesh scan
6 load '/home/AG_Salditt/Publikationen/in_preparation_submitted_2009/Krueger_etal_crossedWG/fig4_siemens/IC35nm_NTT_mesh2
  /0912/data_div.mat';
7
8 %% parameters
9 % energy in keV
10 E = 17.5;
11 % wavelength [m]
12 lambda = 12.4397/E*1E-10;
13 k = 2*pi/lambda;
14 % distance source-sample [m]
15 z1 = 4.48e-3;
16 % distance sample-detector [m]
17 z2 = 3.09;
18 % effective distance of detector
19 z_eff = z1*z2/(z1+z2);
20 % effective magnification factor
21 M = (z1+z2)/z1;
22 % pixel size in detection plane
23 dx_det = 55e-6;
24 dy_det = 55e-6;
25 % pixel size in sample plane
26 dx = dx_det/M;
27 dy = dy_det/M;
28 % step size in pixel of mesh scan
29 stept = 25,25;
30 step2 = 24;
31 % regridding: interpolation factor
32 m = 2;

```

```

33 % section of the reconstructed image
34 a1 = 115*m;
35 b1 = 141*m;
36 a2 = b1 + step1*m*15;
37 a3 = b1 + step2*m*15;
38 % number of pixels
39 Nxs = a2-a1;
40 Nys = a2-a1;
41 % grid parameters
42 step3 = step1*m;
43 step4 = step2*m
44 % create matrix (15 x 15 scan points)
45 A_psi = zeros(m*256+15*step3,m*256+15*step4);
46
47 %% reconstruction with gridding
48 for c = 1:16
49     for d = 1:16
50         I_exp = data{(c-1)*16+d};
51         I_exp = I_exp/mean(mean(I_exp));
52         % total number of elements
53         N = numel(I_exp);
54         %number of pixels
55         [Ny,Nx] = size(I_exp);
56         % magnified coordinate system in detector plane
57         [X_det,Y_det] = meshgrid(dx_det*((1:1:Nx)-floor(Nx/2)-1),dy_det*((1:1:Ny)-floor(Ny/2)-1));
58         % coordinate system in sample plane
59         [X,Y] = meshgrid(dx*((1:1:Nx)-floor(Nx/2)-1),dy*((1:1:Ny)-floor(Ny/2)-1));
60         % regridding
61         [XI,YI] = meshgrid(dx/m*((1:1:Nx)-floor(Nx/2)-1),dy/m*((1:1:Ny)-floor(Ny/2)-1));
62         I_exp = interp2(X,Y,I_exp,XI,YI,'spline');
63         %number of pixels after regridding
64         [Ny,Nx] = size(I_exp);
65         % demagnified pixel size in sample plane
66         dx = dx_det/M/m;
67         dy = dy_det/M/m;
68         % grid conversion in q-space
69         dqx = 2*pi/(Nx*dx);
70         dqy = 2*pi/(Ny*dy);
71         % coordinate system in q-space
72         [Qx,Qy] = meshgrid(dqx*((1:1:Nx)-floor(Nx/2)-1),dqy*((1:1:Ny)-floor(Ny/2)-1));
73         % estimation of Poissonian error
74         sigma = sqrt(I_exp);
75         % reconstruction
76         kappa = sqrt(k.^2-(Qx.^2+Qy.^2));
77         psi_recon = fft2(fft2(I_exp).*fftshift(exp(-ii*kappa*z_off)));
78         % smoothing by use of a Gaussian
79         gaussenveloppe = zeros(256*m,256*m);
80         for ii = 1:256*m
81             for jj = 1:256*m
82                 gaussenveloppe(ii,jj)=gaussenveloppe(ii,jj)+exp(-(ii-128*m)^2/(100*m)^2-(jj-128*m)^2/(100*m)^2);
83             end
84         end
85
86         for ii = 1:256*m
87             for jj = 1:256*m
88                 gaussenveloppe(ii,jj)=gaussenveloppe(ii,jj)+exp(-(ii-128)^2/100-(jj-128)^2/100);
89             end
90         end
91         % filling of the matrix with reconstructed images (stitching)
92         A_psi(a1+step3*(c-1):b1+step3*(c-1),a1+step4*(d-1):b1+step4*(d-1)) = A_psi(a1+step3*(c-1):b1+step3*(c-1),a1+
            step4*(d-1):b1+step4*(d-1)) + psi_recon(a1:b1,a1:b1);
93     end
94 end
95
96 %% plot reconstruction
97 figure;
98 imagesc(Nxs*dx/m* linspace(0,1,Nys)*1E6, Nys*dx/m* linspace(0,1,Nxs)*1E6,mod(angle(A_psi(a1:a2,a1:a3)),2*pi)');
99 colormap gray;
100 axis equal ;
101 colorbar
102 caxis([2.3 3.2]);
103 axis off;
104 % scale bar
105 line(linspace(13,15,10),linspace(14,14,10),'LineWidth',8,'Color','w');

```

Iterative reconstruction of measured holograms

GS-Gaussian_GS.m

```

1  %% reconstruction of a hologram using the GS-Gaussian GS algorithm
2
3  %% I_exp is the normalized hologram
4
5  %% initial guess: holographic reconstruction
6  psi_recon_holo = ifft2(fft2(sqrt(I_exp)).*ifftshift(exp(-i*kappa*z_eff)));
7
8  %% stop criterion: algorithm stops when err < sigma
9  % WG is the waveguide far-field
10 sigma = sqrt(mean2(2./WG))
11
12 %% create Gaussian with a 1 pixel variance
13 gaussenveloppe = zeros(size(I_exp));
14 sigmagauss = 1;
15 for ii = 1:sqrt(numel(I_exp))
16     for jj = 1:sqrt(numel(I_exp))
17         gaussenveloppe(ii,jj)=gaussenveloppe(ii,jj)+exp(-(ii-sqrt(numel(I_exp)))^2)/(sigmagauss)^2-(jj-sqrt(numel(I_exp)))/2
18             ^2/(sigmagauss)^2);
19     end;
20 end;
21 gaussenveloppe = gaussenveloppe(sqrt(numel(I_exp)))/2-10:sqrt(numel(I_exp))/2+10:sqrt(numel(I_exp))/2-10:sqrt(numel(I_exp))
22     /2+10);
23
24 %% GS-Gaussian reconstruction
25 clear err in
26 % initial guess
27 in = psi_recon_holo;
28 % number of iterations
29 N = 100;
30 scrsz = get(0,'ScreenSize');
31 figure('Position',[scrsz(3)/24 scrsz(4)/4.2 scrsz(3)/1.1 scrsz(4)/1.5]);
32 for l = 1:N
33     Psi_recon = fftshift(fft2(fft2(fftshift(in)).*ifftshift(exp(i*kappa*z_eff))));
34     % fourier-space constraint
35     Psi_recon = sqrt(I_exp).*(Psi_recon./abs(Psi_recon));
36     in = fft2(fft2(Psi_recon).*ifftshift(exp(-i*kappa*z_eff)));
37     % convolution of the iterate with 1 pixel variance Gaussian function
38     in = conv2(in,gaussenveloppe,'same');
39     % real-space constraint
40     psi_ampl = ones(size(in));
41     in = psi_ampl.*(in./abs(in));
42     % error metric
43     err(l) = sum(sum(abs(sqrt(I_exp)-(abs(fftshift(fft2(fft2(fftshift(in)).*ifftshift(exp(i*kappa*z_eff)))))^2) ./
44         sum(sum(I_exp)));
45     subplot(2,2,1); imagesc(Nx*dx*linspace(0,1,Ny)*1E6,Nx*dx*linspace(0,1,Nx)*1E6,angle(psi_recon_holo)); colormap gray;
46     axis equal tight; colorbar; title('holo reconstructed phase');caxis([-0.9 -0.4]);drawnow;
47     subplot(2,2,2); imagesc(Nx*dx*linspace(0,1,Ny)*1E6,Nx*dx*linspace(0,1,Nx)*1E6,angle(in)); colormap gray; axis equal
48     tight; colorbar; title('reconstructed phase'); caxis([-0.9 -0.4]); drawnow; %caxis([4.85,5.35]);
49     subplot(2,2,3); imagesc(Nx*dx*linspace(0,1,Ny)*1E6,Nx*dx*linspace(0,1,Nx)*1E6,abs(in)); colormap gray; axis equal
50     tight; colorbar; title('reconstructed amplitude'); drawnow;
51     subplot(2,2,4); plot(err); title(['iteration' num2str(l)]); drawnow;
52     % algorithm stop-criterion
53     if err(l) <= sigma
54         break;
55     end
56 end
57
58 %% GS reconstruction
59 clear err
60 % number of iterations
61 N = 100;
62 scrsz = get(0,'ScreenSize');
63 figure('Position',[scrsz(3)/24 scrsz(4)/4.2 scrsz(3)/1.1 scrsz(4)/1.5]);
64 for l = 1:N
65     Psi_recon = fftshift(fft2(fft2(fftshift(in)).*ifftshift(exp(i*kappa*z_eff))));
66     % fourier-space constraint
67     Psi_recon = sqrt(I_exp).*(Psi_recon./abs(Psi_recon));
68     in = fft2(fft2(Psi_recon).*ifftshift(exp(-i*kappa*z_eff)));
69     % real-space constraint
70     psi_ampl = ones(size(in));
71     in = psi_ampl.*(in./abs(in));
72     % error metric
73     err(l) = sum(sum(abs(sqrt(I_exp)-(abs(fftshift(fft2(fft2(fftshift(in)).*ifftshift(exp(i*kappa*z_eff)))))^2) ./
74         sum(sum(I_exp)));
75     subplot(2,2,1); imagesc(Nx*dx*linspace(0,1,Ny)*1E6,Nx*dx*linspace(0,1,Nx)*1E6,angle(psi_recon_holo)); colormap gray;
76     axis equal tight; colorbar; title('holo reconstructed phase');drawnow;
77     subplot(2,2,2); imagesc(Nx*dx*linspace(0,1,Ny)*1E6,Nx*dx*linspace(0,1,Nx)*1E6,angle(in)); colormap gray; axis equal
78     tight; colorbar; title('reconstructed phase'); drawnow;

```



```

70     subplot(2,2,3); imagesc(Nx*dx*linspace(0,1,Ny)*1E6,Nx*dx*linspace(0,1,Nx)*1E6,abs(in)); colormap gray; axis equal
71         tight; colorbar; title('reconstructed amplitude'); drawnow;
72     subplot(2,2,4); plot(err); title(['iteration' num2str(1)]); drawnow;
73     % algorithm stop-criterion
74     if err(1) <= sigma
75         break;
76     end
end

```

ER_min-max.m

```

1  %% reconstruction of a hologram using the GS-Gaussian GS algorithm
2
3  %% I_exp is the normalized hologram
4
5  %% initial guess: holographic reconstruction
6  psi_recon_holo = ifft2(fft2(sqrt(I_exp)).*ifftshift(exp(-i*kappa*z_eff)));
7
8  %% stop criterion: algorithm stopps when err < sigma
9  % WG is the waveguide far-field
10 sigma = sqrt(mean2(2./WG))
11
12 %% ER_min-max algorithm
13 clear err in
14 % initial guess
15 in = psi_recon_holo;
16 % number of iterations
17 N = 100;
18 scrsz = get(0,'ScreenSize');
19 figure('Position',[scrsz(3)/24 scrsz(4)/4.2 scrsz(3)/1.1 scrsz(4)/1.5]);
20 for l = 1:N
21     Psi_recon = fftshift(ifft2(fft2(ifftshift(in)).*ifftshift(exp(ii*kappa*z_eff))));
22     % fourier-space constraint
23     Psi_recon = sqrt(I_exp).*(Psi_recon./abs(Psi_recon));
24     in = fft2(ifft2(Psi_recon).*ifftshift(exp(-i*kappa*z_eff)));
25     % real-space constraint
26     psi_ampl = abs(in);
27     I_max = 1.0; % maximum transmission value of the object
28     I_min = 0.9644; % minimal transmission value of the object
29     psi_ampl = min(I_max,psi_ampl);
30     psi_ampl = max(I_min,psi_ampl);
31     in = psi_ampl.*(in./abs(in));
32     % error metric
33     err(l) = sum(sum(abs(sqrt(I_exp)-(abs(fftshift(ifft2(fft2(ifftshift(in)).*ifftshift(exp(ii*kappa*z_eff)))))).^2) ./
34         sum(sum(I_exp)));
35     subplot(2,2,1); imagesc(Nx*dx*linspace(0,1,Ny)*1E6,Nx*dx*linspace(0,1,Nx)*1E6,angle(psi_recon_holo)); colormap gray;
36         axis equal tight; colorbar; title('holo reconstructed phase');drawnow;
37     subplot(2,2,2); imagesc(Nx*dx*linspace(0,1,Ny)*1E6,Nx*dx*linspace(0,1,Nx)*1E6,angle(in)); colormap gray; axis equal
38         tight; colorbar; title('reconstructed phase'); drawnow;
39     subplot(2,2,3); imagesc(Nx*dx*linspace(0,1,Ny)*1E6,Nx*dx*linspace(0,1,Nx)*1E6,abs(in)); colormap gray; axis equal
40         tight; colorbar; title('reconstructed amplitude'); drawnow;
41     subplot(2,2,4); plot(err); title(['iteration' num2str(1)]); drawnow;
42     % algorithm stop-criterion
43     if err(1) <= sigma
44         break;
45     end
end

```

References

- [1] Chao, W., Harteneck, B. D., Liddle, J. A., Anderson, E. H., and Attwood, D. T. *Nature* **435**(7046), 1210–1213 June (2005).
- [2] Uchida, M., McDermott, G., Wetzler, M., Le Gros, M. A., Myllys, M., Knoechel, C., Barron, A. E., and Larabell, C. A. *Proceedings of the National Academy of Sciences* **106**(46), 19375–19380 (2009).
- [3] Chao, W., Kim, J., Rekawa, S., Fischer, P., and Anderson, E. H. *Opt. Express* **17**(20), 17669–17677 September (2009).
- [4] Hignette, O., Cloetens, P., Rostaing, G., Bernard, P., and Morawe, C. *Review of Scientific Instruments* **76**(6), 063709 (2005).
- [5] Schroer, C. G., Kurapova, O., Patommel, J., Boye, P., Feldkamp, J., Lengeler, B., Burghammer, M., Riekkel, C., Vincze, L., van der Hart, A., and Kuchler, M. *Appl. Phys. Lett.* **87**(12), 124103–3 September (2005).
- [6] Miao, J., Charalambous, P., Kirz, J., and Sayre, D. *Nature* **400**(6742), 342–344 July (1999).
- [7] Williams, G. J., Quiney, H. M., Dhal, B. B., Tran, C. Q., Nugent, K. A., Peele, A. G., Paterson, D., and de Jonge, M. D. *Physical Review Letters* **97**(2), 025506 (2006).
- [8] Schropp, A., Boye, P., Feldkamp, J. M., Hoppe, R., Patommel, J., Samberg, D., Stephan, S., Giewekemeyer, K., Wilke, R. N., Salditt, T., Gulden, J., Mancuso, A. P., Vartanyants, I. A., Weckert, E., Schoder, S., Burghammer, M., and Schroer, C. G. *Appl. Phys. Lett.* **96**(9), 091102–3 March (2010).
- [9] Schroer, C. G., Boye, P., Feldkamp, J. M., Patommel, J., Schropp, A., Schwab, A., Stephan, S., Burghammer, M., Schoder, S., and Riekkel, C. *Phys. Rev. Lett.* **101**(9), 090801 (2008).
- [10] Gabor, D. *Nature* **161**, 777–778 May (1948).
- [11] Giewekemeyer, K., Krüger, S. P., Kalbfleisch, S., Bartels, M., Beta, C., and Salditt, T. *Phys. Rev. A* **83**(2), 023804 Feb (2011).
- [12] Gerchberg, R. W. and Saxton, W. O. *Optik (Jena)* **35**, 237–246 (1972).
- [13] Fienup, J. R. *Opt. Lett.* **3**(1), 27–29 (1978).

- [14] Rodenburg, J. M. and Faulkner, H. M. L. *Appl. Phys. Lett.* **85**(20), 4795–4797 November (2004).
- [15] Pfeiffer, F., David, C., Burghammer, M., Riekkel, C., and Salditt, T. *Science* **297**(6), 230 (2002).
- [16] Jarre, A., Fuhse, C., Ollinger, C., Seeger, J., Tucoulou, R., and Salditt, T. *Physical Review Letters* **94**(7), 074801 (2005).
- [17] Fuhse, C., Jarre, A., Ollinger, C., Seeger, J., Salditt, T., and Tucoulou, R. *Applied Physics Letters* **85**(11), 1907–1909 (2004).
- [18] Fuhse, C., Ollinger, C., and Salditt, T. *Physical Review Letters* **97**(25), 254801 (2006).
- [19] Fuhse, C. *X-ray waveguides and waveguide-based lensless imaging*. PhD thesis, University of Göttingen, (2006).
- [20] Salditt, T., Krüger, S. P., Fuhse, C., and Bähz, C. *Phys. Rev. Lett.* **100**(18), 184801–4 May (2008).
- [21] Caro, L. D., Giannini, C., Pelliccia, D., Mocuta, C., Metzger, T. H., Guagliardi, A., Cedola, A., Burkeeva, I., and Lagomarsino, S. *Physical Review B (Condensed Matter and Materials Physics)* **77**(8), 081408 (2008).
- [22] Born, M. and Wolf, E. *Principles of optics: 7th (expanded) edition*. Principles of optics: 7th (expanded) edition by Born, M., (1999).
- [23] Paganin, D. M. *Coherent X-Ray Optics*. Oxford Univ. Press, (2006).
- [24] Cowley, J. *Diffraction physics*. North Holland Publishing Company, Amsterdam, New York, Oxford, (1981).
- [25] Gabor, D. *J.Instn.Elect.Engrs.* **93**, 429–457 (1946).
- [26] Goodman, J. W. *Introduction to Fourier optics*. McGraw-Hill, (1996).
- [27] Als-Nielsen, J. and McMorrow, D. *Elements of Modern X-ray Physics*. (2001).
- [28] Cloetens, P. *Contribution to Phase Contrast Imaging, Reconstruction and Tomography with Hard Synchrotron Radiation*. PhD thesis, Vrije Universiteit Brussel, (1999).
- [29] Salditt, T., Giewekemeyer, K., Fuhse, C., Krüger, S. P., Tucoulou, R., and Cloetens, P. *Phys. Rev. B* **79**(18), 184112–6 May (2009).

- [30] Morgan, K. S., Siu, K. K. W., and Paganin, D. M. *Opt. Express* **18**(10), 9865–9878 (2010).
- [31] Mayo, S., Miller, P., Wilkins, S., Davis, T., Gao, D., Gureyev, T., Paganin, D., Parry, D., Pogany, A., and Stevenson, A. *J. Microsc.* **207**(Pt 2), 79–96 (2002).
- [32] Kohn, V., Snigireva, I., and Snigirev, A. *Optics Communications* **198**(4-6), 293 – 309 (2001).
- [33] Gureyev, T. E., Raven, C., Snigirev, A., Snigireva, I., and Wilkins, S. W. *J. Phys. D: Appl. Phys.* **32**(5), 563–567 (1999).
- [34] Fienup, J. R. *Appl. Opt.* **21**(15), 2758–2769 (1982).
- [35] Marchesini, S. *Rev. Sci. Instrum.* **78**(1), 011301 (2007).
- [36] Elser, V. *J. Opt. Soc. Am. A* **20**(1), 40–55 January (2003).
- [37] Jimenez, J. and Hita, E. *Optical Review* **8**, 495–497 (2001).
10.1007/BF02931741.
- [38] Shannon, C. *Proceedings of the IRE DOI* - **37**(1), 10–21 (1949).
- [39] Fienup, J. R. and Wackerman, C. C. *J. Opt. Soc. Am. A* **3**(11), 1897–1907 (1986).
- [40] Voelz, D. G. and Roggemann, M. C. *Appl. Opt.* **48**(32), 6132–6142 (2009).
- [41] Bauschke, H. H., Combettes, P. L., and Luke, D. R. *Journal of Approximation Theory* **127**(2), 178 – 192 (2004).
- [42] Miao, J., Sayre, D., and Chapman, H. N. *J. Opt. Soc. Am. A* **15**(6), 1662–1669 (1998).
- [43] Lane, R. *Optics Communications* **63**(1), 6 – 10 (1987).
- [44] Fienup, J. R. *J. Opt. Soc. Am. A* **4**(1), 118–123 (1987).
- [45] Millane, R. P. *J. Opt. Soc. Am. A* **7**(3), 394–411 (1990).
- [46] Chapman, H. N., Barty, A., Marchesini, S., Noy, A., Hau-Riege, S. P., Cui, C., Howells, M. R., Rosen, R., He, H., Spence, J. C. H., Weierstall, U., Beetz, T., Jacobsen, C., and Shapiro, D. *J. Opt. Soc. Am. A* **23**(5), 1179–1200 (2006).
- [47] Krüger, S. P., Giewekemeyer, K., Kalbfleisch, S., Bartels, M., Neubauer, H., and Salditt, T. *Opt. Express* **18**(13), 13492–13501 June (2010).

- [48] Somogyi, A., Tucoulou, R., Martinez-Criado, G., Homs, A., Cauzid, J., Bleuet, P., Bohic, S., and Simionovici, A. *Journal of Synchrotron Radiation* **12**(2), 208–215 (2005).
- [49] Mimura, H., Yumoto, H., Matsuyama, S., Sano, Y., Yamamura, K., Mori, Y., Yabashi, M., Nishino, Y., Tamasaku, K., Ishikawa, T., and Yamauchi, K. *Applied Physics Letters* **90**(5), 051903 (2007).
- [50] Mimura, H., Matsuyama, S., Yumoto, H., Hara, H., Yamamura, K., Sano, Y., Shibahara, M., Endo, K., Mori, Y., Nishino, Y., Tamasaku, K., Yabashi, M., Ishikawa, T., and Yamauchi, K. *Japanese Journal of Applied Physics* **44**(18), L539–L542 (2005).
- [51] Mimura, H., Handa, S., Kimura, T., Yumoto, H., Yamakawa, D., Yokoyama, H., Matsuyama, S., Inagaki, K., Yamamura, K., Sano, Y., Tamasaku, K., Nishino, Y., Yabashi, M., Ishikawa, T., and Yamauchi, K. *Nat Phys* **6**(2), 122–125 February (2010).
- [52] Chu, Y. S., Yi, J. M., Carlo, F. D., Shen, Q., Lee, W.-K., Wu, H. J., Wang, C. L., Wang, J. Y., Liu, C. J., Wang, C. H., Wu, S. R., Chien, C. C., Hwu, Y., Tkachuk, A., Yun, W., Feser, M., Liang, K. S., Yang, C. S., Je, J. H., and Margaritondo, G. *Applied Physics Letters* **92**(10), 103119 (2008).
- [53] Technische Universität Dresden, *Refractive X-Ray Lenses*, http://tu-dresden.de/die_tu_dresden/fakultaeten/fakultaet_mathematik_und_naturwissenschaften/fachrichtung_physik/isp/skm/research/xray_lenses/crl_pic. Last access on 10/20/2010.
- [54] Snigirev, A., Kohn, V., Snigireva, I., and Lengeler, B. *Nature* **384**(6604), 49–51 November (1996).
- [55] Gary, C. K., Pikuz, S. A., Mitchell, M. D., Chandler, K. M., Shelkovenko, T. A., Hammer, D. A., and Dudchik, Y. I. *Review of Scientific Instruments* **75**(10), 3950–3952 (2004).
- [56] Cederstrom, B., Cahn, R. N., Danielsson, M., Lundqvist, M., and Nygren, D. R. *Nature* **404**(6781), 951–951 April (2000).
- [57] Eisebitt, S., Luning, J., Schlotter, W. F., Lorgen, M., Hellwig, O., Eberhardt, W., and Stohr, J. *Nature* **432**(7019), 885–888 December (2004).
- [58] Giewekemeyer, K., Thibault, P., Kalbfleisch, S., Beerlink, A., Kewish, C. M., Dierolf, M., Pfeiffer, F., and Salditt, T. *Proceedings of the National Academy of Sciences* **107**(2), 529–534 (2010).

- [59] Jarre, A., Seeger, J., Ollinger, C., Fuhse, C., David, C., and Salditt, T. *Journal of Applied Physics* **101**(5), 054306 (2007).
- [60] Bergemann, C., Keymeulen, H., and van der Veen, J. F. *Phys. Rev. Lett.* **91**(20), 204801– November (2003).
- [61] Di Fonzo, S., Jark, W., Lagomarsino, S., Giannini, C., De Caro, L., Cedola, A., and Muller, M. *Nature* **403**(6770), 638–640 February (2000).
- [62] Quiney, H. M., Peele, A. G., Cai, Z., Paterson, D., and Nugent, K. A. *Nat Phys* **2**(2), 101–104 February (2006).
- [63] Spiller, E. and Segmuller, A. *Applied Physics Letters* **24**(2), 60–61 (1974).
- [64] Bongaerts, J. H. H., David, C., Drakopoulos, M., Zwanenburg, M. J., Wegdam, G. H., Lackner, T., Keymeulen, H., and van der Veen, J. F. *Journal of Synchrotron Radiation* **9**(6), 383–393 Nov (2002).
- [65] Shabel'nikov, L., Snigirev, A., Snigireva, I., Kuznetsov, S., Yunkin, V., Levashov, V., and Grigoriev, M. *J. Phys. IV France* **104**, 227–230 (2003).
- [66] Marcuse, D. *Theory of Dielectric Optical Waveguides*. Acad. Press, New York, (1974).
- [67] Zwanenburg, M. J., van der Veen, J. F., Ficke, H. G., and Neerings, H. *Review of Scientific Instruments* **71**(4), 1723–1732 (2000).
- [68] Fuhse, C. and Salditt, T. *Physica B: Condensed Matter* **357**(1-2), 57–60 February (2005).
- [69] Fock, V. *Electromagnetic diffraction and propagation problems*. Pergamon, Oxford, (1965).
- [70] Kopylov, Y. V., Popov, A. V., and Vinogradov, A. V. *Optics Communications* **118**(5-6), 619–636 August (1995).
- [71] Scarmozzino, R. and R. M. Osgood, J. *J. Opt. Soc. Am. A* **8**(5), 724–731 (1991).
- [72] Crank, J. and Nicolson, P. *Proc. Cambridge Philos. Soc.* **43**, 55–67 (1947).
- [73] Fuhse, C. and Salditt, T. *Optics Communications* **265**(1), 140–146 September (2006).
- [74] Ghatak, A. and Thyagarajan, K. *An Introduction to Fiber Optics*. Cambridge Univ. Press, England, (1998).

- [75] Center for X-Ray Optics (CXRO), *X-Ray Interactions With Matter*, http://henke.lbl.gov/optical_constants/, <http://www.cxro.lbl.gov>. Last access on 07/20/2010.
- [76] Cohen-Tannoudji, C., Diu, B., and Laloe, F. *Quantenmechanik*. de Gruyter, (1999).
- [77] Martin, T. and Koch, A. *Journal of Synchrotron Radiation* **13**(2), 180–194 Mar (2006).
- [78] Windt, D. L. *Computers in Physics* **12**(4), 360–370 (1998).
- [79] Jorgenson, J. D. and George, M. W. *USGS Series* **2004-1300**, 24 (2005).
- [80] Henke, B. L., Gullikson, E. M., and Davis, J. C. *Atomic Data and Nuclear Data Tables* **54**(2), 181–342 July (1993).
- [81] Indium Corporation, *Table of alloys*, <http://www.indium.com/products/alloysolderchart.php>. Last access on 08/04/2010.
- [82] Cookson Electronics Enthone, *Product Information Enthone 4LF*, <http://www.enthone.com/functional/index.aspx?Detail=ENfinity-4-LFascx>. Last access on 08/04/2010.
- [83] Giannuzzi, L. A. and Stevie, F. *Introduction to Focused Ion beams: Instrumentation, Theory, Techniques and Practice*. Springer, (2005).
- [84] Volkert, C. A. and Minor, A. M. *MRS Bulletin* **32**, 389–399 (2007).
- [85] Kalbfleisch, S., Osterhoff, M., Giewekemeyer, K., Neubauer, H., Krüger, S. P., Hartmann, B., Bartels, M., Sprung, M., Leupold, O., Siewert, F., and Salditt, T. volume 1234, 433–436. AIP, (2010).
- [86] Rossendorf-Beamline, *Beamline Optics*, <http://www.hzdr.de/pls/rois/Cms?pNid=146>. Last access on 10/20/2010.
- [87] European Synchrotron Radiation Facility (ESRF), *Beamline manuel ID22*, <http://www.esrf.eu/UsersAndScience/Experiments/Imaging/ID22/BeamlineManual>. Last access on 10/21/2010.
- [88] Ollinger, C. G. J. *A waveguide-based lens-less x-ray microscope*. PhD thesis, University of Göttingen, (2006).
- [89] Hignette, O., Rostaing, G., Cloetens, P., Rommeveaux, A., Ludwig, W., and Freund, A. K. *Proceedings of SPIE* **4499**, 105–116 (2001).

- [90] Hignette, O., Cloetens, P., Lee, W.-K., Ludwig, W., and Rostaing, G. *J. Phys. IV France* **104**, 231–234 mar (2003).
- [91] Vartanyants, I. A. and Singer, A. (2009).
- [92] European Synchrotron Radiation Facility (ESRF), *ID1 beamline*, <http://www.esrf.eu/UsersAndScience/Experiments/StructMaterials/ID01>. Last access on 10/21/2010.
- [93] Ponchut, C., Clément, J., Rigal, J.-M., Papillon, E., Vallerger, J., LaMarra, D., and Mikulec, B. *Nuclear Instruments and Methods in Physics Research Section A: Accelerators, Spectrometers, Detectors and Associated Equipment* **576**(1), 109–112 June (2007).
- [94] Kalbfleisch, S., Neubauer, H., Krüger, S., Bartels, M., Osterhoff, M., Mai, D., Giewekemeyer, K., Hartmann, B., Sprung, M., and Salditt, T. *submitted* (2010).
- [95] Kraft, P., Bergamaschi, A., Broennimann, C., Dinapoli, R., Eikenberry, E. F., Henrich, B., Johnson, I., Mozzanica, A., Schlepütz, C. M., Willmott, P. R., and Schmitt, B. *Journal of Synchrotron Radiation* **16**(3), 368–375 (2009).
- [96] NTT Advanced Nanotechnology, *Nanofabrication Products*, <http://www.ntt-at.com/prdsvc/nanotech.html>. Last access on 10/20/2010.
- [97] Bushberg, J. T., Seibert, J. A., Leidholdt Jr., E. M., and Boone, J. M. *The Essential Physics of Medical Imaging*. Philadelphia: Lippincott Williams & Wilkins, (2006).
- [98] Oppenheim, A. V. and Schaffer, R. W. *Discrete-Time Signal Processing*. Prentice-Hall, (1989).
- [99] de Boor, C. R. *A Practical Guide to Splines*. (1978).
- [100] Marchesini, S., He, H., Chapman, H. N., Hau-Riege, S. P., Noy, A., Howells, M. R., Weierstall, U., and Spence, J. C. H. *Phys. Rev. B* **68**(14), 140101 Oct (2003).
- [101] Giewekemeyer, K., Hantke, M., Beta, C., Tucoulou, R., and Salditt, T. *Journal of Physics: Conference Series* **186**(1), 012086 (2009).
- [102] Geloni, G., Saldin, E., Samoylova, L., Schneidmiller, E., Sinn, H., Tschentscher, T., and Yurkov, M. *New Journal of Physics* **12**(3), 035021 (2010).

- [103] Cooley, J. W. and Tukey, J. W. *Mathematics of Computation* **19**(90), 297–301 (1965).
- [104] Thibault, P. *Algorithmic methods in diffraction microscopy*. PhD thesis, University Microfilms International, (2008).
- [105] Miao, J. and Sayre, D. *Acta Crystallographica Section A* **56**(6), 596–605 (2000).
- [106] Elser, V. and Millane, R. P. *Acta Crystallographica Section A* **64**(2), 273–279 Mar (2008).
- [107] Mas, D., Perez, J., Vazquez, C., Hernandez, C., and Illueca, C. *Journal of Modern Optics* **50**(9), 1335 (2003).
- [108] Mas, D., Pérez, J., Hernández, C., Vázquez, C., Miret, J. J., and Illueca, C. *Optics Communications* **227**(4-6), 245 – 258 (2003).
- [109] Bruck, Y. M. and Sodin, L. G. *Optics Communications* **30**(3), 304 – 308 (1979).
- [110] Sanz, J. L. C., Huang, T. S., and Cukierman, F. *J. Opt. Soc. Am.* **73**(11), 1442–1445 (1983).
- [111] Hayes, M. and McClellan, J. *Proceedings of the IEEE* **70**(2), 197 – 198 feb. (1982).
- [112] Barakat, R. and Newsam, G. *J. Math. Phys.* **25**(11), 3190–3193 November (1984).
- [113] Seldin, J. H. and Fienup, J. R. *J. Opt. Soc. Am. A* **7**(3), 412–427 (1990).
- [114] Nugent, K. A., Peele, A. G., Quiney, H. M., and Chapman, H. N. *Acta Crystallographica Section A* **61**(3), 373–381 May (2005).
- [115] Hoppe, W. *Acta Crystallographica Section A* **25**(4), 495–501 (1969).
- [116] Nellist, P. D., McCallum, B. C., and Rodenburg, J. M. *Nature* **374**(6523), 630–632 April (1995).
- [117] Rodenburg, J. M., Hurst, A. C., Cullis, A. G., Dobson, B. R., Pfeiffer, F., Bunk, O., David, C., Jefimovs, K., and Johnson, I. *Phys. Rev. Lett.* **98**(3), 034801–January (2007).
- [118] Thibault, P., Dierolf, M., Menzel, A., Bunk, O., David, C., and Pfeiffer, F. *Science* **321**(5887), 379–382 (2008).

-
- [119] Dierolf, M., Menzel, A., Thibault, P., Schneider, P., Kewish, C. M., Wepf, R., Bunk, O., and Pfeiffer, F. *Nature* **467**(7314), 436–439 September (2010).
- [120] Giewekemeyer, K., Neubauer, H., Kalbfleisch, S., Krüger, S. P., and Salditt, T. *New Journal of Physics* **12**(3), 035008 (2010).

List of publications

S. P. Krüger, H. Neubauer, M. Bartels, P. J. Wilbrandt, M. Seibt and T. Salditt,
A study of high transmission planar x-ray waveguides,
in preparation.

S. Kalbfleisch, H. Neubauer, S. P. Krüger, M. Bartels, M. Osterhoff, D. D. Mai,
K. Giewekemeyer, B. Hartmann, M. Sprung and T. Salditt,
The Göttingen holography endstation of beamline P10 at PETRA III/DESY,
accepted to AIP. Conf. Proc. (2011).

T. Salditt, S. Kalbfleisch, M. Osterhoff, S. P. Krüger, M. Bartels, K. Giewekemeyer,
H. Neubauer, and M. Sprung
Partially coherent nano-focused x-ray radiation characterized by Talbot interferometry,
Opt. Express **19**, 9656-9675 (2011).

K. Giewekemeyer, S. P. Krüger, S. Kalbfleisch, M. Bartels, C. Beta and T. Salditt,
X-ray propagation microscopy of biological cells using waveguides as a quasipoint source,
Phys. Rev. A **83**, 023804 (2011).

S. Kalbfleisch, M. Osterhoff, K. Giewekemeyer, H. Neubauer, S. P. Krüger,
B. Hartmann, M. Bartels, M. Sprung, O. Leupold, F. Siewert and T. Salditt,
The holography endstation of beamline P10 at PETRA III,
AIP. Conf. Proc., **1234**, 433-436 (2010).

S. P. Krüger, K. Giewekemeyer, S. Kalbfleisch, M. Bartels, H. Neubauer and T. Salditt,
Sub-15 nm beam confinement by two crossed x-ray waveguides,
Opt. Express **18**, 13492-13501 (2010).

K. Giewekemeyer, H. Neubauer, S. Kalbfleisch, S. P. Krüger and T. Salditt,
Holographic and diffractive x-ray imaging using waveguides as quasi-point sources,
New J. Phys. **12**, 035008 (2010).

T. Salditt, K. Giewekemeyer, C. Fuhse, S. P. Krüger, R. Tucoulou and P. Cloetens,
Projection phase contrast microscopy with a hard x-ray nanofocused beam: Defocus and contrast transfer,
Phys. Rev. B **79**, 184112 (2009).

T. Salditt, S. P. Krüger, C. Fuhse and C. Bähz,
High-transmission planar x-ray waveguides,
Phys. Rev. Lett. **100**, 184801 (2008).

J. K. Krüger, P. Alnot, J. Baller, R. Bactavatchalou, S. Dorosz, M. Henkel, M. Kolle,
S. P. Krüger, U. Müller, M. Philipp, W. Possart, R. Sanctuary, C. Vergnat
About the nature of the structural glass transition: an experimental approach,
Lect. Notes Phys. **716**, 61–159 (2007).

P. Mesquida, S. P. Krüger, J. K. Krüger,
*Präzisionsmessungen der spezifischen Wärmekapazität mit Hilfe der Temperatur-
Modulierten-DSC (TMDSC) bei mitteltiefen Temperaturen*,
Mettler-Toledo GmbH Usercom, **7**, 12 (1998).

Patent application

T. Salditt und S. P. Krüger,
Konfokaler Multilamellenwellenleiter,
Patentanmeldung DE 102010002778 (nicht offengelegt), 11.03.2010.

Danksagung

Ich möchte mich ganz herzlich bei Prof. Tim Salditt für die interessante Aufgabenstellung und seine erstklassige Betreuung bedanken. Seine motivierende Art, seine allzeit positive Einstellung und seine Warmherzigkeit haben mich tief beeindruckt. Danke auch für die anregenden Diskussionen, zahlreichen Erläuterungen und neuen Ideen, die mich in meiner Arbeit entscheidend vorangebracht haben.

Ich bedanke mich ganz herzlich bei Prof. Hans-Ulrich Krebs, der sich bereitklärt hat, das Zweitgutachten für meine Doktorarbeit anzufertigen.

Ich möchte mich bei Klaus Giewekemeyer insbesondere für die unermüdlichen Diskussionen und die weitreichende Unterstützung bei den Simulationen und Rekonstruktionen der Beugungsbilder bedanken. Henrike Neubauer gilt mein Dankeschön für die außerordentlich gute Zusammenarbeit bei den Messzeiten zur Charakterisierung der Wellenleiter. Auch bedanke ich mich bei Sebastian Kalbfleisch für seine sachkundige und wertvolle Unterstützung bei den Experimenten. Mathias Bartels hat durch seinen unermüdlichen Einsatz und seine konstruktiven Ideen ganz maßgeblich zum Erfolg der Messzeiten beigetragen. Für ausgiebige fachliche Diskussionen danke ich Markus Osterhoff und Robin Wilke.

Ein weiterer Dank gilt den Mitarbeitern an der European Synchrotron Radiation Facility (ESRF, Grenoble) und dem Deutschen Elektronensynchrotron (DESY, Hamburg), insbesondere Dr. Carsten Bähz und Dr. Nicole Jeutter (BM20), Dr. Peter Cloetens und Dr. Rémi Tucoulou (ID22), Dr. Till Hartmut Metzger (ID1), und Dr. Michael Sprung (P10, Petra III). Ihre technische Unterstützung und ihr kompetenter Rat waren in vielen Phasen der Messzeiten von außerordentlichem Nutzen.

Thorsten Gronemann und Jochen Herbst bin ich für die ausgezeichnete Unterstützung bei den verschiedenen Wellenleiterherstellungsprozessen dankbar. Mit ihren weitreichenden praktischen Erfahrungen haben sie unter anderem zu der Ausarbeitung des chemisch Nickel Prozesses und der Aufdampfprozesse entscheidend beigetragen.

Die ausführlichen Erläuterungen von Dr. Peter-J. Wilbrandt und Volker Radisch aus dem Institut für Materialphysik zur Bedienung des Focused Ion Beam und ihre wertvollen Anregungen und Verbesserungsvorschläge ermöglichten es mir das Polieren der Wellenleiteroptiken zu optimieren. Mathias Hahn und Mike Kanbach danke ich für die exzellente Unterstützung bei der Rasterelektronenmikroskopie. Ich möchte mich bei Prof. Michael Seibt und seiner Arbeitsgruppe aus dem IV. Physikalischen Institut für die sehr hilfreiche Einführung in mechanische Schleif- und Polierprozesse bedanken.

Bastian Hartmann, Peter Nieschalk und Carsten Wulff danke ich für den Entwurf und die Fertigung von Komponenten des Messaufbaus. Mit ihrem großen Engagement ermöglichten sie es auch sehr kurzfristig, exzellent gefertigte Bauteile zur Verfügung zu stellen.

Ich möchte mich ganz herzlich bei Prof. Jan-Kristian Krüger und Dr. Martine Philipp für die kritische Korrektur der vorliegenden Arbeit und die wertvollen inhaltlichen Anmerkungen bedanken. Ich danke auch Dr. Sven Dorosz für den regen Austausch in quantenmechanischen Überlegungen. Sein fundiertes Wissen und seine schnelle Auffassungsgabe waren ausnehmend hilfreich.

Schließlich geht mein großer Dank an alle Mitarbeiter des Instituts für Röntgenphysik für die ausgesprochen freundliche Atmosphäre im Institut und für das große Engagement, das mir zuteil geworden ist. Insbesondere danke ich auch für die hervorragende Unterstützung bei Computerfragen und für die schnelle und unkomplizierte Hilfe in organisatorischen Fragen.

Die Forschungsarbeit wurde von der Deutschen Forschungsgemeinschaft über den *SFB755 Nanoscale Photonic Imaging* und von dem Bundesministerium für Bildung und Forschung unter der Fördernummer 05KS7MGA finanziell unterstützt.

Ein ganz besonderer Dank gilt meinen Eltern und meiner Schwester für ihre wertvolle Hilfe und ihren fortlaufenden Rückhalt. Ich danke Julia, dass sie mir stets zur Seite stand und mich immer wieder aufgemuntert hat.

Curriculum vitae

Sven Philip Krüger

geboren am 26. Dezember 1980 in Saarbrücken,
Staatsangehörigkeit: deutsch-französisch

Schul- und Berufsbildung

- seit 2006 wissenschaftlicher Mitarbeiter am Institut für Röntgenphysik,
Georg-August-Universität Göttingen
- 2006 Diplôme de d'études approfondies (D.E.A) Physique et chimie
de la matière condensée/Hauptdiplom in Physik
(Deutsch-französisches Doppeldiplom in Physik (integrierter
trinationaler Saar-Lor-Lux-Studiengang)), Titel der Diplomarbeit:
'États d'interfaces de dépôt d'un isolant sur métaux nobles',
Université de Nancy 1, Frankreich
- 2004 – 2006 Physik-Studium an der Université de Nancy 1
- 2003 – 2004 Physik-Studium an der Universität des Saarlandes
- 2002 – 2003 Physik-Studium an der Université du Luxembourg
- 2001 – 2002 Physik-Studium an der Universität des Saarlandes
- 2000 – 2001 Zivildienst, Deutsches Rotes Kreuz Sulzbach (Rettungsdienst)
- 2000 Abitur/Baccalauréat, Deutsch-französisches Gymnasium Saarbrücken

Lensless x-ray imaging is a promising method to determine the three-dimensional structure of material science and biological specimens at the nanoscale. The development of this technique is strongly related to the optimization of x-ray optics since the image formation and object reconstruction depend significantly on the properties of the illumination wave-field. Waveguide optics act as quasi-point sources and enable the spatial and coherent filtering of x-ray beams. Up to now, x-ray waveguides were severely limited in transmission and flux, restricting their use to high-contrast test structures with moderate resolution and long accumulation times. To overcome these limitations, a novel waveguide design with an optimized refractive index profile is presented which significantly minimizes the absorption of the modes propagating inside the waveguide. Experimental results along with simulations show that these two-component planar x-ray waveguides provide small beam cross-sections along with a high photon flux at the exit. By a serial arrangement of two waveguide slices an optimized illumination source has been developed for high-resolution microscopy, as demonstrated in proof-of-concept imaging experiments.



GEORG-AUGUST-UNIVERSITÄT
GÖTTINGEN

ISBN 978-3-86395-015-6
ISSN 2191-9860

Universitätsverlag Göttingen